Electrical Properties of Binary Solutions of Molten Titanium Dioxide-Barium Oxide

by

Naomi Anne Fried

B.S., Chemistry
University of California at Berkeley, 1987

Submitted to the
Department of Materials Science and Engineering
in partial fulfillment of the requirements
for the degree of

DOCTOR OF PHILOSOPHY

at the
Massachusetts Institute of Technology
Cambridge, Massachusetts

September, 1996

Author's
Signature________________________________
Department of Materials Science and Engineering
August 9, 1996

Certified by________________________________
Donald R. Sadoway
Professor of Materials Chemistry
Thesis Supervisor

Accepted by________________________________
Linn W. Hobbs
Chair, Departmental Committee on Graduate Students

Electrical Properties of Binary Solutions of Molten Titanium Dioxide-Barium Oxide

by

Naomi Anne Fried

Submitted to the
Department of Materials Science and Engineering
on August 9, 1996 in partial fulfillment of the
requirements for the Degree of Doctor of Philosophy
in Materials Science and Engineering

Abstract

The electrical properties of TiO_2-BaO melts were studied as part of an assessment of the viability of using molten oxide electrolysis to extract titanium from its ore.

Critical to the investigation was the development of two new techniques for measuring electrical conductivity in corrosive, high-temperature melts. The first technique used dielectric-free moveable coaxial-cylinders electrodes. Over the range of applicability of this technique, this cell did not require calibration. The second new technique developed for this work used a four-point crucible cell design. The key to obtaining highly accurate measurements of melt conductivity in the four-point crucible cell was the calibration procedure. A standard solution with conductivities similar to those of the melts under investigation was used to determine the relationship between the cell factor and conductivity of the specimen.

Electrical conductivities were measured over the temperature range 1325-1475°C for two compositions of molten TiO_2-BaO: 67 mol% TiO_2 and 73 mol% TiO_2. These two compositions are the end points of the TiO_2-BaO eutectic window at 1375°C. A triangular excitation signal with a magnitude of $\pm$ 0.1 V at a slew rate of 3 V/s was used both in cell calibration and for the four-point crucible measurement of electrical conductivity in the molten oxides. The crucible cell was calibrated with a 15:85 mol% mixture of KCl:NaCl over the temperature range 800-913°C.

At constant temperature, electrical conductivity (σ) increased with BaO content. Over the temperature interval measured, the temperature dependence of the electrical conductivity of both compositions displayed a linear relationship between $\ln(\sigma \cdot T)$ and $1/T$. For the 67 mol% TiO_2 melt the relationship $\ln(\sigma \cdot T) = 9.867 - 1778/T$ was determined. For the 73 mol% TiO_2 composition, the relationship was $\ln(\sigma \cdot T) = 9.896 - 1836/T$. These melts were modelled as mixed conductors (ionic and electronic) with activation energies of 0.15-0.16 eV. The electronic portion of the mixed conduction process was modelled by polaron hopping among the titanium ions.

A model was proposed for the current response to a stepped square wave voltage excitation. The initial and long-time values of the current response were used to calculate total ionic and total electronic transference numbers. These melts displayed 10-20% ionic conduction over this temperature range in which BaO was the primary ionic carrier.

As for the technical viability of titanium extraction by molten oxide electrolysis, the fact that the mode of conduction in these melts is not exclusively electronic is encouraging.

Thesis Supervisor: Donald Sadoway
Title: Professor of Materials Chemistry

Acknowledgements

This thesis is the culmination of many years of work. I could not have completed this project without the help and support of many people over the years. I want to thank:

Prof. Donald Sadoway for proposing the idea that motivated this work and for his guidance throughout.

The members of my thesis committee - Prof. Uday Pal, Prof. Harry Tuller, and Dr. Kevin Rhoads - who provided excellent suggestions for the analysis of the data and helped shepherd this document into its final form.

My group members, past and present, who have been a source of comradery as well as technical assistance: Kwang Kim, Heather Shapiro, Robin Michnick, Susan Schiefelbein, Toru Okabe, David Pratt, Mackenzie King, Steen Nissen, Minoru Nakajima, and Andrew Ducret.

The wonderful MIT undergraduates who assisted me in the lab and library: Jeremy Levitan, Kathryn Benedicto, Danielle Russell, Erin Lavick, Bill King, and Betsy Srichai.

Derek Johnson of Scribner Associates, for assistance with the software to run the 1260 and the 1286, and for generously giving of his time to help me design the experimental procedure for the electrical conductivity measurements.

Don Galler, for the loan of his digital oscilloscope and Dave Robertson, for the loan of his electrometer.

Those who read and edited my thesis, and particularly, Robin Michnick and Lena Fried who read this document repeatedly and made many valuable suggestions.

My sources of funding: the Ida Greene Fellowship; the Office of Naval Research; the Mining, Minerals, and Materials Research Fellowship; the National Defense Science and Engineering Graduate Research Fellowship; the GE Foundation Faculty for the Future Program; the American Association of University Women Engineering Fellowship; the Massachusetts Space-Grant Consortium Fellowship; and the Kahn-Rassmussen Environmental Program.

I would like also to acknowledge the tremendous gratitude I feel toward two people who went beyond the call of duty to help me accomplish this work. I am deeply indebted to:

Guenter Arndt, a master machinist, who was invaluable to me in the building and designing of my cells and so much of my equipment.

Dr. Kevin Rhoads, who wrote a number of computer programs to facilitate data collection and analysis, and who helped me develop the new measurement techniques that were at the heart of this project. Kevin has also been a wonderful teacher and mentor. Without him, this work would not have been possible.

I wish to thank three special friends who, having themselves been graduate students, were there to laugh, cry, and empathize with me: Ellen Arruda, Robin Michnick, and Joshua Musher.

Finally, I want to thank my family for their patience, love and support, and especially my husband, Jesse Fried, who gave me the courage to persevere.

אם תרצו אין זו אגדה
הרצל --

Table of Contents

Figures

Tables

Chapter 1: Introduction

1.1 Background

Titanium, the fourth most abundant element in the earth's crust, is endowed with an excellent strength-to-weight ratio and the ability to withstand high temperatures and corrosive environments. These characteristics make titanium eminently suitable for use in the aerospace and marine industries and in harsh chemical environments.

Titanium's properties could also be put to beneficial use in many other areas of civil aerospace and in automotive applications. Unfortunately, the high cost of extracting and processing titanium using current methods makes it very expensive: the price per pound of sponge titanium is currently approximately six times that of pure aluminum [1] and ten times that of steel. Therefore, titanium is used almost exclusively in high-value applications.

Since World War II, the Kroll and Hunter methods have been used to extract titanium. In these processes, a feedstock of titanium ore (TiO_2) is chlorinated in the presence of carbon to produce titanium tetrachloride ($TiCl_4$). The $TiCl_4$ is purified through fractional distillation before being reduced by magnesium (Kroll process) or sodium (Hunter process). The products of this batch operation are $MgCl_2$ and porous titanium metal called "sponge." To yield usable titanium metal, the sponge is crushed, washed with acid, and then rinsed with large quantities of water to remove residual chloride salts. After the sponge is cleaned and dried, it is vacuum arc melted to produce a titanium ingot. The Hunter and Kroll methods involve many separate steps, or unit operations.

Four factors contribute to the high cost of the Kroll and Hunter methods. First, these methods are energy intensive. Second, many of the unit operations are highly inefficient: for example, at least 15% of the $MgCl_2$ generated in the Kroll process cannot be recycled back to elemental magnesium and chlorine. Third, these methods require a number of reagents, many of which are dangerous or difficult to handle[1], namely: chlorine gas, carbon (in the form of coke), magnesium (or sodium), and large volumes of acids and water, adding direct and indirect costs to the processes. Finally, because many of the compounds used in these methods are corrosive, the lining of the reactors in the plant must be replaced on a regular basis, further increasing production costs.

Professor Donald Sadoway of MIT has proposed replacing the Kroll and Hunter methods with a new electrolytic method for the direct extraction of titanium metal from its ore [2]. This electrochemical method, molten oxide electrolysis, involves passing an electric current through molten TiO_2 to produce liquid titanium metal at one electrode and pure oxygen gas at the other electrode.

This new titanium extraction process has at least three advantages over the existing methods. First, molten oxide electrolysis is expected to be more environmentally benign than the Kroll and Hunter processes, producing only pure oxygen gas as its byproduct without yielding toxic intermediate compounds. Second, electrochemical extraction is expected to consume 65% less energy per pound of titanium produced than the Kroll and Hunter processes. The third advantage of molten oxide electrolysis is that the titanium produced is in liquid form, making it suitable for direct casting into metal parts or ingots at low cost.

Additional benefits from this technology may be possible. The development of this relatively environmentally safe electrochemical method for the production of titanium could lead to new technologies for the clean electrolytic extraction of other metals, and new techniques for the remediation of a wide variety of toxic wastes. In addition, this technique could be used for local lunar production of oxygen: a reliable source of lunar

---

[1] The intermediate titanium tetrachloride is highly reactive with moisture. Magnesium metal is susceptible to spontaneous combustion. Gaseous titanium tetrachloride, carbon monoxide, and chlorine can all cause environmental damage.

oxygen is critical both to support human life and provide fuel for vehicles operating from the moon. Some lunar regolith--the layer of loose rock that forms most of the moon's surface--contains a high concentration of titania-bearing ilmenite [3] (a mixed ore of titanium and iron oxide) which would provide an ideal lunar feedstock for the production of oxygen by electrolytic separation.

Whether the proposed process will work depends on the capability of titanium-bearing electrolytes to be ionic conductors. Little information is available at this time on the conductivity of molten titanates. The minimal data on the electrical characteristics of molten titanium dioxide are inconsistent. Some work has been done showing that solid titanium dioxide is not an ionic conductor, but rather an electronic conductor with a high degree of intrinsic semiconduction; other reports claim that molten TiO_2 is an ionic conductor. The lack of reliable data is understandable because of the difficulties in handling molten TiO_2, which melts at 1840°C and is very corrosive [4].

1.2 Summary of Previous Research on Titanate Conductivity

1.2.1 Solids

At room temperature, the most common form of solid titanium dioxide, rutile, is an intrinsic semiconductor [5]. If oxygen is removed from rutile by heating it in hydrogen or a vacuum, n-type semiconducting behavior is induced [6].

1.2.2 Melts

1.2.2.1 Titania Melts

Van Arkel *et al.* [4] report a conductivity of 10 S/cm for TiO_2 at its melting point. The uncertainty in this value is estimated to be 50%. Van Arkel reasoned that liquid titanium dioxide is semiconducting due to oxygen deficiency. Klinchikov *et al.* [7] reported the conductivity of molten titanium dioxide to be 35.8 S/cm, but no details of the experimental method or estimates of the error were given.

1.2.2.2 Titaniferrous Slags ($Ti_xFe_yO_w$)

TiO_2 occurs naturally with iron oxide in the ore ilmenite. Information from research on titanium dioxide-rich titaniferrous slags may suggest the electrical characteristics of pure molten titanium dioxide although the precision of this data is questionable.

In investigations of high titanium dioxide slags, Desrosiers *et al.* reported electronic conduction. This study found that slags containing 66-79 wt% TiO_2 exhibited conductivity in the range 24-57 S/cm. Despite notable iron content in the slag, the authors concluded that the conductivity was a function of the oxidation state of titanium. The mechanism was postulated to be a random walk of electrons between tetra- and trivalent titanium dispersed in the melt. Desrosiers further reported that these slags behave as simple, regular solutions and that oxygen pressure and temperature changes affect conductivity. The measured conductivity was fitted to an Arrhenius-type model. Once again, large uncertainties were encountered and the accuracy of the data was only 40%. This work provides an order of magnitude, but the precise values of the conductivity of pure titanium dioxide are still obscure since these samples contained oxides of other elements such as iron, aluminum, calcium, magnesium, silicon, and chromium.

Mori [8], working with iron titanates, reported that at 1430°C a melt of 68 mol% TiO_2 has a specific electrical conductivity of 50 S/cm. Unlike Desrosiers, he reported little variation in conductivity with temperature. Mori also found that conductivity decreased as titanium dioxide content increased up to 40% TiO_2. Beyond this threshold content, the conductivity increased with TiO_2 content.

Denisov *et al.* [9] reported conductivities of 150-180 S/cm for iron titanate slags with TiO_2 contents of 80-90%. Based on the smooth rise in conductivity of these slags when melting and a weak temperature dependence, they postulated that the conductivity of pure titanium dioxide is semiconducting as a result of oxygen deficiencies.

Bockris *et al.* [10] studied the binary silicate melts of lithium oxide, titanium oxide, and barium oxide. The free energy of activation for the conductance process involved the movement of cations from one interstitial hole in the silicate network to the next. A free energy of activation of 50 kcal/mol at 1800°C was reported for titanium dioxide. Bockris observed that the activation energy and pre-exponential factor decreased with metal oxide content in silicate melts.

1.2.2.3 Melts Containing Barium Oxide

Bockris reported that melts of $BaO\text{-}SiO_2$ systems were ionic. At 1750°C, silicates with BaO content of 17-35% displayed conductivity in the range of 0.04-0.6 S/cm. Bockris' conclusion that these melts were ionic was based on the following factors: the order of magnitude of the conductance; the positive temperature coefficient of conductance; the hundred fold increase in conductance after melting; and the observation that electrolysis obeys Faraday's law.

Bockris also reported that the free energy of activation for conduction in silicate binaries with alkali-earth oxides ranged from 15-35 kcal/mol. Conductance increased with alkaline metal oxide content.

1.2.3.4 Multi-Component Solids and Melts with Titanium Dioxide

Zheng *et al.* [11] studied the conduction of TiO_2 sintered with other oxides. A sample of composition 20 mol% Li_2O, 7 mol% BaO, and 73 mol% TiO_2 was reported to have a conductivity of 0.004 S/cm at 300°C.

In the Klinchikov paper cited above, a conductivity of 25.6 S/cm was reported for MgO-TiO_2, a conductivity of 17 S/cm was reported for $2MgO$-TiO_2, and a conductivity of 13.5 S/cm was reported for $3MgO$-TiO_2. The temperature of these measurements was not specified. Musithin *et al.* [12] examined mixed oxides of composition Al_2O_3 (43-45%), MgO (6%), CaO (41-44%) and TiO_2 (10-15%). They reported conductivities in the range of 0.1-1.0 S/cm between 1400 and 1500°C. They also found that the binary of 20%CaO-80%TiO_2 had a conductivity of 12 S/cm, independent of temperature.

There are conflicting hypotheses concerning the mechanism of conduction. Furthermore, few direct measurements have been made on molten titanates and, of the ones reported, the accuracy is low. This review of the literature indicates the lack of consistent, accurate information on the mechanism for, and magnitude of, conductivity of titanate melts.

1.3 Project Summary

1.3.1 The Candidate Mixture: TiO_2-BaO

The first step toward the design of an industrial process for molten oxide electrolysis is the selection of a supporting electrolyte, composed of titanium dioxide and one or more additional compounds. The purpose of this research was to determine the magnitude and nature of the conductivity of a candidate titanate electrolyte mixture and postulate possible conduction mechanisms.

Two criteria were used in the selection of the counter-oxide: (1) the counter-oxide must form a eutectic mixture with TiO_2, lowering the melting point of pure TiO_2 from 1840°C to below 1500°C (a practical maximum temperature for both laboratory and industrial operations); and (2) the counter-oxide must be thermodynamically more stable than titanium dioxide, so that electrolysis of the mixture of the two oxides would result in the preferential deposition of titanium. Table 1.1 lists candidate counter-oxides.

Only Li_2O and BaO satisfy both criteria. However, the difficulty of containing Li_2O [4] made BaO the appropriate counter-oxide for this study. The temperature limitations of the equipment restricted the compositions that could be studied to those within the range of 67-73% TiO_2 (See Figure 1.01.) Specifically, the two end members of the eutectic window tie-line (67 and 73 mol% TiO_2) were investigated in detail.

1.3.2 Summary of Results and Accomplishments

1.3.2.1 Conductivity Measurements

The major accomplishment of the experimental work done for this thesis is the accurate measurement of the electrical conductivity of molten TiO_2-BaO as a function of temperature and composition. This research is the first step in the systematic study of the electrical properties of binary solutions of TiO_2 and its counter-oxide. Understanding these properties is a prerequisite for determining the viability of molten oxide electrolysis of titanium.

The electrical conductivity as a function of composition and temperature, along with the activation energy, liquid-solid comparisons, and transference numbers are used to investigate the atomistic nature of these melts. The melt was found to be a mixed conductor which displayed an inverse relationship between conductivity and TiO_2 content. Barium contributed to ionic conduction and titanium to electronic semiconduction.

1.3.2.2 New Measurement Technique

The development of two new electrical conductivity measurement techniques for liquids was critical to the success of this work. The first was the coaxial-cylinders electrode (CCE) technique which is calibration-free over its range of accuracy. The second technique, which was ultimately used to measure the conductivity of binary solutions of molten TiO_2-BaO, was the four-point crucible-cell technique using matched calibration standards. Calibration with a standard possessing a conductivity close in magnitude to that of the system under investigation provides the correlation of cell factor with conductivity, enabling the crucible cell to produce accurate measurements of electrical conductivity.

1.3.3 Organization of the Thesis

Chapters 2 and 3 discuss the theory and background of the total conductivity measurement. Chapter 4 describes the theory behind the transference number measurements. Chapter 5 reviews the experimental protocol. Chapter 6 presents the data analysis, the results, and investigates models. Chapter 7 provides suggestions for the expansion and continuation of this research.

Table 1.1 Candidate Counter-Oxides for Titanium Electrolysis

COMPOUND	STABILITY W/R/T TiO_2	EUTECTIC TEMPERATURE
Al_2O_3	greater	1700 C
B_2O_3	less	450 C
BaO	**greater**	**1312 C**
BeO	greater	1670 C
CaO	greater	1460 C
FeO	less	1305 C
Li_2O	**greater**	**1030 C**
MgO	greater	1620 C
Sc_2O_3 (price prohibitive)	greater	1560 C
ThO_2	greater	1650 C
Y_2O_3	greater	1580 C

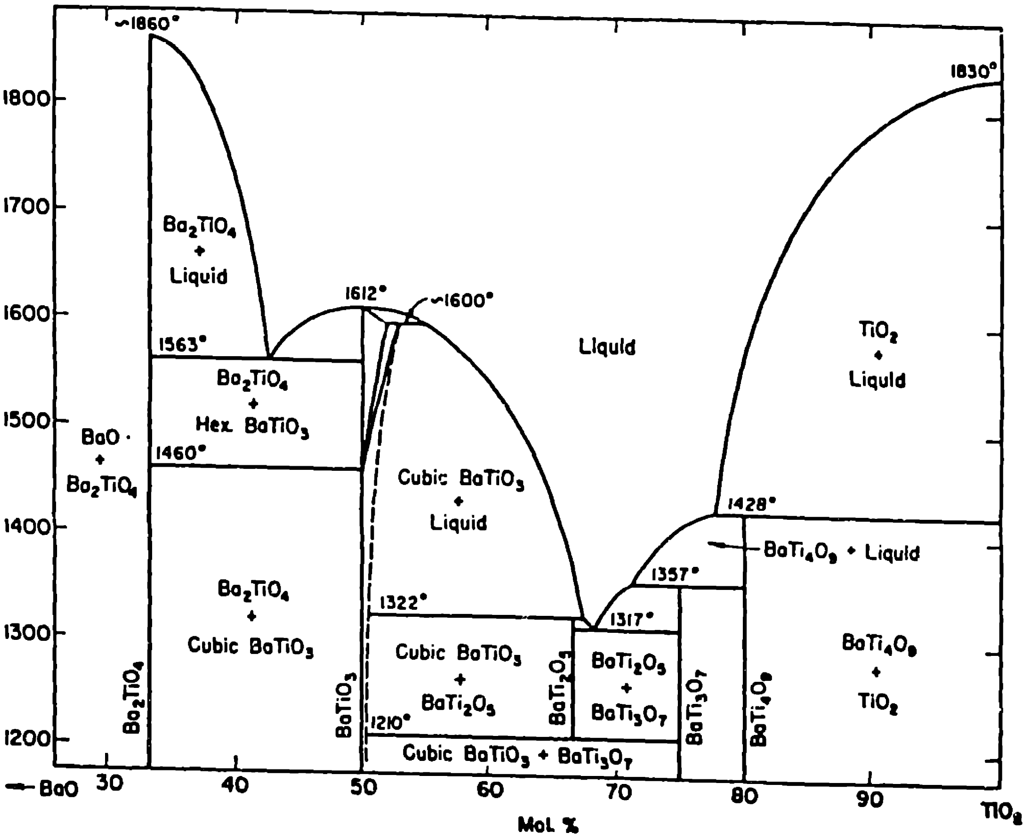

Figure 1.01: Phase Diagram for BaO-TiO$_2$ [13]

Chapter 2: Toward Accurate Electrical Conductivity Measurements of Molten Titanates

This chapter examines how electrical conductivity measurements are performed. Determining electrical conductivity requires (1) knowledge of the cell factor, or current path of the system and (2) measurement of the sample's resistance. While the basic relationship between resistance and conductivity appears simple, an accurate technique requires appropriate selection of cell design, excitation signal, and data processing protocol. Limitations of the materials of containment as well as the sensitivity of the device used to measure the electrical signal add further complexity when designing a conductance cell. Cell choice requires a systems perspective--the recognition of the interconnectedness of the above listed factors. Sections 2.1 and 2.2 examine the meaning of cell factor, its influence on choice of the cell design, excitation signal, and the data analysis technique.

2.1 Cell Factor and Cell Design

2.1.1 Cell Factor

Electrical conductivity cannot be measured directly. Rather, it must be derived by measuring the material's resistance. The "cell factor," or electric geometry of the conductivity cell, is required to determine conductivity values from measured resistance. The relationship among resistance, conductivity, and cell factor is governed by the following equation:

$$R=(1/\sigma)\,G \qquad (2.1)$$

R is the resistance in Ω

σ is the electrical conductivity in S/cm

G is the cell factor in cm^{-1}

The cell factor is proportional to the length of the path travelled by the current and inversely related to the cross-sectional area over which the current travels. The cell factor depends on the dimensions of the cell, the placement of the electrodes, and the conductivity of the medium being measured. Loosely speaking, the cell factor captures that part of the measured resistance that is not attributable to the inherent resistivity of the material but rather to the quantity and dimensions of the material sample whose resistance is being measured.

For solids, determination of the cell factor is straightforward when the current path is confined to a simple shape. For example, a solid in electrical isolation that is shaped as a cylinder and has electrodes covering the end faces will have a cell factor related to the simple geometry. The current is constrained to follow parallel paths between the electrodes, therefore, the cell factor takes the form of the distance between the electrodes divided by the cross sectional area of the end faces and can be directly calculated. (See Figure 2.01) Since the cell factor of this cylinder is the same regardless of the material measured, the cell factor can be referred to as the "cell constant."

For liquids, the cell factor is also represented by the current path length divided by the current's cross sectional area. However, only when a liquid can be shaped and contained entirely by a dielectric material of simple geometry can the cell factor be derived from the specimen geometry. Building a conductivity cell entirely out of dielectric materials is often difficult. As a result, the measurement of the electrical conductivity of liquid specimens generally requires control of the current path either geometrically (examples include concentric spheres, interdigitated electrodes, or coaxial-cylinders electrode), or physically by shaping the current path with some dielectric material (examples include guarded electrodes and the capillary style cell.)

In liquids which are not entirely contained by a dielectric, the cell factor is found by calibrating the cell with a solution of known conductivity. The standard solution's resistance is measured and the cell factor for the particular geometry calculated using

Equation (2.1). After the cell factor is determined experimentally, the cell can be used to measure the electrical conductivity of an unknown liquid. The resistance of the test liquid is then measured and the conductivity calculated using the cell factor. It is assumed that the electrodes are perfectly conducting (or at least significantly more conductive than the melt), an assumption that is valid for some, but not all, combinations of electrode and melt materials. More importantly, it is assumed that the current path is invariant from calibration standard to the test solution.

2.1.2 A Brief Review Of Existing Conductivity Cells for Liquids

Electrical conductivity cell designs for liquids can generally be divided into two classes: low-accuracy and high-accuracy cells. Low-accuracy cells do not control the current path, resulting in inaccurate measurements. High-accuracy techniques include methods that maintain a constant cell factor through an invariant current path from calibration standard to test medium.

Low-accuracy techniques do not geometrically or physically control the current path, therefore, the cell factor varies with the solution conductivity. Only when the conductivity of the calibration solution closely matches that of the solution under investigation will a "low-accuracy" technique furnish "high-accuracy" results. Under these circumstances, the cell factors of the calibration standard and the unknown solution are nearly identical because the current path does not significantly vary from liquid to liquid.

High-accuracy designs, on the other hand, generally have well-defined, reproducible current paths regardless of the conductivity of the sample. The most common techniques rely on dielectric materials to shape the current path and to control stray currents. High-accuracy cell designs for liquids include the capillary cell, the u-tube cell, interdigitated electrodes, and guarded electrode designs. In all of these cells, the current path is confined between the electrodes in a reproducible manner. For these cells, the cell factor is constant because the current path measured with the calibration solution represents the current path for a test solution regardless of its conductivity over a wide range of conductivities.

2.1.3 Development of the Coaxial-Cylinders Electrode Technique

To build a high-accuracy cell for the measurement of the electrical conductivity of molten titanates, a variety of dielectric materials was tested. Unfortunately, all the high-temperature dielectrics examined failed to maintain their mechanical integrity in the presence of the molten titanates. Alumina, magnesia, hot pressed boron nitride, and Sialon[2] all suffered severe attack in molten TiO_2-BaO.

Because of the lack of available dielectric materials, none of the traditional high-accuracy techniques could be deployed for the measurement of the conductivity of molten TiO_2-BaO. To resolve this problem, a new technique utilizing a moveable pair of coaxial, cylindrical electrodes was developed [14] and is shown in Figure 2.02. In the coaxial-cylinders electrode (CCE) technique, the solution impedance (which includes several components) is measured at multiple immersion depths and a differential calculation is used to extract the melt resistance. Provided the electrodes are kept a sufficient distance from the crucible wall and floor[3], most of the current between the electrodes moves radially. In addition to the radial current between the inner and outer electrode, there is a non-radial, constant fringing field at the bottom of the electrodes.

---

[2] Sialon is a high temperature, commercial ceramic composed of silicon nitride, aluminum nitride, aluminum oxide, and silicon oxide. Consolidated Ceramics Products, Blanchester, OH.

[3] The point at which the electrodes too closely approach the crucible floor is determined from the deviation from linearity of the plot of conductance versus depth of immersion. This deviation occurs because the bottom fringe field has been perturbed and is no longer constant for every depth of immersion. Two times the inter-electrode spacing is recommended as the distance of closest approach to the floor.

The mathematical details of the calculation of the conductivity from resistance at a variety of depths of immersions are discussed in Appendix A.

2.1.3.1 Advantages of the Coaxial-Cylinders Electrode Technique

The coaxial-cylinders electrode design offers several advantages. First, this cell design requires no dielectric materials to contact the melt, relying on cell geometry to reproducibly control the current path among solutions. This electrode can be fabricated out of metal and deployed in corrosive liquids. Second, because this is a differential method, the precise melt level need not be known. This approach is particularly useful for conductivity measurements at high temperatures where the melt level cannot be determined visually. In addition, over the applicable regime of melt conductivities (discussed below), the experimental cell factor matches the theoretical cell factor making calibration unnecessary for certain ranges of melt conductivity.

2.1.3.2 Certification of the Coaxial-Cylinders Electrode Technique

A CCE fabricated of platinum inner and outer electrodes was used to certify this technique with aqueous KCl solutions. The electrical conductivity of 1.0, 0.1, and 0.01 demal solutions of KCl were measured with an accuracy of ± 0.5%. The accuracy of this design over the conductivity range 0.1 S/cm through 0.001 S/cm was established by this procedure which was reported by Fried, *et al.* [15].

2.1.3.3 Range of Applicability of the Coaxial-Cylinders Electrode Technique

While the coaxial-cylinders electrode technique has been certified as a method for measuring electrical properties with great accuracy, the range of use is limited[4]. For

---

[4] The coaxial cylinders technique was certified for use with liquids of conductivity up to 0.1 S/cm. Attempts to certify this technique with standard solutions of 2-3 S/cm were unsuccessful. The limits on the range are based on the use of metal electrodes of laboratory scale. Larger,

very resistive melts, the cell factor of laboratory-scale coaxial-cylinders electrodes results in system resistances that were too large to be measured accurately by instruments such as the Solartron 1260 Frequency Response Analyzer. Indeed, it has been reported that dielectric measurements with the coaxial-cylinders electrode in butyronitrile (conductivity of 10^{-8} S/cm) were extremely inaccurate using the coaxial-cylinders electrode technique [16].

At the "high" end of the conductivity spectrum, the CCE cannot accurately measure melts of conductivity greater than 0.1 S/cm even with considerable refinement of the basic mathematical analysis, consideration of second order effects, and deviation from lumped circuit behavior [17]. Based on the high conductivities of molten titanates reported in the literature, their measurement was anticipated to be out of the range of the coaxial-cylinders electrode. An attempt to measure the electrical conductivity of molten TiO_2-BaO with the CCE produced noisy results from which the temperature dependence and activation energy could not be reliably calculated. (See Figure 2.03.) Similarly, molten oxides of other transition metals, such as iron oxide (electrical conductivity ranging from 100-300 S/cm [18]), cannot be measured accurately with the coaxial-cylinders electrode. The following section proposes explanations for the limited range of this technique.

2.1.3.4 Limitations of the Coaxial-Cylinders Electrode Technique

2.1.3.4.1 Breakdown of Equipotentiality

The conductivity range over which the coaxial-cylinders electrode can be successfully deployed has an upper bound defined by the condition that the electrodes behave as equipotential surfaces; that is, the electrode conductivity is sufficiently greater than that of the melt. When this condition is not met, the conductance cell cannot be

---

thicker electrodes could be used to extend the range of applicability of this technique.

modelled with simple lumped elements and a transmission line model must be used. The transmission-line model recognizes that the electrode is not equipotential, causing the current density at any location to vary with immersion. With the latter model, the mathematical simplicity of the CCE is lost. Additionally, "grand fringing," described below, can no longer be ignored. When grand fringing is included in the model, a single short-circuit measurement used to eliminate the electrode resistance is no longer valid for all depths of immersion.

2.1.3.4.2 The Problem of Fringing Fields

The coaxial-cylinders electrode have a recognized fringing field between the bottom of the inner and outer electrodes. If this fringe is constant, its contribution to an impedance measurement of the radial conductance can be eliminated by examining total impedance at a variety of depths and then determining the differential conductance. (See Appendix A.)

There is an additional current path beside the radial path between the electrodes and the bottom fringe path: the "grand fringing path" in which the current leaves the outside of the immersed portion of the outer electrode and travels to the bottom of the inner electrode. Because the grand fringe emanates from the immersed portion of the electrode, changes in the depth of immersion alter this fringing field. Unlike the contribution of the bottom fringe, the contribution of the grand fringe to the radial conductance cannot be removed by differential analysis.

The portion of the current that travels directly between the electrodes, and the portions of the current that participate in each type of fringing will depend on the relative magnitude of the electrical conductivity of the electrode versus the conductivity of the medium. More precisely, the critical parameter is the resistance of the electrode relative to the resistance of the melt. For example, for an electrode with resistance similar to that of the medium, grand fringing offers a significant alternate current path. However, if the electrode resistance is considerably lower than that of the specimen, grand fringing is less important. When a portion of the current taking the "grand fringing" path is anticipated to be significant, care must be exercised to ensure that the electrodes are calibrated with a standard whose conductivity is close to that of the material under investigation.

2.2. The Electrical Measurement

2.2.1 The Excitation Signal

Proper cell design allows accurate determination of conductivity from resistance. The measurement of resistance is the crux of an electrical conductivity determination and there are several ways in which the resistance of a test specimen can be measured. In its simplest form, resistance can be measured by applying Ohm's law to a system in which the voltage and current are known.

$$R = V/i \qquad (2.2)$$

R is the resistance in Ω

V is the voltage in V

i is the current in A

Voltage and current can be measured using either DC or AC techniques. Selection of the appropriate excitation signal and analysis depends on the modes of conduction in the material and the electrode-electrolyte interface. AC-based techniques such as Electrochemical Impedance Spectroscopy (EIS) are the most flexible and generally used for ionic materials.

EIS is the method of choice for ionic liquids in the presence of blocking electrodes where a high-impedance, interfacial double-layer capacitance develops. Electrodes are termed "blocking" when the formation of a double-layer at the electrode-electrolyte interface inhibits the flow of current from the electrode to the electrolyte below the decomposition or faradaic voltage. DC current cannot be coupled through a capacitor or double-layer below the decomposition voltage. Since a capacitor will respond to a time-varying signal, small AC excitations can be used to probe a system with blocking electrodes.

For systems with "non-blocking" electrodes, there is an alternate, low-impedance interfacial pathway between the electrodes and melt, and DC techniques are applicable. Low impedance interfaces are generally found in systems in which the melt is partially or completely electronic, or in cells that have a common element in the melt and electrode.

In this investigation, molybdenum electrodes in a chloride melt used for calibration behaved as blocking electrodes. In the TiO_2-BaO melts, molybdenum electrodes were found to be non-blocking[5].

2.2.2 The Equivalent Circuit

Whatever the excitation signal used, it is imperative that an appropriate equivalent electrical circuit model be selected to accurately interpret the system's response to the excitation signal. In particular, when using EIS, which detects the phase shift from all the reactive components in the system, there may be many circuit elements contributing to the overall system response to the signal. To successfully isolate the resistance of a test specimen, an equivalent circuit was used to understand each element's contribution. Figure 2.04 gives the equivalent circuit used for measurement of electrical conductivity of molten barium titanate with the CCE. While there is a "universal" equivalent circuit that represents all possible physical characteristics of the system, the more useful equivalent circuit reduces the universal equivalent circuit to one that reflects the dominant

---

[5] The molybdenum electrodes were non-blocking with respect to electrons but blocking with respect to barium, oxygen, and titanium.

elements for a test system. For example, when using the CCE as described in Appendix A to measure the conductivity of conductive melts, there is capacitance between the electrodes. Since the melt is "conductive," the impedance due to this capacitor is negligible over the frequency range studied. This capacitor behaves essentially as an open circuit and is omitted from Figure 2.04. In contrast, if this system were more resistive, the impedance of this capacitor would be significant while the lead wire resistance becomes negligible.

In a DC (zero frequency) measurement, the contributions of reactive circuit elements (capacitance and inductance) which are detected by the phase shifts they induce are not observed at steady-state. As a result, steady-state DC measurements do not contain the response of solution capacitance, parasitic capacitance, or electrode inductance. One can conclude that the dominant equivalent circuit model for a system responding to a DC signal is generally simpler than one for the same system responding to an AC excitation. This simplification facilitates data analysis and reduces error. When the electrodes are non-blocking, solution resistance is easily and more accurately extracted from a DC measurement.

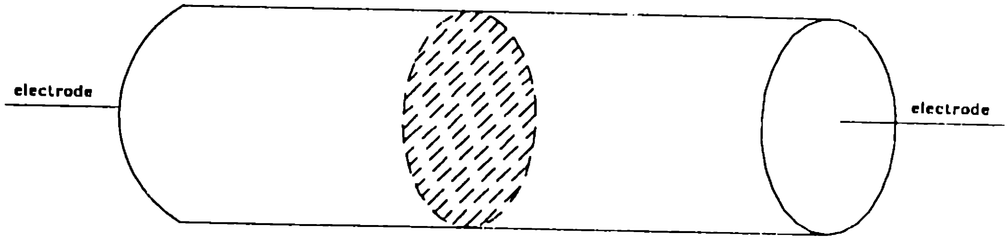

Homogenous Solid Cylinder
A = cross section = πr^2
G = cell factor = ℓ/A
$G = \ell/\pi r^2$

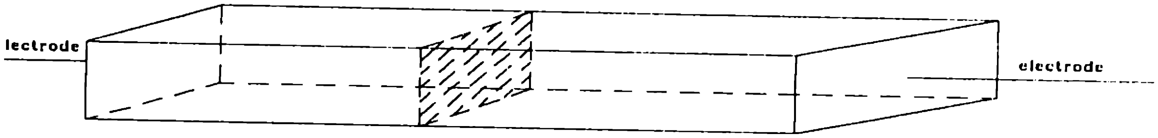

Homogenous Solid Rectangle
A = cross section = $h \bullet w$
G = cell factor = ℓ/A
$G = \ell/h \bullet w$

Figure 2.01: Cell Factors for A Solid Homogeneous Cylinder and Rectangle

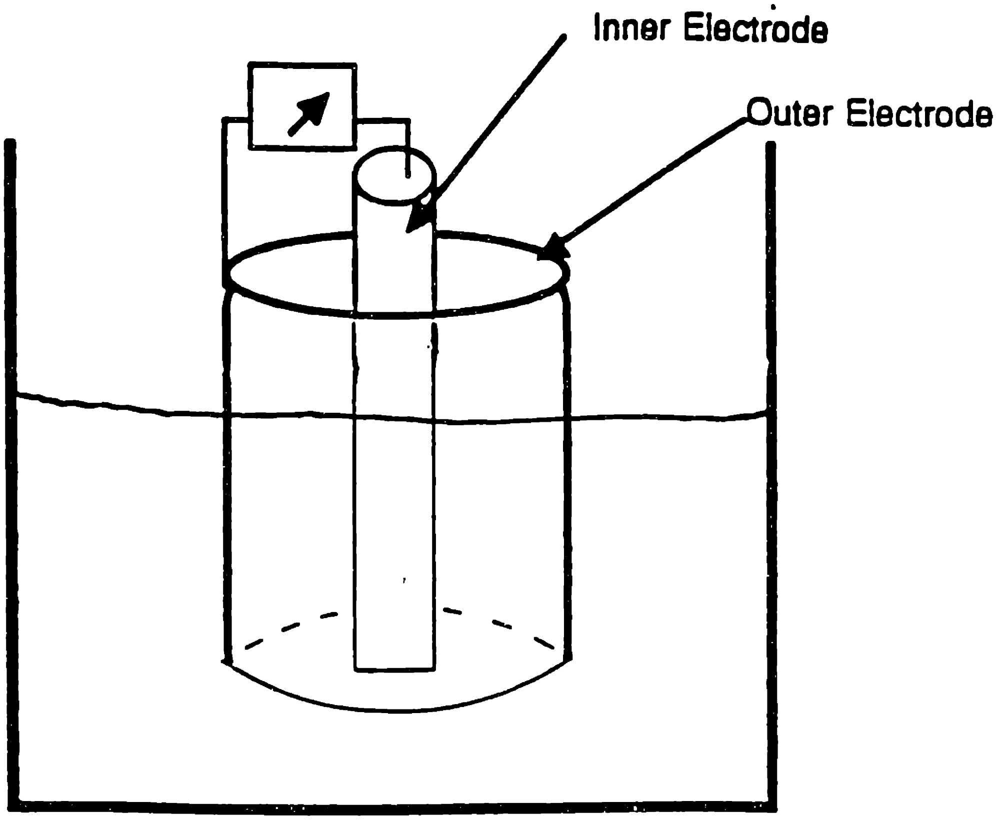

Figure 2.02: The Coaxial-Cylinders Electrode

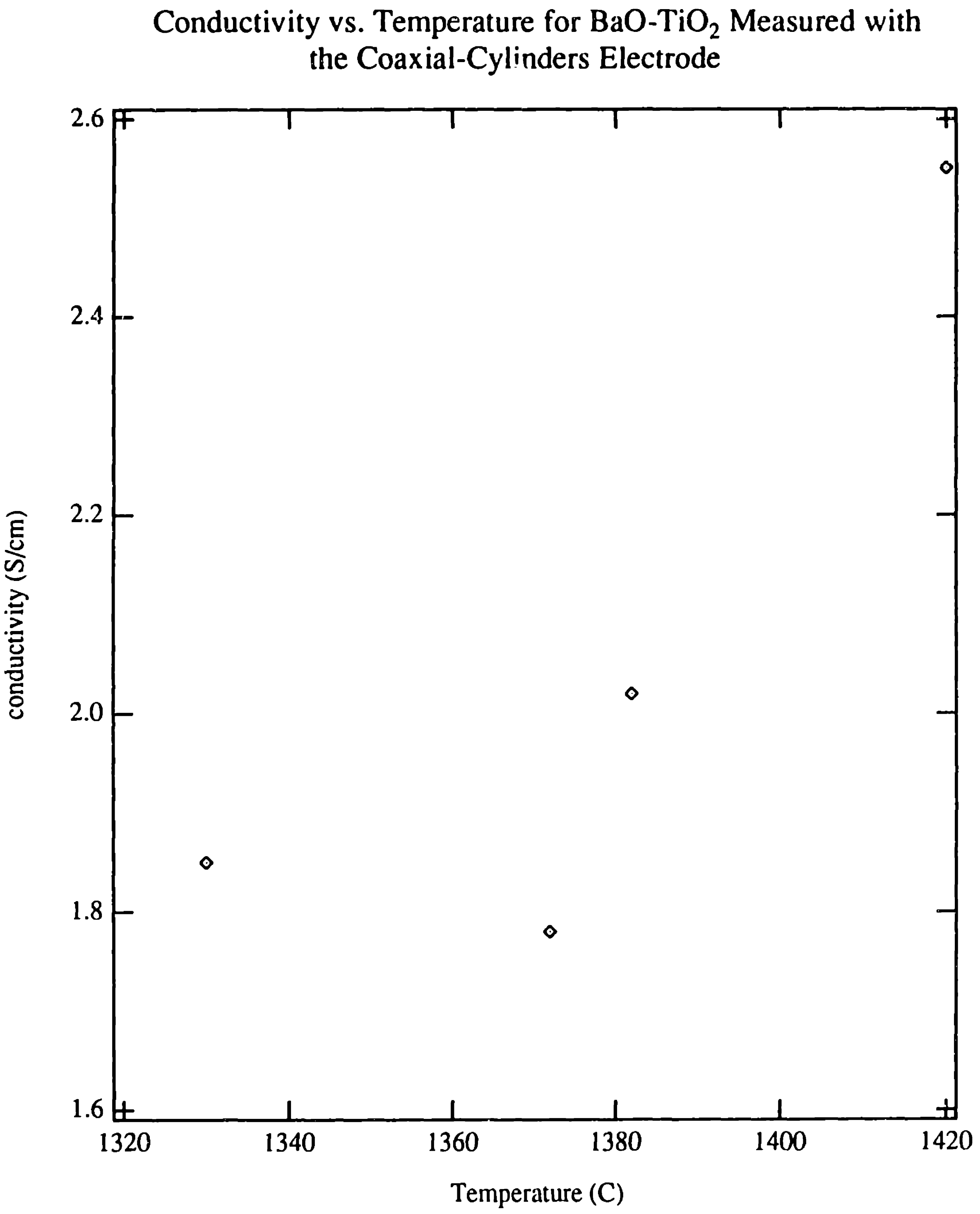

Figure 2.03: Electrical Conductivity of TiO_2-BaO (67:33 mol%) Measured by Coaxial-Cylinders Electrode

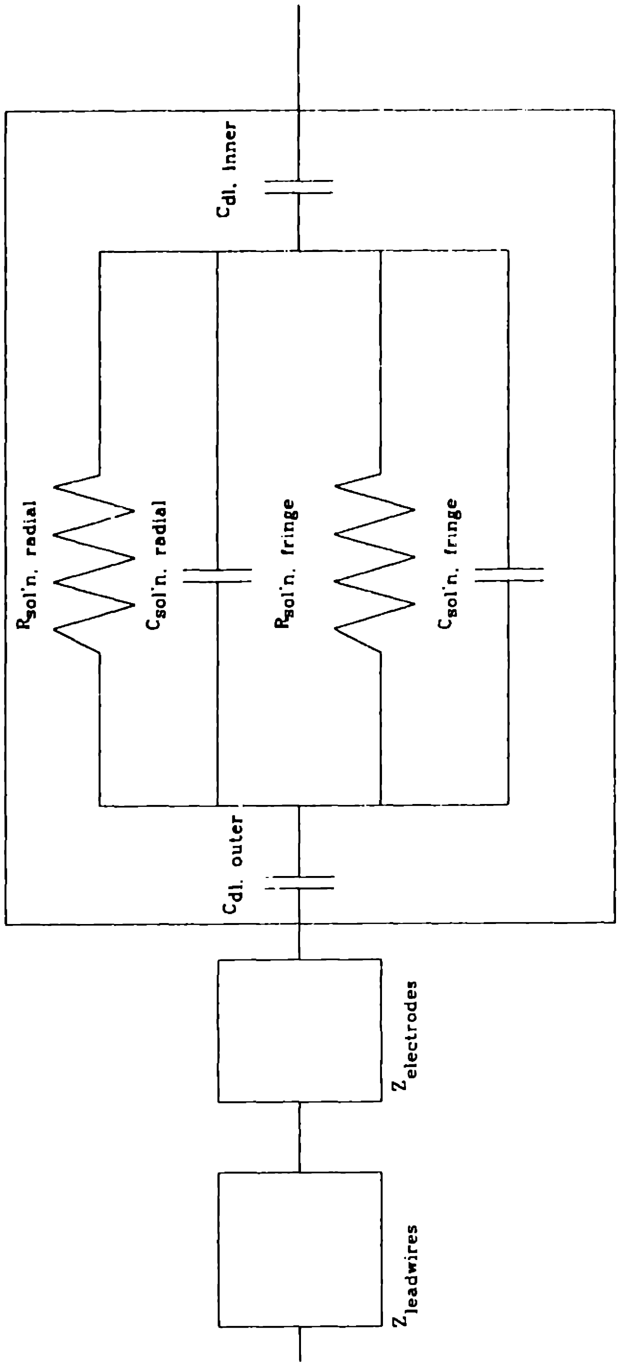

Figure 2.04: Equivalent-Circuit Model for EIS Measurements of Molten Oxides and Molten Chlorides Using Coaxial-Cylinders Electrode

Chapter 3: Development of the Four-Point Crucible-Cell Technique Utilizing Matching Calibration Standards

After the new coaxial-cylinders electrode technique proved inadequate for molten oxide measurements, a second new cell design and experimental protocol called the four-point crucible-cell technique with matching calibration was developed. This technique is capable of high-accuracy measurements in conductive and corrosive melts without the use of dielectric material. The following is a description of the background, theory, and deployment of this new technique for measuring total electrical conductivity.

3.1 The New Four-Point Crucible-Cell Technique

3.1.1 Crucible-Style Cells: Description and Background

The crucible-style cell consists of a crucible that functions both to contain the melt and as a current-injecting electrode and a center rod which acts as the second, current-injecting[6] electrode. The crucible-style cell has been used by Lovering *et al.* [19], Gale *et al.* [20], and Hives *et al.* [21] to measure electrical conductivity of melts. This design does not require any insulating material to contact the melt. The electric field distribution in the crucible cell is similar to a coaxial-cylinders electrode with an inner electrode that is shorter than the outer electrode. Like the coaxial cell, the crucible cell exhibits radial symmetry. However, grand fringing does not exist in a crucible-style cell when the crucible sits in an insulating tube.

Historically, the crucible-style cell has been a low-accuracy cell design because of a poor understanding of the importance of the cell factor in the measurement of conductivity [22]. As with all cell designs for liquids, current flows from one

---

[6] Both electrodes that are active are termed "current-injecting," but from a technical perspective, one electrode injects the current while the other receives it.

electrode to the other based on the shape of the electrodes, the conductivity of the medium, and the conductivity of the electrodes. Unlike a capillary style cell, the current path in a crucible-style cell is not controlled physically by dielectric materials. Furthermore, unlike concentric sphere electrodes, there is no simple geometry that can be used to constrain and reproduce the flow of the current between the electrodes. For a reproducible crucible cell geometry, the current distribution in a crucible style cell is a function of the relative conductivities of the electrode material and the solution.

In a crucible cell, the cell factor must be determined from calibration with a solution of known conductivity. Typically, a single calibration with a standard of known conductivity has been used. However, in a crucible cell, the electric field and the resulting current path and cell factor, depend on the relative conductivities of the electrode material and the liquid. If provisions are not made to assure that the current path in the calibration standard is the same as the current path in the test medium, the calibration procedure is inaccurate.

The failure to recognize the importance of cell factor and its variation as a function of medium for crucible cells is widespread throughout the literature. For example, Ogino *et al.* [23] measured the electrical conductivity of calcium fluoride in two identical crucible cells, one made of molybdenum, the other of graphite. At 1500°C, Ogino found a 30% difference in the "conductivity" of the melt when the molybdenum crucible was used in place of the graphite. One would not expect the current distribution nor the cell factor to be the same for two different crucible materials. Yet Ogino used a single cell factor for the calculation of conductivity in each crucible. Furthermore, the magnitude of the inaccuracies increased because of Ogino's choice of calibration standards. Ogino used molten KCl (conductivity around 2 S/cm) to calibrate his cells. In this case, the fact that calcium fluoride has a conductivity around 6.5 S/cm [24]-- nearly three times greater than that of the calibration medium -- was not taken into account. Because of this difference in conductivity between the calibration standard and the test medium, the cell factor determined by "calibration" was not representative of the current path in the test medium.

3.1.2 Conductivity-Dependent Cell Factor

In the present investigation, it was recognized that the crucible-style cell can be used to obtain accurate values of conductivity. The key to successful utilization requires that the variation in cell factor with medium and operating conditions be accounted for or controlled. When the conductivity of the calibration standard matches the conductivity of the test medium and the same crucible cell geometry and material are used, the cell factor determined through use of a calibration standard is an accurate representation of the current path in the test medium. Multiple calibrations can then be used to establish the general relationship between cell factor and conductivity when identical matching of the conductivities is not possible. Provided that all calibrations are conducted with the same volume of solution, the relationship between cell factor and solution conductivity can be established. The conductivity-dependent cell factor, $G(\sigma)$, can then be used to determine the conductivity of an unknown medium of the same volume. For a crucible cell, the general relationship between resistance and conductivity (equation (2.1)) is expressed:

$$R = (1/\sigma)\, G(\sigma) \qquad (3.1)$$

R is the measured resistance in Ω

σ is the electrical conductivity in S/cm

$G(\sigma)$ is the conductivity-dependent cell factor in cm^{-1}

The high-accuracy four-point crucible cell technique developed for this research accounts for the variation in current path with the solution contained in the cell. Calibration solutions are chosen to match, or bracket, the conductivity of the test medium. Once the set of cell factors of the standards are measured, the calibration curve which correlates cell factor with conductivity can be established for a given crucible cell, electrode material, and electrode geometry.

The cell factor (a single scalar) summarizes the geometric shape of the current path (a vector field) whose shape is a result of the applied electric field. The electric field is defined by the boundary conditions which depend, in part, on the conductivity of the medium. Provided the boundary conditions do not change, the shape of the electric field will be identical among solutions with the same conductivity, regardless of the nature of the charge carriers.[7] The relationship between cell factor and electric field is seen in the field expressions of voltage and current.

$$V = \int \mathbf{E} \bullet d\mathbf{l} \tag{3.2}$$

$$i = \iint \mathbf{J} \bullet d\mathbf{A} \tag{3.3}$$

V is the voltage in V[8]

E is the electric field vector in V/m

dl is the differential vector length element in m

i is the current in A[9]

J is the current density vector in A/m^2

dA is the differential vector area element in m^2

---

[7] For a mixed conductor, all the charge carriers will experience the same total electric field and have the same shape current paths, although the magnitudes of the currents may be different.

[8] The limits of the voltage integral are the positions of the two voltage measuring electrodes.

[9] The current integral is integrated over the surface of either current injecting electrode.

From the constitutive equation for conduction, in the absence of diffusion and convection [25] the current density is expressed as:

$$\mathbf{J} = \sigma \mathbf{E} \tag{3.4}$$

σ is the total electrical conductivity[10] in S/m

The expression for current (equation (3.3)) can be rewritten as

$$i = \sigma \iint \mathbf{E} \cdot d\mathbf{A} \tag{3.5}$$

The ratio of the voltage to the current is the resistance:

$$R = (\int \mathbf{E} \cdot d\mathbf{l}) / \sigma (\iint \mathbf{E} \cdot d\mathbf{A}) \tag{3.6}$$

The comparison of equation (3.6) with equation (2.1) shows that the cell factor is given by the expression:

$$G = (\int \mathbf{E} \cdot d\mathbf{l}) / (\iint \mathbf{E} \cdot d\mathbf{A}) \tag{3.7}$$

The dependence of the electric field (and thus cell factor) on the conductivity of the medium is explored in detail in the following sections.

For the conductivity-dependent cell factor to give accurate results, it is critical that the integrals **dl** and **dA** in equation (3.7) be constant and the total cell geometry invariant. Practically speaking, this means the melt depth for each solution and the relative positions of all the electrodes must be invariant.

---

[10] For a mixed conductor $\sigma_{total} = \sigma_{ionic} + \sigma_{electronic}$.

3.1.2.1 Introduction to the Derivation of the Dependence of Cell Factor on Electric Field

In the above section, the relationship between cell factor and electric field was derived and the dependence of cell factor on the shape of the current density vector which in turn depends on the shape of the electric field was demonstrated. In general, since an electric field has both spatial and temporal dependencies, the relationship between cell factor and electric field is more completely expressed as:

$$G = \left(\int \mathbf{E}(r,\phi,z,t)\bullet \mathbf{dl}\right)/\left(\iint \mathrm{E}(r,\phi,z,t)\bullet \mathbf{dA}\right) \qquad (3.8)$$

In the following sections, the nature of the electric field is examined and it is shown that when all the boundary conditions for the systems are specified there exists only one electric field in the system. Furthermore, the relationship between the shape of the electric field and the conductivity of the melt in this boundary-value problem will be demonstrated.

3.1.2.2 System Definition and Assumptions

To define the electric field, it is necessary to specify the system and its boundaries. For the measurement of the cell factor using chloride melts and the subsequent determination of the total conductivity of the molten oxides, the system is the volume of melt between the electrodes, excluding the double-layer. The electrode-electrolyte interface, known as the double-layer, serves as the boundary. (Figure 3.01 illustrates the system and its boundaries.) The system consists only of bulk solution.

Although the double-layer is not part of the system, it contributes to the boundary conditions. The excitation signal used in these experiments, a triangle wave of magnitude 0.1 V[11] and a slew rate of 3 V/s, is sufficiently small in amplitude and fast in frequency

---

[11] The applied voltage is well below the decomposition voltage for BaO or TiO_2.

to couple current through the double-layer without perturbing its uniformity. It is assumed that the double-layer chemistry and electrical behavior are invariant with position along the electrode-electrolyte interface for each individual electrode[12]. Furthermore, it is also assumed that the electrode's resistivity is the same for both the oxide and chloride systems.[13]

3.1.2.3 Governing Field Equations

Maxwell's laws and the relevant constitutive materials laws are the points of departure for the examination of the electric field in this system. Here it is assumed that the propagation of electromagnetic waves can be neglected and, therefore, use of the electro-quasistatics (EQS) field model is valid. The EQS approximation gives the following two equations [25]:

$$\nabla \times \mathbf{E} = -\partial \mathbf{B}/\partial t \approx 0 \qquad (3.9)$$

$\mathbf{E}$ is the electric field vector in V/m

$\mathbf{B}$ is the magnetic flux density in Wb/m^2

$\partial \mathbf{B}/\partial t$ is the rate of change of the magnetic flux density in Wb/m^{2}s

When $\nabla \times \mathbf{E} \approx 0$, a potential, Φ, can be defined such that

$$\mathbf{E} = -\nabla \Phi \qquad (3.10)$$

Φ is the potential in V

---

[12] This does not mean that all electrodes must have the same interfacial characteristics as every other electrode. In fact, the interface for the active and passive electrodes are expected to be quite different.

[13] While the resistivity of the molybdenum electrode will change with temperature, the magnitude of the resistivity of the electrodes is five orders smaller than that of the melt, allowing minor changes in the electrode's conductivity with temperature to be ignored.

Other field laws are simplified by examining the time constant for dielectric relaxation. The time constant for net free-charge in the system is found from the ratio of ε (the dielectric constant in F/m) to σ (the total conductivity in S/cm). Using a conductivity of 4 S/cm and an ε of $100\varepsilon_0$ [14] for the titanate melts, the time constant for dielectric relaxation (the lifetime of a net free-charge in this medium) is on the order of 5×10^{-12} seconds, short enough to eliminate the need to consider net free-charge. A similar calculation for the time constant of dielectric relaxation for the chlorides, based on an average dielectric constant of $5\varepsilon_0$ [26] is found to be around 2×10^{-13} seconds. The net free-charge density and its time rate of change are effectively zero for this system:

$$\rho_{free} \approx 0 \qquad (3.11)$$

$$\delta\rho/\delta t \approx 0 \qquad (3.12)$$

ρ is the free-charge density in C/m^3

$\delta\rho/\delta t$ is the rate of change of free-charge in C/m^{3}s

With these approximations, Maxwell's equations for the electric displacement density and current density are reduced to:

$$\nabla \bullet \mathbf{D} = \rho_{free} \approx 0 \qquad (3.13)$$

$$\nabla \bullet \mathbf{J} = -\delta\rho/\delta t \approx 0 \qquad (3.14)$$

D is the electric displacement vector in C/cm^2

Combining equations (3.10) and (3.14) yields Laplace's equation as the governing differential equation for finding the electric field for this system:

$$\nabla^2 \Phi = 0 \qquad (3.15)$$

---

[14] A conservative estimate $100\varepsilon_0$ for ε assumes that the dielectric constant of the liquid is approximately equal to that of the solid. In fact, the dielectric constant of a liquid is expected to be much smaller than that of a solid, making the dielectric relaxation time even shorter.

3.1.2.4 The Existence of a Single Electric Field

The existence and uniqueness theorem for Laplace's equation states: for fully defined boundary conditions there exists only one potential, Φ, that both solves Laplace's equation (equation (3.15)) and satisfies the boundary conditions [27] [28]. The existence of a unique Φ solution is equivalent to the existence of a single, unique electric field in both the chloride and oxide systems. To demonstrate that the cell factors in the chloride and oxide systems are equivalent, it is only necessary to show that the boundary conditions are fully specified and spatially identical in both cases.

3.1.2.5 Boundary Conditions

The specification of one boundary condition on all surfaces meets the requirement of a "fully specified" boundary value problem. Boundary conditions for Laplace's equation take the form of either a specified potential, Φ, a specified normal component of the potential, $\partial\Phi/\partial N$, or a weighted sum of the two [29]. The boundary condition in both systems which can be specified on all surfaces is that the current is injected normally (perpendicular) at each melt surface.[15] The partial derivative with respect to the normal direction of the potential[16] is the fixed boundary condition and is expressed as:

$$\partial\Phi/\partial N = -\mathbf{E}_{\mathrm{surface}} = -\mathbf{J}_{\mathrm{injected}} / \sigma_{\mathrm{melt}} \qquad (3.16)$$

$\partial\Phi/\partial N$ is the normal derivative of the potential in V/m

$\mathbf{E}_{\mathrm{surface}}$ is the electric field vector at the surface in V/m

---

[15] The active electrode-electrolyte interfaces on the crucible and center electrode have a non-zero normally directed current. The passive electrode-electrolyte interfaces on the voltage sensing electrodes and the free surface of the liquid have a zero normally directed current.

[16] When the boundary condition is on the normal derivative of the potential, $\partial\Phi/\partial N$, Laplace's equation is said to satisfy the Neumann condition.

Furthermore, the electric field in this model has positional and time components that are separable because the boundary condition and the governing differential equation can be given as a single product of a time functionality and a space functionality. The boundary condition for both the oxide and chloride systems established through experimental design is represented as[17]:

$$\partial\Phi/\partial N\ (\mathbf{r},t) = \{\partial\Phi(\mathbf{r})/\partial N\}\ \{f(t)\} = -\mathbf{J}_{\mathrm{injected}}\ /\ \sigma_{\mathrm{melt}} \qquad (3.17)$$

Under certain circumstances the electrical properties of the double-layer, rather than the relative conductivities of the melt and the electrodes[18], may govern the shape of the injected current, $\mathbf{J}_{\mathrm{injected}}$, and the shape of the electric field. However, the assumption that the chemistry and electrical behavior of the double-layer at each electrode are invariant with position eliminates any positional effects of the double-layer on injected current in this system. When the electrode-electrolyte interface is invariant along each electrode, it cannot influence the spatial distribution of the electric field. The only effect of the double-layer is as a multiplicative term or amplification factor.[19]

These experiments were designed so that the interfacial behavior would be invariant along each electrode. Uniformity of the double-layer capacitors is maintained by limiting the magnitude of the excitation signal. If this experiment were carried out

---

[17] Equation (3.16) requires that the time function of each of the active electrodes are identical. This requirement is automatically satisfied when there are only two active electrodes and one of them removes all the current that is injected by the other.

[18] The effect of the electrode resistivity is not seen explicitly in this boundary condition. But the resistivity, in general, affects the shaping of the injected current, $\mathbf{J}_{\mathrm{injected}}$.

[19] In fact, examination of this system as a distributed circuit shows that it is possible to remove a uniform, interfacial impedance from the distributed circuit model and place it external to the field shaping portion of the model. Mathematically, any scale factor or time functionality of the electric field in equation (3.7) will cancel from the numerator and denominator and not affect the cell factor. Only boundaries that contribute to the spatial component of the electric field will be operated on in the spatial integral of equation (3.7) and influence the cell factor.

with an applied potential near the decomposition voltage of any of the elements present then Faradaic processes could occur and the assumption of uniformity of the interface would be difficult to meet.

The detailed nature of the double-layer does not influence the shape of the electric field for the system and assumptions presented here. Therefore, the interface models for the molten titanates, a resistor shunted by a capacitor, and for the chlorides, a simple capacitor, have no bearing on the geometric shape of the electric field. It is only the magnitude of the bulk conductivity of each melt that contributes to the geometric shaping of the electric field and ultimately the cell factor. For two melts with the same boundary conditions (in this case normal injected current) and the same bulk conductivity, the electric field will be identical.

3.1.2.6 Derivation Summary

It has been shown that the cell factor derives its value solely from the geometric shape of the electric field. For the system as defined and the assumption of electro-quasistatics, the field problem resolves to the Laplace equation with Neumann boundary conditions. The complete specification of the normal current on all boundaries guarantees a single, unique potential and thus electric field through the uniqueness and existence theorem. For these systems, assumptions, and experimental parameters, the shape of the normal current distribution and electric field was shown to depend on the bulk conductivity of the melt and is independent of the interface model.

3.1.3 Selection of Calibration Standards

The selection of proper calibration standards requires preliminary information about the magnitude of the conductivity of the test medium. Because only an approximate value of the conductivity is needed, a variety of techniques are available. For the investigation of the conductivity of molten titanates, approximate conductivity measurements were made with the CCE. Once the approximate conductivity of TiO_2-BaO was established, a matching standard solution was selected to determine the conductivity-dependent cell factor.

In addition to the criterion that the conductivity standards be as close as possible to the conductivity of the test medium, the four-point crucible-cell technique requires that the density of the standard be well known in order to reproduce the depth of the center electrode and the volume of the specimen. For the measurement of the electrical conductivity of molten titanates, a conductivity standard composed of mixtures of molten KCl and NaCl were selected. The exact compositions will be discussed in Section 5.1.3.1.

3.1.4 Design and Advantages of the Four-Point Crucible Cell

The accuracy of the crucible cell is further improved and the analysis simplified by replacing a two-point arrangement with a four-point one. In the four-point configuration, two additional electrodes, called voltage-sensing electrodes, are placed between the current injecting electrodes (the crucible and the center electrodes). See Figure 3.02. In this configuration, the crucible and center electrodes are dynamic, active interfaces where charge crosses the electrode-electrolyte interface. In contrast, the two voltage-sensing electrodes are static electrodes through which no current travels.[20]

The four-point measurement has been used by Hauser [30], Hogarth *et al.* [31], MacCallum *et al.* [32], Delahaye [33], Cutkosky [34], and Bruce *et al.*[35], and its advantages are well known. In its most common form, a current of known value is applied at the outer two electrodes and the voltage is measured at the

---

[20] The voltage sensing electrodes can only be considered "static" as long as the voltage measuring device to which they are attached has a high enough input impedance to prevent any current from travelling up these electrodes. This topic will be discussed in more detail in Chapter 5.

inner two electrodes. See Figure 3.03. Alternately, a known voltage can be applied at the outer electrode and the resulting current measured. Whether an applied voltage or current is used, the inner electrodes always measure the specimen's voltage [36]. Resistance is then simply the ratio of the measured voltage over the applied current. Care should be taken when using the four-point measurement technique with an applied current to prevent the applied voltage from exceeding the decomposition voltage of the sample.

In the four-point configuration, the voltage measured at the two static sensing electrodes contains no contributions from the resistance or inductance of the crucible or center electrodes nor their interfacial impedances. The exclusion of interfacial effects is particularly useful when measuring a bulk property such as electrical conductivity.

Because the crucible cell exhibits radial symmetry, the two sense electrodes must be located at different radii. If the sense electrodes are located at the same radius, they experience the same field and register no voltage drop across the melt. To increase the magnitude of the signal measured by the two sense electrodes it is desirable to maximize their radial separation without touching either the center or crucible electrode. Because of the steric hindrance of the ports on the cap of the conductance cell through which the voltage-sensing electrodes were fed, the voltage-sensing electrodes in these experiments were placed on opposite sides of the central rod. (See Figure 5.02.)

The four-point crucible cell can be designed with a variety of relative depths for the center and sense electrodes. It is important to have the two sense electrodes immersed to the same depth. To decrease the amount of non-radial, fringe field current measured by the sense electrodes, the center electrode is immersed more deeply than the voltage-sensing electrodes.

The advantage of the four-point crucible cell, in contrast to the coaxial-cylinders cell, is that it does not require any short circuit measurements of the current injecting electrodes' impedance.[21] In the four-point arrangement, the crucible and center electrode resistances and inductances are not part of the measurement.

3.2 Electrical Signal and Response

3.2.1 AC vs DC Excitation Signals

The four-point crucible cell can be deployed with a variety of excitation signals[22]. As discussed in Chapter 2, EIS is generally chosen for measurement in ionic solutions. Due to the limitations of the Solartron 1260,[23] DC techniques using the Solartron 1286 Electrochemical Interface[24] instead of AC techniques were adopted. The following sections will describe the selection of an appropriate excitation signal which depends on the blocking or non-blocking characteristics of the electrodes. The discussion will be limited to signals that can be generated by the Solartron 1286 Electrochemical Interface.

3.2.2 Magnitude of the Excitation Signal

For both AC and DC experiments, measurements must be conducted below the decomposition voltage of the melt to ensure that the melt composition is unaltered. At

---

[21] Inaccuracies in the short circuit measurement of the electrodes' resistance and inductance can be a significant source of error when using the CCE to measure the electrical conductivity of conductive melts.

[22] The choice of AC or DC techniques generally depends on the medium under study, the cell specifics, the nature of the electrodes, and the instrumentation available.

[23] The Solartron 1260 Frequency Response Analyzer is specified to an accuracy of only 10% for impedances of less than 0.1 Ω at all frequencies. For frequencies greater than 100,000 Hz, measurement of 0.1-1 Ω has the same specification. For a load of 0.1 Ω the 1286 is rated to a 0.3% accuracy at frequencies less than 1 kHz. In this experiment a ramp rate of 3 V/sec with an amplitude of ± 0.1 V (equivalent to a frequency of 8.3 Hz) was used.

[24] Solartron, Houston, TX.

827°C, the decomposition voltage of pure KCl is 3.41 V and that of pure NaCl is 3.22 V [37].

The magnitude of the excitation signal is also limited by the voltage at which the capacitance of the double-layer begins to deviate from linearity. Initial experiments using a 1.0 V excitation signal did not yield linear current and voltage responses, presumably because of the breakdown of the double-layer. Additionally, in chloride runs in which the applied voltage was above 0.1 V, a black layer was found at the interface of the white chloride salt and the molybdenum crucible. The inner rod also displayed surface roughening, indicating the possibility of an undesirable chemical reaction. Experiments determined that the excitation voltage for molten chlorides should be limited to 0.1 V.

3.2.3 Potentiostatic Excitation Signal for Non-Blocking Electrodes

When a low-impedance interfacial pathway is present for current to enter the melt from the electrode, a variety of excitation signals can be used to probe the melt. Under these circumstances, a simple DC square wave is sufficient for measuring the melt resistance. Alternatively, cyclic voltammetry in the form of a triangle excitation can be used to capture the melt resistance. For non-blocking electrodes, characterized by a low impedance interface and modelled by a simple resistor, a triangle excitation results in a triangular response. The equivalent circuit model for non-blocking electrodes is useful for the interpretation of the system response and is shown in Figure 3.04. Non-blocking electrodes are found in systems with electronic melts, or in systems of ionic melts where the electrodes contains a component of the melt. Molybdenum electrodes were non-blocking in the TiO_2-BaO melts studied during this investigation.

3.2.4 Potentiostatic Excitation Signal with Blocking Electrodes

Though the most common method for measuring electrical conductivity in the presence of blocking electrodes uses EIS, there are potentiostatic excitation signals that can also be used. The simplest DC signal-- the square wave--cannot be used to study a system such as an ionic melt that shares no elements with the electrode. Because of the formation of a double-layer capacitance at the electrode-electrolyte interface, polarization is the only result when a square wave is applied. No current flows into the melt so it is not possible to measure the responding melt voltage. Figure 3.05 shows the equivalent circuit model for an ionic melt with blocking electrodes.

The current through a double-layer, modelled as a capacitor, is governed by the rate of change of the voltage. The following equation gives the expression for current in a linear capacitor[25]:

$$i = C\,(dV/dt) \qquad (3.18)$$

i is the current in A

C is the capacitance of the capacitor in F

dV/dt is the rate of change in voltage in V/s

When there is blocking-electrode behavior, coupling the current from the electrodes to the melt requires applying a continuously changing voltage. To meet this requirement a triangular excitation was used for the calibration of the four-point crucible cell with ionic chloride melts and molybdenum electrodes. This form of cyclic voltammetry produces a time changing voltage so that the current is coupled through the double-layer capacitor and into the melt.

---

[25] The relationship between voltage and charge in a capacitor is

$$V = q/C$$

Assuming linearity, differentiation with respect to time gives the resulting relationship

$$i = dq/dt = C(dV/dt)$$

A DC measurement using a triangle wave in which the voltage varies with time is similar to an EIS measurement in which the signal frequency varies with time. Both time varying voltage (cyclic voltammetry) and time varying frequency (EIS) signals produce current through the double-layer capacitance while static DC voltage measurement below the decomposition voltage do not. The 1286 Electrochemical Interface (DC) can, therefore, be used to probe the resistance of ionic melts that are not accurately measurable with the 1260 Frequency Response Analyzer (AC). While the range of "frequencies" possible with the 1286 is narrow, the current and voltage ranges are considerably larger than the 1260.[26]

3.2.5 Voltage Control and the Shape of the Response

The Solartron 1286 Electrochemical Interface can be used as a potentiostat or galvanostat. Because the voltage-current characteristic of the system was unknown, it was not possible to fix the current and be certain that the applied voltage was below the maximum allowable to maintain linearity (see section 3.2.2.) As a result, the Electrochemical Interface was operated in potentiostatic (voltage control) mode and the current was allowed to vary to meet the voltage requirement. The 1286, acting as a potentiostat, generated a triangular voltage signal with an operator set maximum, minimum, and slew rate.

For ionic melts with a double-layer capacitance at the electrode-electrolyte interface, a triangular voltage excitation is applied between the crucible and center electrode. The current response through the melt is a square wave, and the voltage measured at the sensing electrodes is also a square wave. In a system with an additional, or alternate, low impedance interfacial route, such as an electronic melt, a triangular voltage excitation produces a triangular current wave and triangular melt voltage response.

---

[26] The 1260 Frequency Response Analyzer has a range of ± 3.0 V and ± 60 mA. The 1286 Electrochemical Interface can produce ± 12.8 V and ± 2.0 A.

Figure 3.06 illustrates the voltage-current response in a system with blocking electrodes and Figure 3.07 for the current and melt voltage response of a system with non-blocking electrodes.

The use of the Electrochemical Interface (1286), rather than the Frequency Response Analyzer (1260) has the additional advantage that square wave excitation and the resulting current response can be used to examine the type of the charge carriers in a material. Chapter 4 will examine this technique in detail.

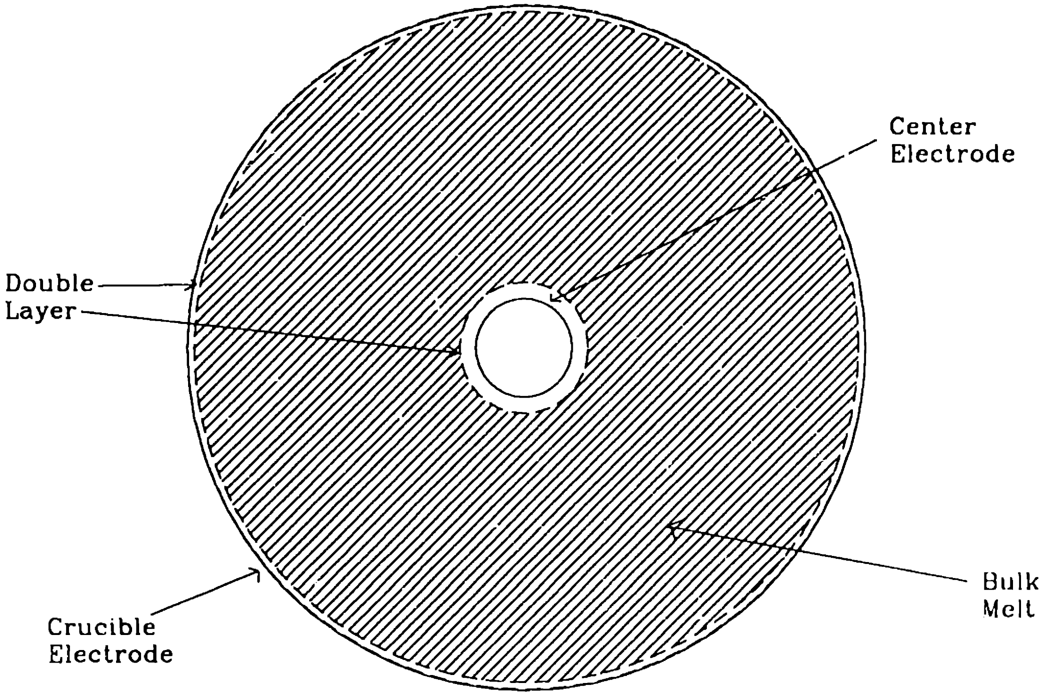

Figure 3.01: System and Boundary Definition for the Cell Factor Derivation

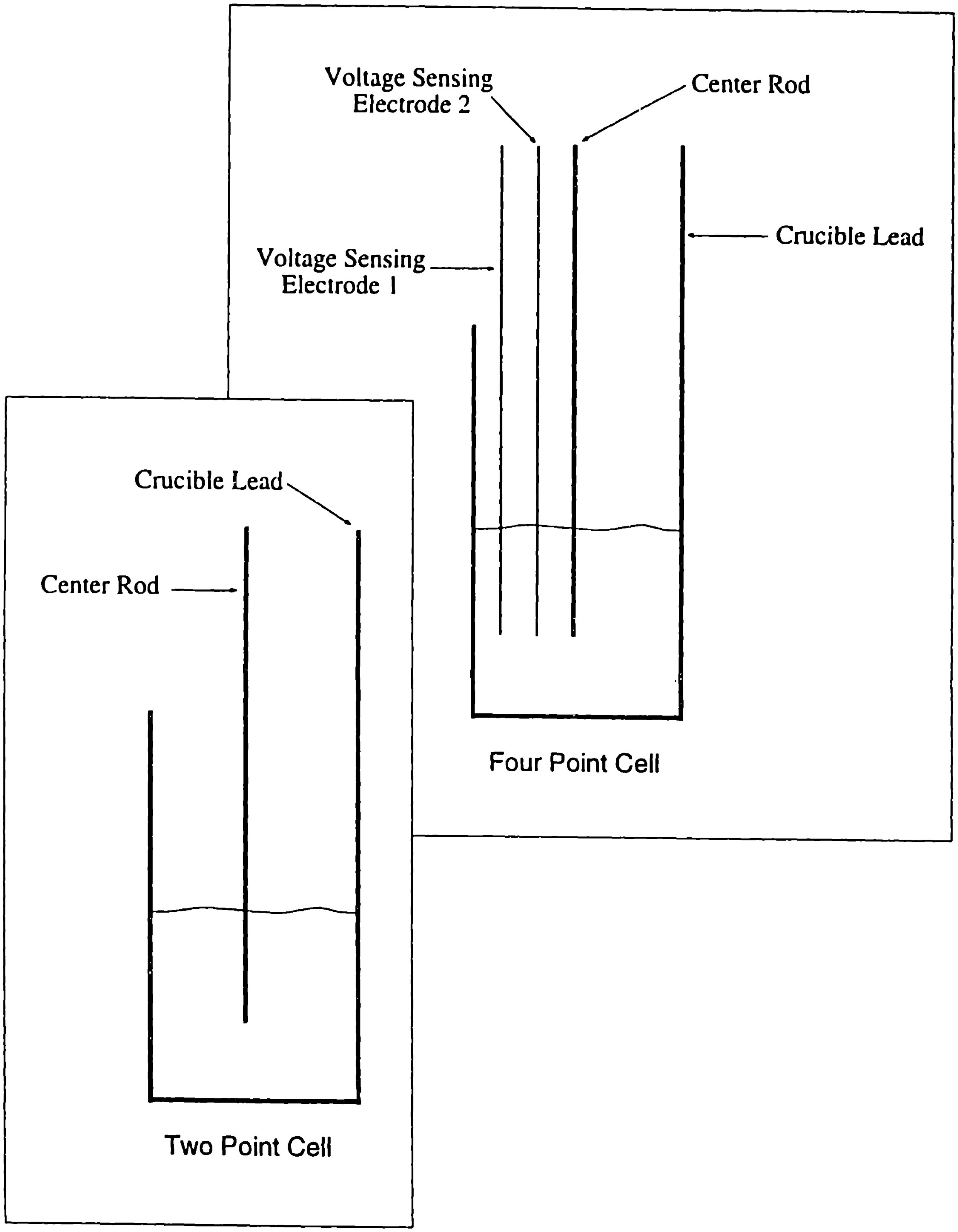

Figure 3.02: Two-Point Crucible Cell and Four-Point Crucible Cell

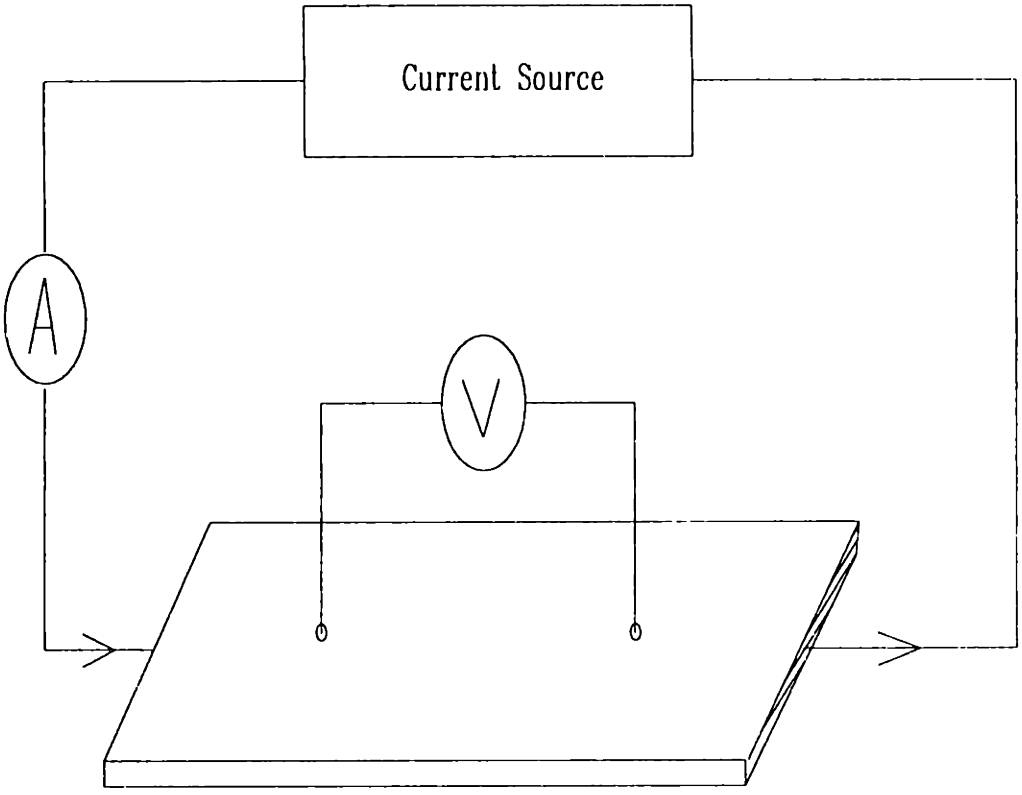

Figure 3.03: Voltage and Current Measurements with a Four-Point Cell

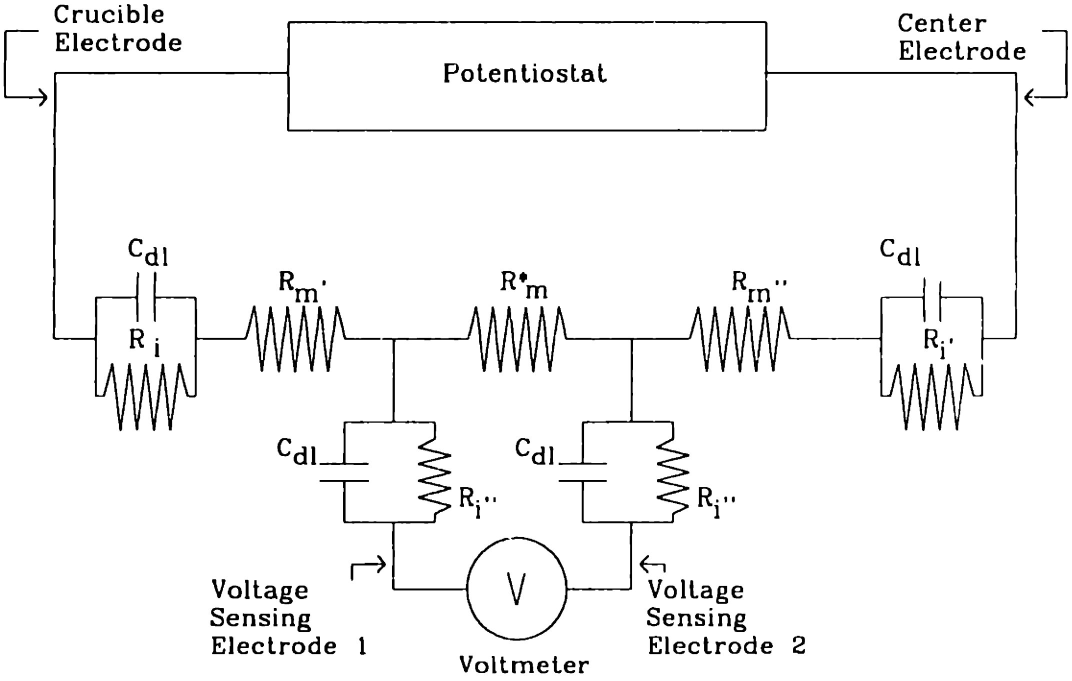

Figure 3.04: Equivalent Circuit for Four-Point DC Measurements with Non-Blocking Electrodes

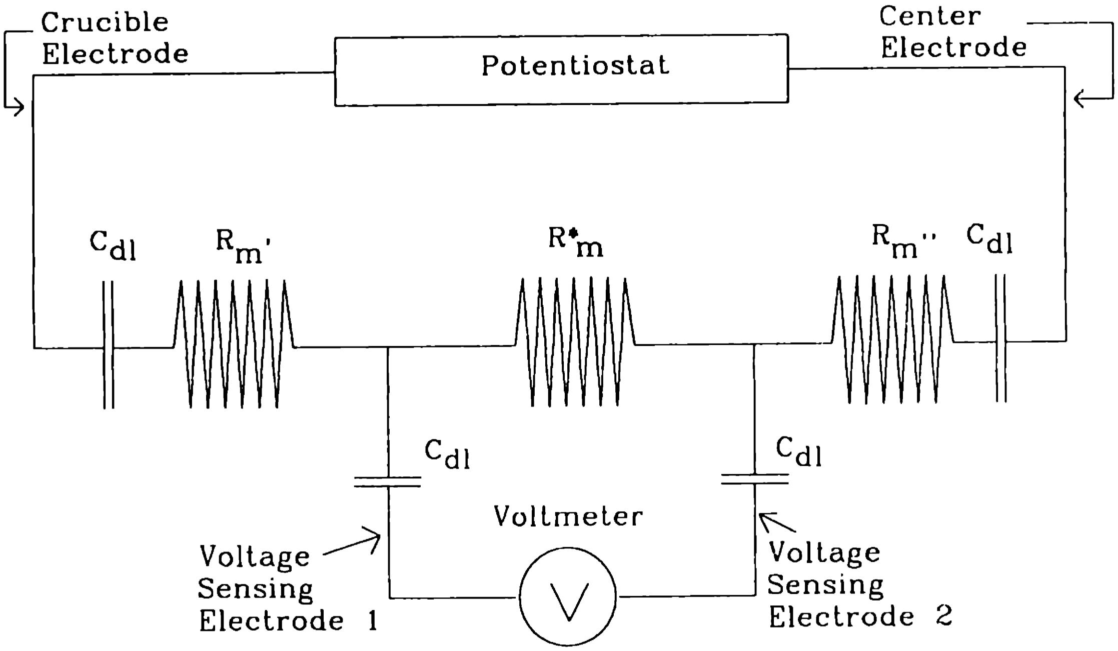

Figure 3.05: Equivalent Circuit for Four-Point DC Measurements with Blocking Electrodes

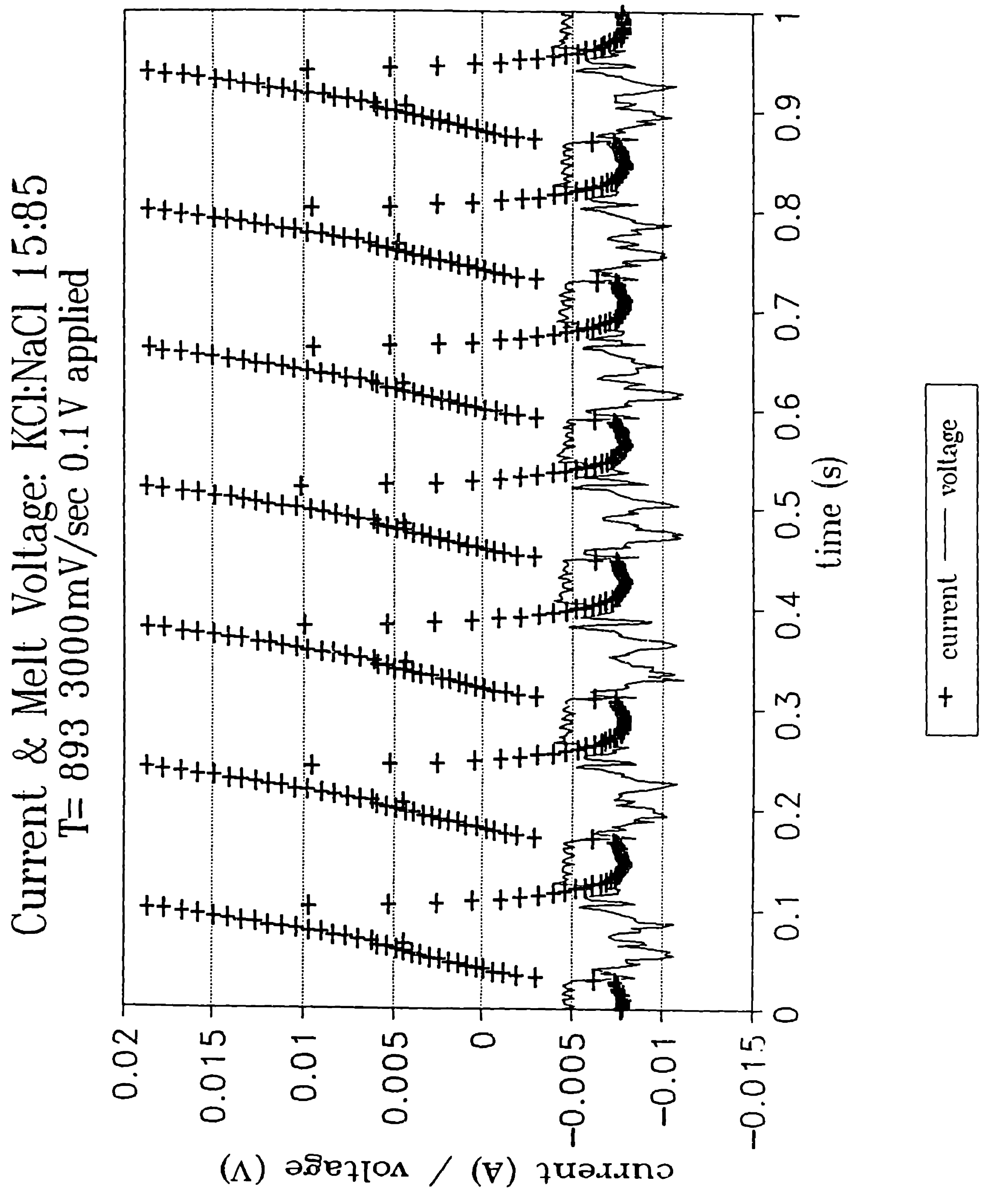

Figure 3.06: Current and Melt Voltage Response to a Triangular Excitation Voltage in a System with Blocking Electrodes

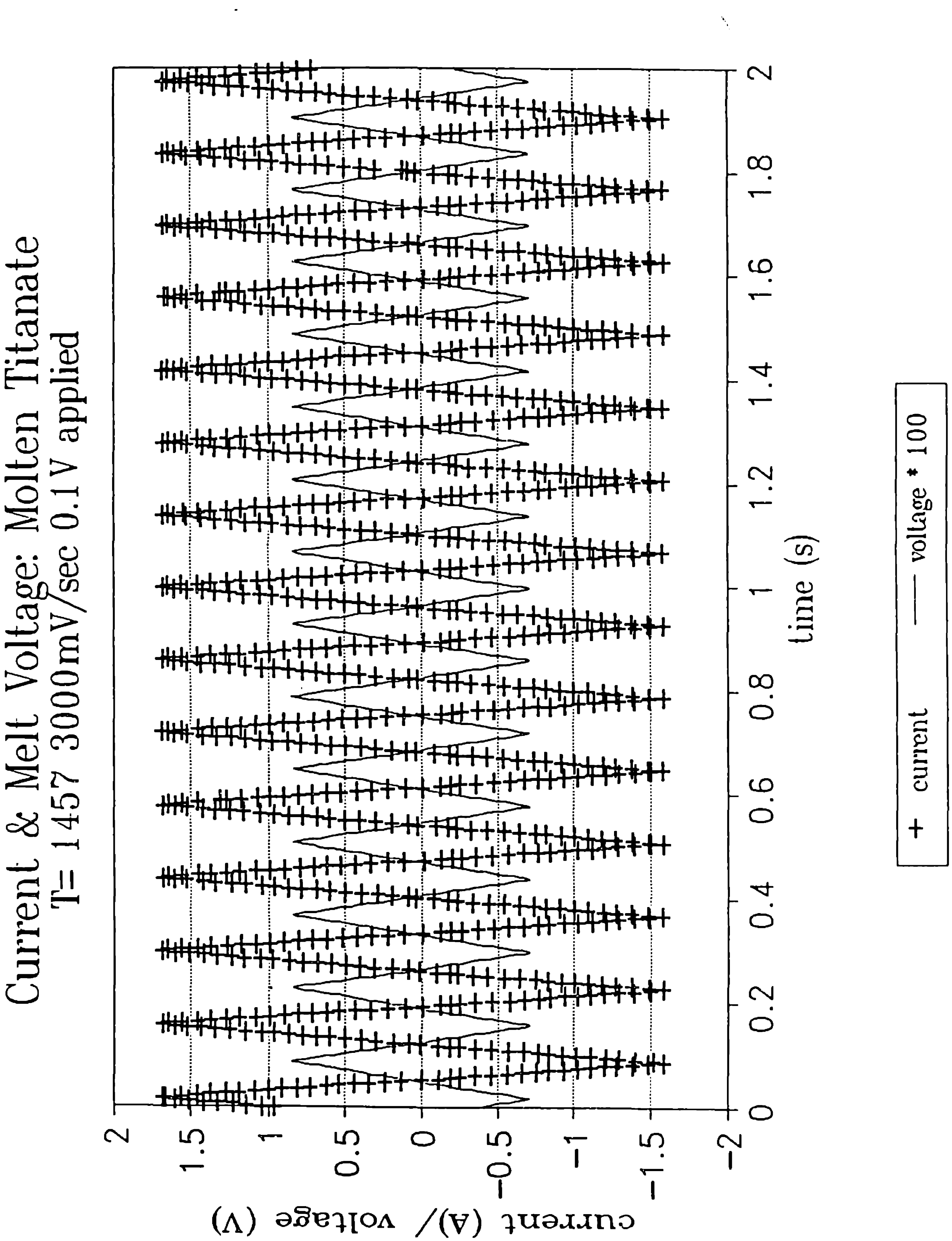

Figure 3.07: Current and Melt Voltage Response to a Triangular Excitation Voltage in a System with Non-Blocking Electrodes

Chapter 4: Stepped Potential Experiments for the Determination of Transference Numbers

In the last chapter, DC methods for the measurement of total conductivity were explored. Along with total conductivity, it is often important to know the mechanism of conduction in a material. While AC measurements are useful for measuring total conductivity, the response of a material to a DC square wave of amplitude less than the decomposition potential can be used to determine if a material is ionic, electronic, or a mixed conductor. In this chapter, a quantitative model for the square wave decay method for the determination of transference numbers is developed.

4.1 Description of the Square Wave Technique

Monitoring current as a function of time when a stepped potential (square wave) is applied to a material is useful in determining the mechanism of conduction. Transference numbers, which indicate the fraction of the total conductivity arising from specific species [38], can be calculated from the relative values of the initial and long-time ($t\rightarrow\infty$) values of the current in response to an applied square wave voltage.

In general, for an electronic conductor, after any initial (very fast) double-layer charging, when a DC voltage is applied, a constant current is observed through the material. When the voltage is removed, no current is detected beyond the double-layer discharge. The magnitude of the electronic conductivity can be directly calculated from the ratio of steady-state current and applied voltage.

When this same DC square wave is applied to an ionic material, the double-layer is very quickly charged and current ceases to flow. The electrode interfaces of ionic melts polarize in response to the application of a square wave. Removal of the applied voltage results in the double-layer discharge and relaxation of the ions from polarization.

When the stepped potential is applied to a mixed conductor, the current displays some decay with time, on a scale of minutes to hours, until a long-time, non-zero current is reached. The electronic component of the total conductivity in a mixed conductor can be calculated from the ratio of the long-time, steady-state current to the applied voltage.

The behavior of the current response after removal of the applied potential may be used to confirm the presence of mixed conduction. A material with significant mixed character exhibits an initial non-zero melt current of the opposite sign after the square wave is removed. This current results from the re-equilibration of the concentration gradient of ions which had developed as a result of the square wave application. A purely electronic material, on the other hand, displays only a very fast double-layer discharging.

4.2 Literature Review

DC square waves are frequently used to determine mode of conduction. This technique does not require a particular cell design. The key requirement is the ability to monitor the melt response (voltage or current) during and after the application of a square wave. This DC decay technique has been used to measure transference numbers. I.I. Olsen *et al.* [39] concluded that the DC polarization technique for transference number measurements is as effective as the Hittorf (Turbandt), NMR and Radio Tracer techniques, and Concentration Cell methods for measuring transference numbers. This technique has been applied to polymers ([40], [41], [42]), oxygen sensors [43], and mixed oxide conductors such as $Li(Na)_xMo_2O_x$ [44]. Furthermore, one can monitor either the voltage, or the current,[27] decay as a function of time to obtain information about the specimen's charge carriers [45].

---

[27] The melt current and voltage are related through Ohm's Law (V=iR). For this work, the current was easier to measure and its decay was monitored.

While the DC decay technique has been exploited by many scientists, the underlying theory for the mixed conductor has never been explicitly developed. Models such as that of Colson, *et al.* [44] for the time-dependent current response are phenomenological[28] and not rigorous.

4.3 Drift and Diffusion Model

In this section, a model, based on an examination of all of the sources of current[29] in the system, is proposed to explain the time-dependence of the current measured in a mixed conductor subjected to a stepped potential with electrodes that are non-blocking to electrons, but blocking to ions.

In this model, the current response of a mixed conductor to an applied square wave is divided into three regimes. In the first regime[30], $t=0^+$, only electronic ohmic and ionic ohmic currents are present. In the second regime, called the transient regime, the effects of an ionic diffusion current as well as the electronic and ionic ohmic currents contribute to the total measured current. The third regime is the long-time, $t\rightarrow\infty$, regime in which the ionic diffusion and ionic drift currents are equal in magnitude and opposite in sign everywhere on a point-by-point basis, and only the ohmic electronic current is detected in the external circuit.

---

[28] Colson's model for the time dependent current response in a mixed conductor involves a single exponential function. However, the present investigation determined that even in a simple, one-dimensional Cartesian model, the expression for current in the transient regime is composed of a sum of an infinite number of exponentials, resulting in an infinite number of time constants.

[29] Bulk capacitive currents in this system are assumed to be negligible beyond a very short charging transient because $BaO\text{-}TiO_2$ is a conductive medium. The time for double-layer charging is extremely short relative to the time scale of the experiment. As a result, double-layer capacitive currents can also be neglected.

[30] Technically, in the very early stages of the $t=0^+$ stage, the double layer and bulk capacitors are charging. Since the time constants for charging are on the order of micro-seconds and nanoseconds, respectively, they need not be considered in the discussion of the $t=0^+$ regime which is on the order of tenths of second.

4.3.1 System Definition

The first step in this derivation is to define the system that is being modelled. The system boundaries for the molten TiO_2-BaO are located beyond the electrode-electrolyte interface, known as the double-layer. (Figure 4.01 illustrates the system and its boundaries.) The double-layer is excluded from the system, which consists only of the bulk solution. Furthermore, the double-layer chemistry and electrical behavior are assumed to be invariant with position along the electrode-electrolyte interface for each individual electrode[31]. As long as the behavior of the double-layer does not change with position, the only boundary condition of interest for this system is the injection of current normal to the electrode-electrolyte interface[32].

As mentioned above, the molybdenum electrodes are taken to be non-blocking to electrons but blocking to the barium and titanate ions present in the system. The only sources or sinks for charge in the system are the active electrodes and they can only produce or consume electrons.

4.3.2 Chemical and Electrical Assumptions

For the molten mixtures of TiO_2-BaO, studied in this work, several assumptions were made, namely: that all BaO fully dissociates; that any ionic current detected is a result of the smaller, more mobile ion, Ba^{2+}; and that all the oxygen is bound up in

---

[31] This does not mean that each electrode must have the same interfacial chemistry and electrical behavior as every other electrode. Rather, the requirement of uniformity refers to uniformity of chemistry and electrical behavior along each electrode individually. The interfaces for the active and passive electrodes are quite different.

[32] The active electrode-electrolyte interfaces on the crucible and center electrode have a non-zero normally-directed current. The passive electrode-electrolyte interfaces on the voltage sensing electrodes and the free surface of the liquid have a zero normally-directed current.

complexes with titanium[33]. It is also assumed that there are no initial concentration gradients of any species and that the melt is homogeneous prior to the application of the square wave. While the distribution of barium ions may diverge from homogeneity during the application of the square wave, because the applied potential is below the decomposition voltage for all the species present, there is no net production or destruction of ions.

In this model, it is assumed that electrons in the melt do not exist as free electrons, but rather are resident on the titanium complexes and move by hopping from one titanate complex to another. Due to the size of the titanate complexes, they are modelled as effectively stationary, having a very low mobility relative to barium ions.

Electrical convection currents and mechanical convection are also assumed to be negligible. There is no significant electrical convection because no net free-charge is expected to exist in this melt (see discussion below). Relative to ion and charge mobility, any material convection[34] is expected to be slow. Within this context, a convection-free system is a reasonable assumption.

The absence of net free-charge is also assumed. The time constant for net free-charge in the system is calculated from the ratio of ε (the dielectric constant in F/m) to

---

[33] Assuming the complexing of the Ti^{+4} ion is sound given the large effective charge of the titanium ion. Complexing of metal ions is often observed for metals with high oxidation states. Given the mole ratio of these mixtures, there is not enough oxygen to form a TiO_4^{-x} ion from each titanium.

[34] The source of any material convection is expected to be thermal gradients in the melt. Once thermal equilibrium is established the convection should stop. Also, convection is not expected to be dramatic as the temperature of these experiments is not far from the melting point and the viscosity of the melts is moderate. These melts were allowed to equilibrate before measurement at each temperature to facilitate thermal equilibrium.

σ (the total conductivity). Using a conductivity of 4 S/cm and an ε of $100\varepsilon_0$ [35] [46] for the titanate melts, the time constant for dielectric relaxation (the lifetime of any net free-charge in this medium) is on the order of 5×10^{-12} seconds. Since the time scale for this experiment is minutes, any net free-charge in this system has decayed away before the first measurements are taken.

The absence of net free-charge simplifies the governing field equations. When the net free-charge density and its time rate of change can be approximated as zero, Maxwell's equations for the electric displacement density and current density can be represented as:

$$\nabla \bullet \mathbf{D} = \rho_{free} \approx 0 \tag{4.1}$$

$$\nabla \bullet \mathbf{J} = -\delta\rho/\delta t \approx 0 \tag{4.2}$$

$\mathbf{J}$ is the current density vector in A/m^2

ρ is the free-charge density in C/m^3

$\delta\rho/\delta t$ is the rate of change of free-charge in C/m^3s

$\mathbf{D}$ is the electric displacement vector in C/m^2

The propagation of electromagnetic waves[36] in this system can be neglected (the electro-quasistatics or EQS field model). The EQS approximation gives the following equations [25]:

---

[35] An estimate of ε of $100\varepsilon_0$ is a conservative estimate and assumes that the dielectric constant of the liquid is approximately equal to that of the solid. In fact, the dielectric constant of the liquid is expected to be much less than that of the solid and thus the dielectric relaxation time is even shorter.

[36] Using the speed of light as an order of magnitude estimation of the speed of electromagnetic wave propagation in this system and recognizing that the length scale of this cell is on the order of centimeters, the approximation that all electromagnetic wave transit time delays are immeasurably short is excellent.

$$\nabla \times \mathbf{E} = -\partial \mathbf{B}/\partial t \approx 0 \qquad (4.3)$$

$$\mathbf{E} = -\nabla\Phi \qquad (4.4)$$

$\mathbf{E}$ is the electric field vector in V/m

$\mathbf{B}$ is the magnetic flux density in $\mathrm{Wb/m^2}$

$\partial\mathbf{B}/\partial t$ is the rate of change of the magnetic flux density in $\mathrm{Wb/m^2s}$

Φ is the potential in V

From the material's constitutive relationship, $\mathbf{D}=\varepsilon\mathbf{E}$, and the relationships in equations (4.1) and (4.4), the Laplace equation for characterizing the electrical behavior of this system can be derived:

$$\nabla^2 \Phi = 0 \qquad (4.5)$$

No net free-charge in the melt implies that this problem can be treated as an imposed field problem. That is, since there are no sources of field in the melt, the electric field is defined solely by the boundary condition. When the electric field follows the imposed field model, the field can affect the behavior of the melt; because there are no sources of field in the melt, the melt does not contribute to the behavior of the field[37]. The establishment of the imposed field model for this system provides for the separation of the governing electrical differential equation (Laplace's equation) from the differential equation governing the barium flux.

Another implication of the extremely fast time constant for the dissipation of net free-charge in this system is quasineutrality in the melt. Based on quasineutrality, any microscopic region[38] examined displays local neutrality, so that an attempt to perturb the

---

[37] As stated earlier, the conductivity of the melt is a boundary condition which sets the geometric shape of the field.

[38] The electric field model used in this work assumes a continuum material model. As a result, the assertions made are expected to be valid on a micron scale, but not the atomistic scale (angstroms and nanometers).

local net charge density resulting from the movement of ions is immediately, electrically neutralized. The assumption of quasineutrality means it is possible to pile up ions, but not accumulate net charge.

This system is governed by the differential equation given by Laplace (equation (4.5)), for the electrical potential and field, and by the equation of continuity applied to barium. The barium number density and flux density expressions are derived next.

4.3.3 Derivation

This section presents a proof that in the long-time limit, only the electronic current is detected in the external circuit. For the $t \to \infty$ limit, a spatial (number) distribution is presented for barium which produces zero net ionic current. In the long-time limit, the ionic drift current is balanced by the diffusion current. It will be further demonstrated by examining all of the significant currents present in the system that the initial current density is a function of total conductivity (electronic and ionic). The ratio of the long-time current to initial current value yields the electronic transference number from which the ionic transference number can be obtained[39].

4.3.3.1 Coordinate Definition and Description

Polar coordinates (r,ϕ,z) are used where needed to reflect the radial symmetry displayed by the crucible and center electrode where r and ϕ define the x-y plane and the z direction is represented by z. The initial solution will be fully general without specifics of electrode geometry or coordinate representation. For mathematical simplicity, the general solution will be evaluated for infinitely long center and crucible electrodes,

---

[39] Once the electronic transference number is calculated, the ionic transference number can be found from the identity $t_{electronic} + t_{ionic} = 1$.

making it possible to examine the current as a function of r and ϕ only, ignoring variations in the z direction.

In this model, the crucible has a radius of "b" and the center electrode has radius of "a." For the electric field and potential, the ground reference is taken to be near the crucible electrode in the melt, just beyond the double-layer. V is the voltage near the inner electrode, just beyond the double-layer. (See Figure 4.01)

4.3.3.2 Governing Expression

The first step is the examination and definition of all significant sources of current in this system. The total current is the sum of the electronic ohmic current ($\sigma_e E$), ionic ohmic current ($\sigma_{Ba} E$), and ionic diffusion current ($z_{Ba} e D_{Ba} \nabla N_{Ba}$). The total current[40] is expressed as:

$$J = \sigma_e E + \sigma_{Ba} E - z_{Ba} e D_{Ba} \nabla N_{Ba} \qquad (4.6)$$

σ_e is the electronic conductivity in S/cm

σ_{Ba} is the ionic conductivity of the barium ion in S/cm

z_{Ba} is the charge on a barium ion

e is the electron charge in C

D_{Ba} is the diffusion constant for the barium ion in cm^2/s

N_{Ba} is the number density of barium ions in $particles/cm^3$

---

[40] There is no diffusion term for the electrons as there is no concentration gradient in free electrons. Rather, the electrons are resident on the titanate molecules which are extremely large and thus immobile. For clarity, the negligible ohmic and diffusional drift currents of the titanate molecules are left out of equation (4.6).

4.3.3.3 Initial ($t=0^+$) Regime

Consider now the $t=0^+$ case. The number density of barium ions is uniform and can be expressed by the constant

$$N_{Ba}(r,t) = N_o \text{ at } t=0^+ \tag{4.7}$$

The gradient in the concentration is zero ($\nabla N_{Ba} = 0$) and the expression for total current density (equation (4.6)) at $t=0^+$is simply:

$$\mathbf{J} = \sigma_e \mathbf{E} + \sigma_{Ba} \mathbf{E} \tag{4.8}$$

$$\mathbf{J} = (\sigma_e + \sigma_{Ba})\, \mathbf{E} \tag{4.9}$$

The current can be found from the double integral of the current density with the differential vector area over either current injecting electrode:

$$i = \iint \mathbf{J} \bullet \mathbf{dA} \tag{4.10}$$

$$i = (\sigma_e + \sigma_{Ba}) \iint \mathbf{E} \bullet \mathbf{dA} \tag{4.11}$$

i is the current in A

dA is the differential vector area in m^2

According to this model, at $t=0^+$, the initial peak in the current response to an applied square wave is a result of the total conductivity.

4.3.3.4 Long-time (t→∞) regime

4.3.3.4.1 General Expression

The t→∞ regime is now examined. A proof by construction is offered that there exists a number density distribution in N_{Ba} such that the diffusion current of barium ions balances the drift current of barium ions ($\mathbf{J}_{drift} = -\mathbf{J}_{diffusion}$.) The drift current density in barium is given as:

$$\mathbf{J}_{drift} = \sigma_{Ba}\mathbf{E} \tag{4.12}$$

The conductivity of barium can be written as:

$$\sigma_{Ba} = \mu_{Ba} z_{Ba} e N_{Ba} \tag{4.13}$$

μ_{Ba} is the mobility of the barium ion in $cm^2/(V\ s)$

The expression for the current density resulting from diffusion of the barium ions is derived from Fick's first law [47]:

$$\mathbf{J}_{diffusion} = -z_{Ba} e D_{Ba} \nabla N_{Ba} \tag{4.14}$$

When $\mathbf{J}_{drift}$ and $\mathbf{J}_{diffusion}$ are summed and the Einstein relationship ($D_{Ba} = \mu_{Ba}(kT/e)$) is employed, the following, governing partial differential equation results:

$$N_{Ba}\mathbf{E} - (kT/e)\nabla N_{Ba} = 0 \tag{4.15}$$

k is the Boltzman's constant in eV/K

T is the temperature in K

Equation (4.15) is the long-time ($t \rightarrow \infty$) limit in any coordinate system with any electrode geometry. It is the general expression for the long-time limit when the ionic diffusion current and the ionic drift current balance.

With the general identity given in equation (4.4) and some simple rearranging of terms, equation (4.15) can be re-expressed as:

$$\nabla N_{Ba}/N_{Ba} = \mathbf{E}/(kT/e) = -\nabla\Phi/(kT/e) \qquad (4.16)$$

A completely general expression for the number distribution can be found by doing the line integral[41] of equation (4.16) from $r=r_o$ to r.

$$\int_{r=ro}^{r} \nabla N_{Ba}/N_{Ba} \bullet \mathbf{dl} = (-e/kT) \int_{r=ro}^{r} \nabla\Phi \bullet \mathbf{dl} \qquad (4.17)$$

Integrating and exponentiating the solution to equation (4.17) give the expression for the number density of N_{Ba} in the long term limit as a function of a constant $N_{Ba}(r_o)$ and the potential, Φ:

$$N_{Ba}(r) = N_{Ba}(r_o)e^{-(\Phi(r)/Vth)} \qquad (4.18)$$

where $V_{th} = kT/e$

The value of the constant $N_{Ba}(r_o)$ is evaluated by applying the law for conservation of barium ions and equating the volume integral of the number distribution of barium at $t=0^+$ (equation (4.7)) and $t \rightarrow \infty$ (equation (4.18)).

---

[41] The integral is simplified if the boundaries are set such that $\Phi(r_o) = 0$.

4.3.3.4.2 Infinite Crucible and Center Electrode Geometry

For the simple geometry of infinitely long center and crucible electrodes, the potential[42] can be written as:

$$\Phi = V\{\ln(r/b)/\ln(a/b)\} \qquad (4.19)$$

V is the applied voltage in V

r is the radius in cm

Although equation (4.19) can be directly substituted into equation (4.18), a direct derivation is instructive because it demonstrates the internal logic of the general solution in a simplified and specified geometry. To find the explicit expression for the number density in this geometry, the first step is to express the potential specifically. Taking the negative gradient of the potential (equations (4.4) and (4.19)) yields the following expression for the electric field:

$$\mathbf{E} = \mathbf{r}(1/r)\{V/\ln(b/a)\} \qquad (4.20)$$

r is the unit vector in the r direction

Since the electric field's shape is dependent only on **r** (equation (4.20)), the partial with respect to r is the only term of interest in the ∇ operator. Equation (4.15) then reduces to the scaler differential equation:

$$N_{Ba}/r\ \{V/\ln(b/a)\} - V_{th}(\partial N_{Ba}/\partial r) = 0 \qquad (4.21)$$

---

[42] An additional term representing the constant voltage drop at the double-layer could be included. Since this term is a constant (it disappears when the gradient of the potential is taken), it is omitted from equation (4.19) to simplify the calculation.

Rearranging and expressing the partial differential equation as an ordinary differential equation[43]:

$$dN_{Ba}/dr - w(N_{Ba}/r) = 0 \qquad (4.22)$$

where $w = (V/V_{th})/\ln(b/a)$

Separation of the variables and integration of the equation (4.22) gives

$$\int_{N=N(a)}^{N(r)} 1/N_{Ba}\, dN_{Ba} = \int_{r=a}^{r} w(1/r)dr \qquad (4.23)$$

which yields

$$\ln \{N_{Ba}(r)/N_{Ba}(a)\} = w \ln (r/a) \qquad (4.24)$$

Exponentiating and rearranging terms gives the t→∞ number distribution of N_{Ba}[44] as

$$N_{Ba}(r) = N_{Ba}(a)(r/a)^{w} \qquad (4.25)$$

Conservation of barium holds as the electrodes are blocking to barium and there is no production or destruction of barium in the melt. Therefore, the equivalence of the volume integral of the barium distribution at time $t=0^{+}$ (equation (4.7)) and $t\rightarrow\infty$ (equation (4.25)) is used to find the constant, $N_{Ba}(a)$:

$$\int N_{Ba}(t=0^{+})dV = \int N_{Ba}(t=\infty)dV \qquad (4.26)$$

---

[43] A partial differential equation (p.d.e.) can be expressed as an ordinary differential equation (o.d.e.) when it depends on a single variable.

[44] Note that the direct substitution of equation (4.19) into equation (4.18) yields the equivalent solution: $N_{Ba}(r) = N_{Ba}(b)(r/b)^{w}$. Solving for the constant $N_{Ba}(b)$ by equating the volume integrals of the number distribution at $t=0^{+}$ and $t\rightarrow\infty$ produces equation (4.29).

$$ {}_{z=0}\int^{\ell} {}_{r=a}\int^{b} {}_{\phi=0}\int^{2\pi} N_o \, d\phi \, dr \, dz = {}_{z=0}\int^{\ell} {}_{r=a}\int^{b} {}_{\phi=0}\int^{2\pi} N_{Ba}(a)(r/a)^w \, d\phi \, dr \, dz \qquad (4.27) $$

From the integration of equation (4.27) the constant, $N_{Ba}(a)$, is found:

$$ N_{Ba}(a) = N_o\{(w+2)/2\}\{(b^2-a^2)/(b^{w+2}-a^{w+2)}\}a^w \qquad (4.28) $$

where $w = (V/V_{th})/(\ln(b/a)$

It has been shown that there exists a number distribution (in space) in barium, such that, as t→∞ the diffusion current of barium ions is balanced by the drift of barium ions at every point. For the infinite center and crucible electrode model, that number distribution is:

$$ N_{Ba}(r,\infty) = N_o\{(w+2)/2\}\{(b^2-a^2)/(b^{w+2}-a^{w+2)}\}r^w \qquad (4.29) $$

4.3.3.5 Summary

By using the expression for $N_{Ba}(r,\infty)$ (equation (4.29)) in equation (4.6) along with the other identities, it has been shown that in the case of t→∞ all the current measured is simply the ohmic electronic current ($\sigma_e E$.) Further support for this model will be given in Chapter 6 where it will be demonstrated that calculation of the ionic activation energy in this system based on the ionic transference numbers is consistent with values reported in the literature. Possible future refinements and expansions of this model will be discussed in Chapter 7.

4.4 Alternate Models

In this section, various alternate models for the source of the current decay behavior in a mixed conductor are presented and evaluated. The examination of the physical parameters of each possible source will show that none of these models correctly predicts the observed behavior.

4.4.1 Double-layer Charging

As the decay curve in the current response curve measured for TiO_2-BaO appears to have an exponential shape, double-layer charging at the electrode-electrolyte interface might be considered as the source of the decay behavior. The capacitance of a typical double-layer is approximately 500 μF [45] [48] and the resistance of this system is on the order of 0.05 Ω[46], therefore, a time constant, τ=RC, of 25 micro-seconds is expected. After several time constants have passed, the double-layer should be completely charged. Since the observed current decay takes tens of seconds, it follows that double-layer charging is not the source of the decay. Figure 4.02 is a typical current response curve.

4.4.2 Interfacial Oxide Layer

It could be argued that the source of the current decay is the presence of a solid interfacial layer on the electrodes that functions as a capacitor and produces "RC" behavior. Since all the electrodes are molybdenum and the melt contains oxides, a layer of molybdenum oxide is the most likely candidate for an interfacial barrier. Because almost all oxides are soluble in the TiO_2-BaO melt, a coating of molybdenum oxide is unlikely. Furthermore, molybdenum oxide compounds are extremely volatile at temperatures above about 600 °C [49].

---

[45] The range of 1500-2000 μF/cm^2 was measured by Esin *et al.* for molten oxides. For the crucible electrode with area of 46 cm^2, the capacitance is 7-9 x 10^{-2} F. The capacitance of the inner electrode which has an area of 0.32 cm^2 is 480-640 μF. Combining these series capacitors results in a total double layer capacitance of about 500 μF.

[46] The bulk resistance is on the order of 0.5 Ω. To find the resistance that shunts the double layer capacitor, the bulk resistance must be taken in parallel with the interfacial resistance. A conservative estimate of the interfacial resistance is that it is 10% of the bulk resistance, or 0.05 Ω. The effective resistance of the interface in parallel with the bulk is 0.05 Ω.

4.4.3 Electrolysis

The destruction or creation of barium, titanium, or oxygen might provide a depletion zone near the electrodes which would give rise to an exponentially-decaying current through the melt. However, the decomposition voltage at 1400°C for BaO is 2.9 V and for TiO_2, 1.6 V [37] -- well above the largest excitation, 0.1 V, used in these measurements. Additionally, if the source of the observed current decay was related to electrolysis, a current in the melt after the applied voltage was removed would not be expected. In all instances where a mixed conductor was studied, a current was detected when the applied voltage was removed. See Figure 4.02.

4.4.4 Instrumentation Artifact

Another possibility to consider is that the decay behavior observed in the TiO_2-BaO melts is an instrumentation artifact. This explanation is unlikely since this decay behavior was not observed when a square wave excitation was applied to the molten chloride (purely ionic) system. The molten chloride system response was a nearly zero current at all times. The behavior of the chloride system is consistent with the model presented above based on ohmic currents in ionic systems.

The disappearance of the current decay when the temperature was lowered provided further evidence that the decay behavior was not an instrumental artifact. For the 73 mol% TiO_2 melt, the decay behavior was nearly non-existent when it was cooled to a temperature of 1210°C, a temperature at which the mixture is completely solid. Figure 4.03 shows the current response of TiO_2-BaO at 1210°C. The current decay returned when this same mixture was restored to liquid temperatures. The model for the decay based on diffusion and ohmic currents would suggest that there was no significant ionic current at 1210°C, in the solid.

4.4.5 Schottky Barrier

It could be argued that the electrode-melt interface in this system forms a Schottky barrier which produces the observed current decay. A Schottky barrier, found at metal-semiconductor interfaces, produces a rectifying contact and displays RC behavior [50]. Though the applied voltage for these experiments was 0.08-0.1 V, a range in which the influence of rectification would be pronounced, there was no evidence of such an interface. Current flowed in response to the application of a square wave of both positive and negative magnitude. Also, the polarity of the electrodes was reversed from time to time. In no instance was the presence of a rectifying contact in the system detected.

4.4.6 Nonspecific Resistance and Capacitance

Another possible source of the observed current response is from a "non-specific" RC source. If the resistance of the system is used (≈0.5 Ω) with a time constant[47], τ, of about 10 seconds, a capacitance of 50 farads is expected. This capacitance is known to be too large for any reasonably sized, physical capacitor.

Attempting this calculation with the same time constant of 10 seconds and a more physically "reasonable" value of the capacitance of 50 μF, a corresponding resistance of 200,000 Ω is predicted. The 1286 measured currents close to 2 A. To draw 2 A through 200,000 Ω, the 1286 would have to produce a voltage of 400,000 V. The 1286 is rated for a maximum output of 12.8 V and cannot possibly source 400,000 V.

---

[47] The time constant, τ, is time for the current to decay 37% (e^{-1}).

4.5 Comparison of the Triangle and Square Wave Excitation Signal

4.5.1 Similarities

The system definition and boundary conditions are the same for the triangle excitation experiment for the measurement of total conductivity and for the square wave experiment for the measurement of transference numbers. Both experiments are imposed field problems in which there are no sources or sinks of net free-charge in the bulk. As such, Laplace's equation governs the electric field behavior. The magnitude of the triangle and square wave are small enough to remain below the decomposition voltage for all the species present.

4.5.2 Differences

There are several differences between the conditions of the experiments to measure total conductivity (triangular excitation signal) and the experiments to measure the transference numbers (square wave excitation signal). Because the time scale of the applied square wave signal is hundreds of seconds, it is possible for concentration gradients in barium to develop. In contrast, the triangle reverses polarity every 0.06 seconds -- too fast for the development of concentration gradients in the bulk.

The total current for the triangle wave is simply the sum of the ionic and electronic ohmic currents. For the square wave, the total current expression contains this sum plus an additional term representing the barium diffusion currents.

While both experiments are governed by Laplace's equation for the electric potential, the square wave is also governed by the equation of continuity for barium[48].

---

[48] Technically, the triangle wave experiment is also governed by a barium flux equation but the change in concentration is effectively zero due to the speed of this experiment, justifying omitting this equation when describing the governing equations for the measurement of total

Because the governing equation is an enhanced[49] diffusion equation, the space and time modes in the barium number density expression are coupled. When this occurs, the space and time modes are also coupled in the flux and current expressions as opposed to the measurement of total conductivity using the triangle wave, which is governed only by the Laplace equation and does not force the coupling of space and time.

---

conductivity.

[49] The diffusion equation is complicated by the addition of a term resulting from imposed electric field induced drift.

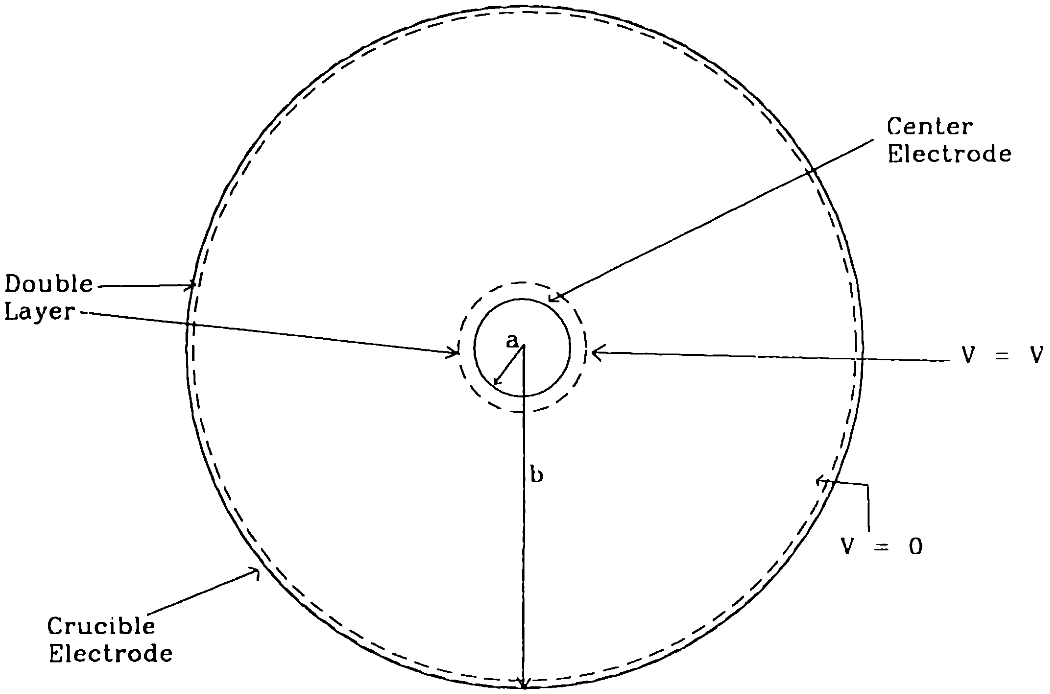

Figure 4.01: System and Boundary Definition for the Square Wave-Decay Derivation

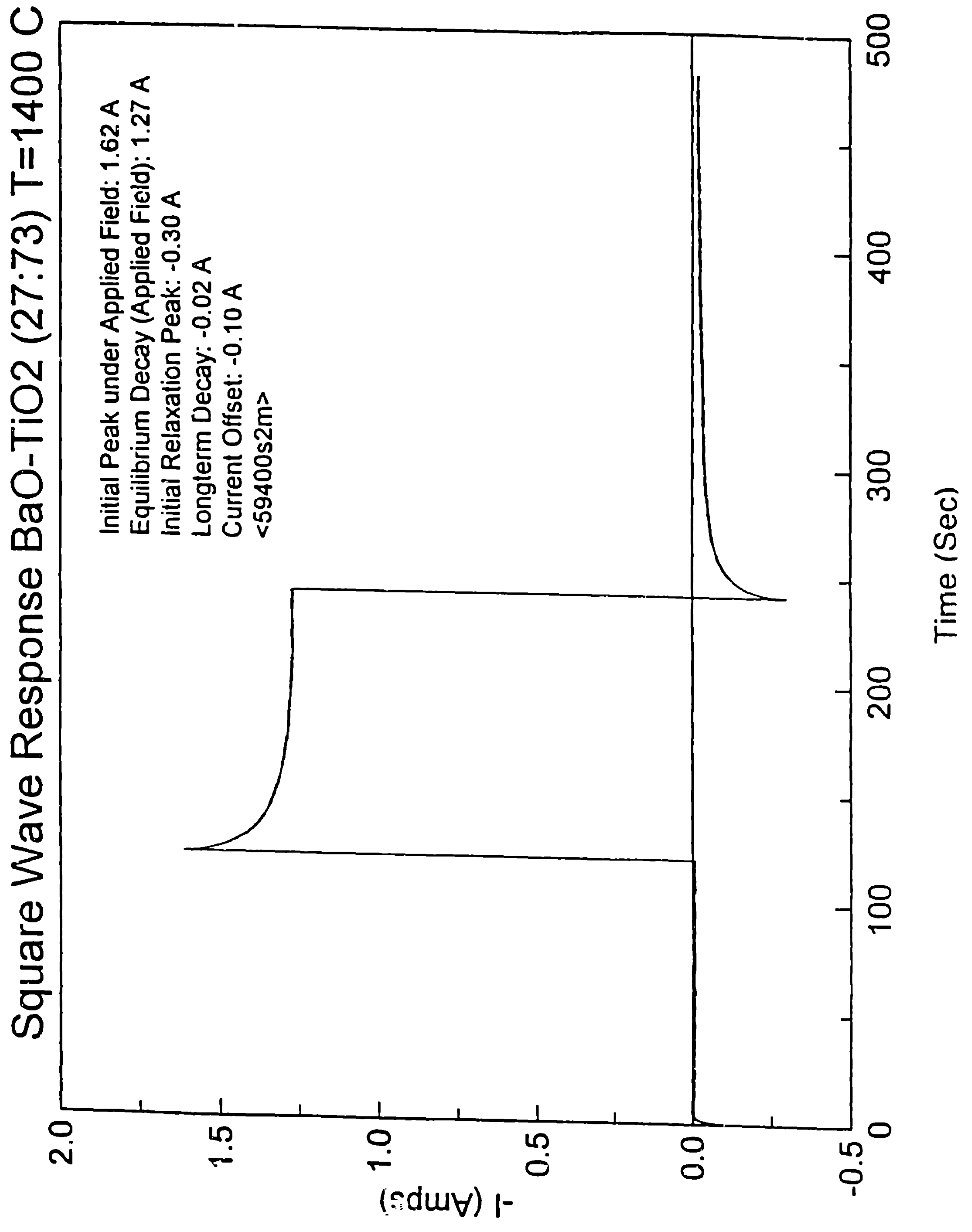

Figure 4.02: A Typical Current Response to the Application and Removal of a Square Wave Voltage Excitation

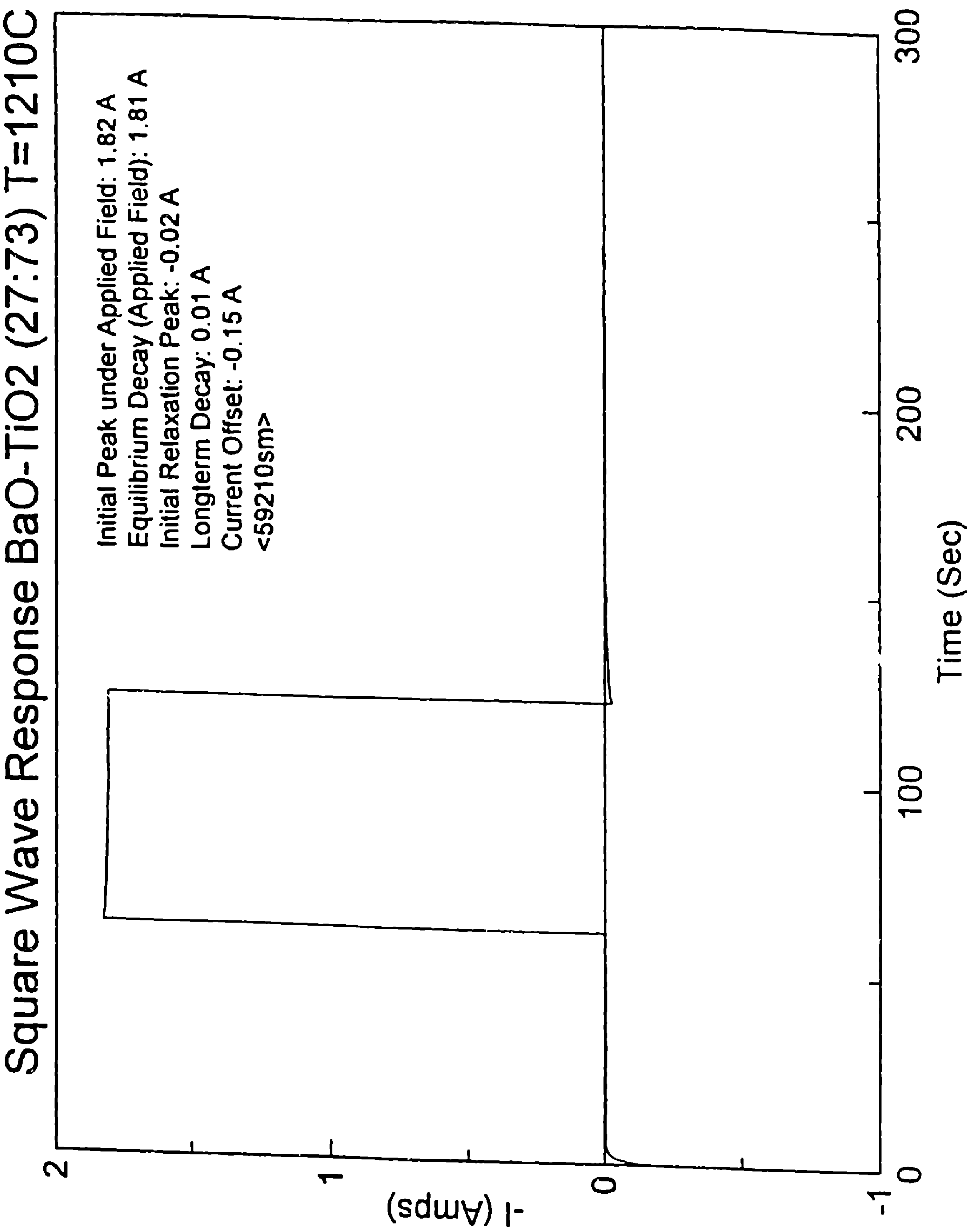

Figure 4.03: Current Response to the Application and Removal of a Square Wave Voltage Excitation in Solid TiO_2-BaO

Chapter 5: Experimental Procedure

The apparatus and experimental protocol for the cell calibration with molten chlorides and the electrical conductivity measurements and transference measurements of molten TiO_2-BaO are described in this chapter.

5.1 Preliminary Measurements and Calibration

5.1.1 Determination of Approximate Electrical Conductivity

Appropriate calibration is the first step in the deployment of the high-accuracy four-point crucible cell. An estimate of the electrical conductivity of the test medium is needed for proper selection of calibration standards. Ideally, the calibration standard's conductivity matches that of the test medium. As stated earlier, the accuracy of the measured conductivity is directly related to the relative magnitudes of the calibration and test solutions' conductivities.

In this investigation, approximate measurements of the electrical conductivity were made using the new, moveable CCE. Using this technique, the electrical conductivity of a melt of TiO_2-BaO (67 mol% TiO_2) was found to be approximately 2 S/cm over the temperature range 1300-1400°C[50]. See Figures 2.02. The details of the cell design and experimental procedure for the CCE measurement are found in Appendix A.

---

[50] The high accuracy crucible cell technique was subsequently used and yielded conductivity measurements of approximately 4 S/cm, over the same temperature range, indicating that the coaxial cell technique had under-reported the conductivity by a factor of 2.

5.1.2 Melt Density Determination and Melt Height Selection

The high-accuracy four-point crucible-cell technique requires the current path of the calibration solution to be reproduced in the test medium. In order to achieve this goal, identical electrode size and position are required and the test samples must have the same volume.

Since the density of molten TiO_2-BaO at 1300-1500°C was not available in the literature, a rough measurement was conducted to determine the approximate melt density. A melt of TiO_2-BaO (67 mol% TiO_2) of known weight was prepared and a molybdenum rod and a thermocouple were immersed in the melt. The molybdenum rod was placed in contact with the floor of a molybdenum crucible to assure adequate contact with the melt. A second molybdenum rod of known length was lowered into the melt and both rods were attached to a digital multimeter[51]. The resistance between the two rods was constantly monitored as the moveable rod was slowly lowered. The top surface of the melt was detected when a dramatic drop in the resistance between the rods was recorded. The location of the melt surface was confirmed by repeatedly lowering the rod after the melt was allowed to drain from the end. Measurements of the melt height were taken over the temperature range 1380-1440°C and an average melt height was calculated. An average density of 4.74 ± 0.12 g/cm^3 was calculated for the melt at an average temperature of 1400°C. Based on the volume available in the crucible used, a melt height of 39 mm was selected for both the chloride calibration and titanate measurements.

5.1.3 Calibration with Standard Solutions

To establish the cell factor as a function of conductivity for the four-point crucible cell, it is necessary to calibrate with a standard solution of conductivity close to that of

---

[51] Keithley model 197, Cleveland, OH

the test medium, or use a series of calibration solutions whose conductivities span that of the system under investigation.

5.1.3.1 Selection of Conductivity Standards

For this work, a well-studied calibration standard whose conductivity and density are known was selected. The literature was surveyed to find a liquid that met the following criteria: (1) conductivity of 2-4 S/cm, (2) well-documented densities, (3) non-toxic, (4) non-corrosive, (5) easy to handle, and (6) readily available.

A mixture of 15.23:84.77 mol% KCl:NaCl (electrical conductivity is 2.99-3.56 S/cm from 758-927°C) which satisfied the above criteria was selected as the calibration standard. The dependence of conductivity on temperature was reported in the literature [51]. Because each temperature represents a melt with a different conductivity, one solution composition can be used to generate the relationship between conductivity and the conductivity-dependent cell factor for a range of conductivities.

5.1.3.2 Equipment

5.1.3.2.1 Non-electrical Equipment

a. The Conductance Cell

The components of the four-point cell were the crucible electrode, the center electrode, and two voltage sensing electrodes placed between them to measure the melt voltage. The crucible electrode was fabricated from an 8" right cylindrical molybdenum crucible[52] with an i.d. of 1.5" and a wall thickness of 0.06" in which two sets of small holes were machined 0.5" from the top. An 18" long, 0.125" molybdenum rod which had

---

[52] Phillips Elmet, Lewiston, ME.

been notched with the same spacing as the crucible holes was attached to the inner wall of the crucible with 0.02" molybdenum wire. The wire was twice threaded through each pair of holes and around the groove twice and then tied off. See Figure 5.01 for an illustration of how this connection was made. A 0.125" diameter solid 18" molybdenum rod was used as the center electrode. Two 0.0625" molybdenum rods, 18" long, were used for the voltage-sensing electrodes. A 0.125" molybdenum-sheathed type-R thermocouple[53] measured the temperature in the melt. An Omega DP-41 temperature indicator[54] with a built-in electronic ice-point converted the voltage reading into temperature.

A fixture of boron-nitride was used to hold the electrodes and thermocouple in place within the reactor tube. The spacer, a disk 1.6" in diameter, 0.25" thick, was machined from hot press boron nitride. The spacer was baked slowly under argon to drive off the binder and prevent shattering during use. It was mounted on a 0.125" diameter 10" long molybdenum rod and secured in place with bushings which were immobilized by 0.02" molybdenum wire wrapped and tied around grooves in the rod. The spacer rested on the top of the crucible and functioned to keep all the electrodes properly aligned. Figure 5.02 illustrates the components of the conductance cell.

To maintain electrical isolation and prevent current loss, all electrodes were electrically isolated from the metal cap through the application of one layer of FEP[55] shrink tubing. Additionally, the thermocouple and spacer holder rod were electrically insulated using shrink tubing. The shrink tubing had to adhere tightly to the rods to maintain the integrity of the atmosphere inside the reactor tube. See Appendix B for more details about and application notes on the shrink tubing.

---

[53] ASTM platinum-13% rhodium, Omega Corporation, Stamford, CT.

[54] Omega Corporation, Stamford, CT.

[55] Tex-Loc, Ft. Worth, TX.

b. Cap and Reactor Tube

A 2.0" i.d. stainless steel Kwik Disconnect Cap[56] was fitted with a customized top plate. Welded to this top plate were several Cajon Ultra-Torr[57] compression fittings. These fittings used viton o-rings to secure the electrodes, thermocouple, and spacer holder. This type of compression fitting allowed positional variation of the thermocouple while maintaining the integrity of the atmosphere in the reactor tube. The relative electrode positions defined by the placement of these compression fitting are illustrated in Figure 5.03.

The Kwik Disconnect cap was further customized by welding stainless steel tubing to two holes machined on opposite sides. The tubing was connected by swagelock fittings to two Nupro vacuum valves[58]. One valve provided an inlet for argon, the other was connected to the vacuum manifold which allowed release of pressure to a vacuum pump or through a bubbler to house vacuum. Figure 5.04 is a schematic of the atmosphere control system.

The Kwik disconnect cap used a compression fitting with 226 viton o-ring and ferrule to attach to the 2.0" o.d. (1.75" i.d.) 15" long round-bottom 99.8% alumina reactor tube.[59] To prevent the crucible from tilting inside the round-bottom reactor tube a 0.25" thick, 1.6" diameter alumina disk was used as a platform at the bottom of the reactor tube. One inch wide ceramic tape[60] was wound around the reactor tube below the cap and tied down with chromel wire to produce a 1" thick heat plug.

---

[56] #410016, MDC Vacuum Product Corporation, Hayward, CA.

[57] Cambridge Valve and Fittings, Cambridge, MA.

[58] B-4HK with soft seat, Cambridge Valve and Fittings, Cambridge, MA.

[59] Vesuvius MacDanel, Beaver Falls, PA.

[60] Zircar, Florida, NY

c. Furnace

A vertical tube furnace with a 2.0" bore, built and designed in-house, provided the heat for these experiments. Six silicon carbide heating elements[61] were arranged in a delta configuration. A three phase, 208 Volt S.C.R. power controller[62] was used with a programmable p.i.d. temperature controller[63] connected to a type-R thermocouple to tune and control the furnace. When properly tuned, the furnace was capable of holding temperature within ± 0.5°C in the 1.5" hot zone. An alumina, closed one end, round-bottom furnace tube with an i.d. of 2" was the receptacle for the reactor tube. The metallic case of the furnace was grounded and two sheets of asbestos insulation were placed on top of the furnace to keep the top face cool. Additionally, a set of four blowers surrounded the reactor tube cap where it extended from the furnace. The blowers were effective at reducing the temperature of the cap so that the o-rings did not decompose.

d. Magnetic Shielding

Because of the sensitivity of the small signal electrical measurements to noise on the electrical line, it was necessary to use isolation power transformers and to ensure that the line power was uncorrupted by local network noise. Noise was further decreased with the placement of a metal stool on the top of the furnace. (Figure 5.05) The metal stool provided a conducting ring about 4" above the furnace at the height of the electrical connections to the cap which decreased the noise from stray magnetic fields. The legs and top plate formed additional conducting rings effective at shielding random magnetic fields. The furnace and, therefore, the stool were grounded through connection with the

---

[61] SE 18x9x0.5 I Squared R, Akron, NY.

[62] Omega Model SCR73, Stamford, CT.

[63] Omega CN2011, Stamford, CT.

ground wire of the power line. The seat of the stool acted as a shield against incoming electric fields.

5.1.3.2.2 Electrical Equipment

a. Electrochemical Interface

A Solartron 1286 Electrochemical Interface[64] was used to apply a voltage between the crucible electrode and the center rod electrode and to measure the current response. The instrument was controlled using CorrWare[65] installed on an IBM 486-DX personal computer in conjunction with a standard GPIB (IEEE-486) parallel interface bus.

b. Electrometers

Two electrometers[66] with high input impedance (5 x 10^{13} Ω shunted by 20 pF) were used to measure the melt voltage at the two sense electrodes for the melts with blocking electrodes. High input electrometers were necessary because of the high interfacial impedance presented by the double-layer capacitance.

Initially, voltage measuring devices with standard input impedances of 1 MΩ were used, but this input impedance was unable to prevent current from leaking out of the cell and corrupting the voltage measurement. Similarly, a single electrometer proved inadequate for measuring the voltage difference between the voltage-sensing electrodes because the high input impedance of the electrometer was available only on the "high" leg of its input terminal. When the electrometer's output was connected to the grounded

---

[64] Solartron, Houston, TX

[65] Version 1.3a, Scribner Associates, Charlottesville, VA.

[66] Keithley, Model 614, Cleveland, OH

outer shield of the oscilloscope, the "low" terminal on the electrometer input was no longer floating and became effectively a low input channel.

c. Oscilloscope

A four-channel digitizing oscilloscope[67] was used to record the applied voltage, melt current, and melt voltage, and to provide a universal time basis for all the measured quantities.

The voltage at each of the two voltage-sensing electrodes was measured by an electrometer and recorded on Channels 1 and 2 of the oscilloscope. From each electrometer, the analog output connection of the back panel was connected to an inner shield of the oscilloscope. The electrometer's back panel common output was tied to the oscilloscope's corresponding outer shields. Figure 5.06 illustrates all the electrical connections used for the calibration experiments. Because of the circuit design of the electrometers, the output was scaled according to the selected input range and was always inverted. The oscilloscope recorded the absolute voltage at each sense electrode rather than the voltage difference. The internal mathematical algorithm of the oscilloscope was not used to find the voltage difference because it was insufficiently accurate. Rather, this differencing of the two voltage measurements was accomplished with a simple math utility, Diff_dat, written expressly for this investigation.[68] All data collected by the oscilloscope was recorded in binary on a floppy diskette.

The back panel connections on the 1286 which supplied the cell current and applied voltages have a 50 Ω semi-floating connection, allowing direct instrument connection of both the inner conductors and the outer shields of the BNC cables to the oscilloscope. (See Figure 5.06)

---

[67] Tektronix 420A, Wilsonville, OR

[68] Dr. Kevin G. Rhoads, MIT, Cambridge, MA.

5.1.3.3 Melt Preparation and Atmosphere Control

The weight of each of the components of the KCl-NaCl mixture needed to achieve a height of 39 mm was calculated based on the median temperature and the mixture density reported by Van Artsdalen *et al.* [51].

The calculated quantities of high purity KCl and NaCl[69] which had been packed under argon, were weighed out and combined in an argon filled dry box. Table 5.1 gives the quantities used. The mixing container was vigorously shaken for 1-2 minutes and the contents carefully transferred to the crucible[70]. The crucible was gently tapped against the dry box floor to pack the powder and prevent spillage. The crucible was placed in the reactor tube and the cap in which the voltage-sensing electrodes, thermocouple, and spacer were mounted was attached to the reactor tube. The crucible lead was secured in its proper port and all the valves and ports were hand tightened. The cap was then secured to the reactor tube and it was removed from the dry box. The cap was further tightened to the reactor tube with a strap wrench. The ceramic tape ring was placed around the reactor tube before it was inserted into the furnace.

The atmosphere in the reactor tube was carefully evacuated to 50 µm of Hg or less using a roughing pump. To prevent scattering of the melt powder, the reactor tube was slowly exposed to the vacuum. A vacuum level no greater than 50 µm was necessary to sufficiently evacuate the atmosphere and prevent high temperature oxidation of the molybdenum. The reactor tube was then heated to 300°C at a rate of 150 degrees per hour and the salts dried under vacuum at 300°C for a minimum of 12 hours.

---

[69] 99.999%, Cerac, Milwaukee, WI.

[70] There was approximately 0.6 g of residual powder that was not transferred from the jar to the crucible.

Before further heating, the reactor tube was cleansed of residual oxygen using a series of pressurizing fills and releases with argon. The argon,[71] which was further dried using a Supelco OMI-2 filter,[72] was admitted into the evacuated tube slowly to prevent disturbance of the powder. Once a steady flow of argon through the reactor tube was established, the pressure in the reactor tube was allowed to rise to atmospheric pressure. At 1-2 psi above atmospheric pressure, the excess pressure in the reactor tube was released out of an oil-filled bubbler. A steady flow out the bubbler was maintained for two minutes. The valve to the bubbler was then closed and the reactor tube pressurized again. This fill-and-release procedure was repeated four times. After the fourth time, the argon was allowed to flow continuously out of the bubbler and the heating of the powder to the first working temperature at a rate of 180 degrees per hour began. (Figure 5.04 illustrates the atmosphere control system.) The initial working temperature was selected to be 75-100 degrees above the melting point of the solution.

5.1.3.4 Experimental Procedure: Calibration

Before beginning any electrical measurements, all instrumentation was thermally equilibrated. The 1286 Electrochemical Interface required two hours to be fully warmed up. Similarly, the oscilloscope and electrometers were turned on in advance of the measurement. After warming up for at least 20 minutes, the oscilloscope was calibrated using its internal signal path compensation program to correct for DC inaccuracies caused by ambient temperature variation or long term drift. After equilibrating for one hour, the electrometers were zeroed.

The integrity of the electrical isolation of the leads from the cap was confirmed using a hand-held ohm-meter before the measurement was started. To assure accurate

---

[71] Ultra-High Purity (UHP), Grade 5.0, Airco, Murray Hills, NJ.

[72] This filter reduces the oxygen content of the argon to 10 p.p.b. and the moisture content to 3 p.p.b. Supelco, Bellefonte, PA.

electrode positioning, the electrodes were positioned relative to the crucible floor. The center electrode was lowered to touch the floor of the crucible. The height of the exposed rod was measured and the center electrode was then retracted 0.25" from the crucible floor. The voltage-sensing electrodes were lowered to the crucible floor and then retracted 0.75". Similarly, the floor of the crucible was found by the thermocouple. The position 0.75" above the crucible floor was marked on the thermocouple so that the thermocouple could be returned to this position after retraction during the electrical measurement.

BNC cables with breakouts to mini-alligator clips were used to connect the 1286 electrochemical interface to the cell. The inner leads of the cables of the working electrode (WE) and reference electrode 2 (RE2) of the 1286 were tied together and attached to the crucible electrode. The counter electrode (CE) and reference electrode 1 (RE1) were tied together and attached to the center electrode.[73] Normal polarity with the working electrode positive and the counter electrode negative was used.[74]

The outer shields of all these terminals were driven by the 1286 and were left floating. Because the 1286 measures the current through a standard resistor between the working electrode and ground, attaching the working electrode to the crucible was the preferred configuration; it minimized stray currents by keeping the potential of the crucible close to ground. When the reverse configuration was tried, the voltage measured was much noisier.

---

[73] Though the "counter electrode" lead from the electrochemical interface is attached to the center electrode, this electrode is the electrochemical working electrode. Electrochemists often use the term "working electrode" to refer to the electrode with the smallest surface area and the highest current density.

[74] The 1286 is designed so that its "working electrode" is maintained at a potential close to ground while the potential on the counter electrode is varied. This ensures that when applying 0.1 V to the cell, the working electrode will be 0 and the counter electrode -0.1 V. Varying the potential at the counter electrode while maintaining a constant potential at the working electrode is referred to as "reverse polarity" and has been the source of great confusion for users of the Solartron 1286 Electrochemical Interface.

Figure 5.06 shows the electrical connections for the electrometer. The input connection of the electrometer required a triaxial cable connection with a "high," "low," and "ground." The "high" legs of each of the two electrometers were connected to one of the voltage measuring electrodes and the melt voltage was found from the difference between the two electrometer measurements.[75] The "low" sides of the electrometer's input terminal were tied together to give a common reference as were the "chassis" connectors of the triaxial cable.

The potential applied to the cell was swept through four set points: 0.0 V, -0.1 V, +0.1 V, and 0 V versus reference (between RE1 and RE2) using the cyclic voltammetry program in CorrWare. A "fast" ramp rate was desirable to increase the amount of current through the double-layer and thus increase the signal to noise ratio. (Equation (3.18)) Although the 1286 is rated to produce 10 V/s, in practice a rate much above 3 V/s was not possible. A slew rate of 3 V/s[76], was used for all measurements which consisted of a subset of the 5000 cycles requested. The data were acquired by the 1286 at a fixed rate of 15 points/second, the maximum possible for the 1286 controlled by CorrWare.

The 1286's back panel signals indicate the current measured and voltage applied[77]. The voltage signal is the actual voltage applied to the cell (up to 12.8 V.) The measured current is also reported as a voltage with the selected current range scaled to ± 200 mV. For the current signal to have any meaning, the current range must be

---

[75] Ideally, a differential electrometer with two high input-impedance terminals is used for this measurement. If a differential electrometer is not available, two, single high-input impedance electrometers can be used to measure the voltage at each of the voltage measuring electrodes and the difference found mathematically.

[76] This slew rate provided a period that was much longer than that needed to charge the double layer. As a result, the double layer was effectively always charged. Additionally, this period was shorter enough that bulk diffusional currents were not observed.

[77] The back panel signals are outputs of the pre-processed, analog circuits of the 1286. As such, these signals are not limited by the 1286's limits on digitization rate or number of digits.

fixed at all times during the experiment. The auto selection option for the current range was never used.

The full-scale current range was either 200 mA or 2 A. The 2 A range was preferred because it corresponds to the smallest standard resistor in the 1286 for measuring current, 0.1 Ω. The smallest standard resistor available in the 1286 provided the highest common mode rejection ratio for this cell, which had a total impedance on the order of 0.5 Ω. It was found that, for small currents, the 2 A current range provided low resolution. To increase the current resolution, it was occasionally necessary to use the 200 mA current range with a 1 Ω standard resistor. When necessary, a voltage amplifier[78] was used to magnify the current signal into the oscilloscope.

The remaining parameters for controlling the 1286 were set as follows: the low pass filter of the 1286 was not used because it decreases the measurement frequency; bandwidth C was used for the analog sweep; and the IR compensation option was not employed.

A metal stool was placed on top of the furnace to shield the electrodes from stray magnetic fields. After the temperature was measured by the thermocouple and recorded, it was raised out of the melt to assure that its metal sheath did not disrupt the electric fields between the working and counter electrodes.

Using the above parameters for the Electrochemical Interface, a triangular excitation was applied to the cell. A 15 second delay between the request for the signal and the actual production of the wave occurred because the 1286 required time to charge its internal capacitors. After the first 10-20 cycles, the oscilloscope was allowed to trigger and 10-15 cycles of data were collected and saved to floppy diskette. Data were collected by the oscilloscope at a rate of 500 samples/second for 2 seconds.

---

[78] Built by Don Galler, DMSE, MIT, Cambridge, MA.

After the data were collected, the thermocouple was lowered once again and the ending temperature recorded. Data in which the temperature varied more than 2 degrees (a 0.25% drift) were discarded. Once data had been collected at a specified temperature, the furnace controller was reprogrammed for a new set point, 25-50 degrees higher or lower. Because the temperature controller was in a continuous "soak" phase, changes in the programmed set point resulted in nearly instantaneous change in the furnace temperature. An additional twenty to thirty minutes were required for the melt to achieve thermal equilibrium. The measurement procedure was repeated at different temperatures during both heating and cooling cycles over the temperature range of interest for the calibration standard.

Once all the data were collected, the electrodes and thermocouple were raised out of the melt. The melt was allowed to drain from the rods before the furnace was turned off and the melt allowed to cool to room temperature under flowing argon.

5.2 Measurement of the Conductivity and Transference Numbers of Molten TiO_2-BaO

The equipment and experimental technique deployed to measure the electrical conductivity of molten TiO_2-BaO were essentially the same as the technique described above for the calibration. The exceptions will be discussed in these sections.

5.2.1 Equipment

5.2.1.1 General

The same experimental set up with crucible electrode, center electrode, and voltage measuring electrodes mounted in Cajon compression fittings in the cap of the reactor tube was employed. A new crucible and new rods of the same dimension were used for each oxide composition. Use of the same caps, spacers, and rod sizes ensured that the geometry of the calibration experiments was replicated in the molten titanates.

5.2.1.2 Electrical Equipment

Preliminary measurements with molten titanates indicated a low impedance interfacial path, typical of electronic or multivalent melt, so that the electrometers were not needed. The Tektronix 420A digitizing oscilloscope was used instead to measure differentially the melt voltage directly on channel 1. Channels 3 and 4 continued to record the total current and applied voltage as reported from the back panel of the 1286. Figure 5.07 illustrates the connections among the electrical equipment for the titanate experiments.

5.2.2 Melt Preparation

For each of the oxide melts, the weight of BaO and TiO_2 needed to produce the correct mole ratio and desired height was calculated using the experimentally measured melt density. The weights of the constituent powders used are given in Table 5.2.

Because BaO is sensitive to air, the titanate melt powders were prepared in a dry box. The proper quantities of BaO[79] and TiO_2[80] as well as a constant 1 weight percent of MoO_2[81] to fix the partial pressure of oxygen[82] in the melt were weighed, combined, and vigorously shaken. The contents were then carefully transferred[83] to a new crucible.

---

[79] 99.5%, <100 mesh, packed under argon, Cerac.

[80] 99.9%, <325 mesh, packed under argon, Cerac.

[81] 99%, Alfa, Ward Hill, MA.

[82] The conductivity of semiconductors is sensitive to the partial pressure of oxygen over certain ranges. To eliminate variability due to changes in the partial pressure of oxygen, a small quantity of MoO_2 was added to the melt to establish an equilibrium between the molybdenum oxide and molybdenum metal to fix the partial pressure of oxygen at every temperature.

[83] A residual of 0.6-0.7 g of powder was not transferred from the jar to the crucible.

The crucible was tapped and packed to prevent spillage after which it was placed in a reactor tube and the cap secured.

Because large volumes of powder were needed to produce the desired melt height and because of the thermal limitations of the shrink tubing, a preliminary melt of the powders was carried out. During this procedure, the ports of the cap were closed off with blanks since the electrodes were not needed.

The reactor tube was removed from the dry box and the cap further tightened using a strap wrench and the ceramic tape heat plug attached. Once in the furnace, the reactor tube was placed under vacuum and the atmosphere controlled as described in section 5.1.3.4. The powders were heated to 500°C at a rate of 250 degrees per hour. The powders were dried under vacuum at 500°C for a minimum of four hours. The reactor tube was then backfilled with ultra-high purity (UHP) argon and heated at a rate of 230 degrees per hour to 1450°C under flowing argon. The temperature was held for one hour at 1450°C and then allowed to cool to room temperature.

Once the powders had melted and cooled, the electrodes, thermocouple, and spacer holder were mounted in the cap. The reactor tube was heated under flowing argon to 1475°C at a rate of 300 degrees per hour after being pressurized with UHP argon three times.

5.2.3 Measurement Procedure

5.2.3.1 Conductivity Measurements: Triangle Wave Excitation

In the experimental protocol described above for the calibration a triangular excitation of 0.1 V at a rate of 3 V/s was used to measure the total conductivity. For some of the temperatures at which the electrical conductivity was measured, the electronic and ionic transference numbers were also found using a square wave rather than triangular excitation.

5.2.3.2 Transference Number Measurements: Square Wave Excitation

Using the CorrWare software to control the 1286 Electrochemical Interface, a stepped potential (square wave) was applied to the current injecting electrodes when the melt was at thermal equilibrium. Unlike the electrical conductivity measurement which lasted 2 seconds, the duration of the square wave experiment was several minutes and the establishment of thermal equilibrium in the melt in advance of the measurement was important.

The first step of the square wave was 0 V versus open circuit for 1-2 minutes, followed by 0.1 V[84] versus reference[85] for 2 minutes, and ending with 0 V versus open circuit for 2 minutes. The remaining parameters for the 1286 Electrochemical Interface are the same as those described above. During the stepped potential measurements, the oscilloscope monitored the melt voltage, the total current, and the applied voltage at a rate of 5 samples per second for a total of 500 seconds. To assure electronic homogeneity after polarization, at least one triangular excitation was always applied between successive square waves.

When the total conductivity and the transference numbers were measured, the temperature controller was reset 25 degrees higher for the heating cycles and 50 degrees lower for the cooling cycles. While the furnace controller quickly reached the new set point, it took 30-45 minutes for the melt to reach its new equilibrium temperature. Because the electrical conductivity measurements lasted only two seconds, it was possible

---

[84] For the barium titanate melt with a composition of 73 mol% TiO_2, it was necessary to limit the applied potential to ± 0.08 V. Higher voltages caused overloads in the 1286's ammeter.

[85] In the CorrWare program, "versus reference" means between RE1 and RE2.

to collect data during the transition from one set point to the next. On the other hand, since the transference measurements took several minutes, they were conducted only when a set point had been reached and the temperature in the melt was stable. Any measurement in which the temperature varied more than 3 degrees (a 0.2% drift) over the duration of the experiment was discarded. For each oxide composition, measurements were made over a 100-125 degree interval beginning about 25 degrees above the melting point.

Once all the data were collected, the electrodes and thermocouple were removed from the melt. The temperature in the furnace was increased to facilitate the melt draining from the rods. Finally, the furnace was turned off and the melt was cooled to room temperature under flowing argon. Unlike the chlorides, the molten titanates are not water soluble and no solution was found to remove the hardened melt from the rods. As a result, each oxide composition required a new crucible and set of electrodes.[86]

5.3 Measurements of the Conductivity Near the Melting Point

Electrical conductivity measurements (triangular excitation) and transference measurements (square wave excitation) were also taken in solid TiO_2-BaO (73 mol% TiO_2). This melt was allowed to freeze with the electrodes and thermocouple in position. The experiment was useful in determining the relative magnitude of the electrical conductivity for the liquid and solid. These results along with those for conductivity of a function of temperature and composition and the transference numbers are discussed in Chapter 6.

---

[86] The thermocouple was reused following cleaning by carefully grinding away the residual melt.

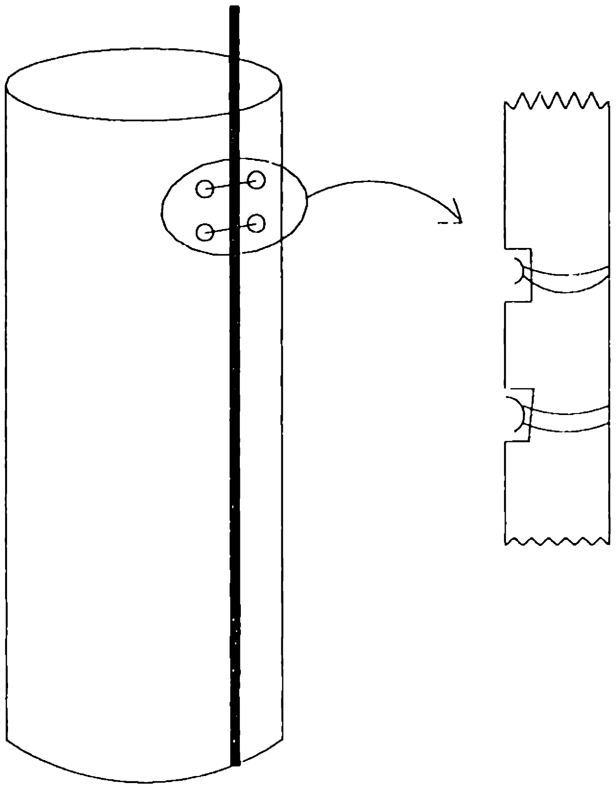

Figure 5.01: Attachment of Current-Carrying Lead to Crucible Electrode

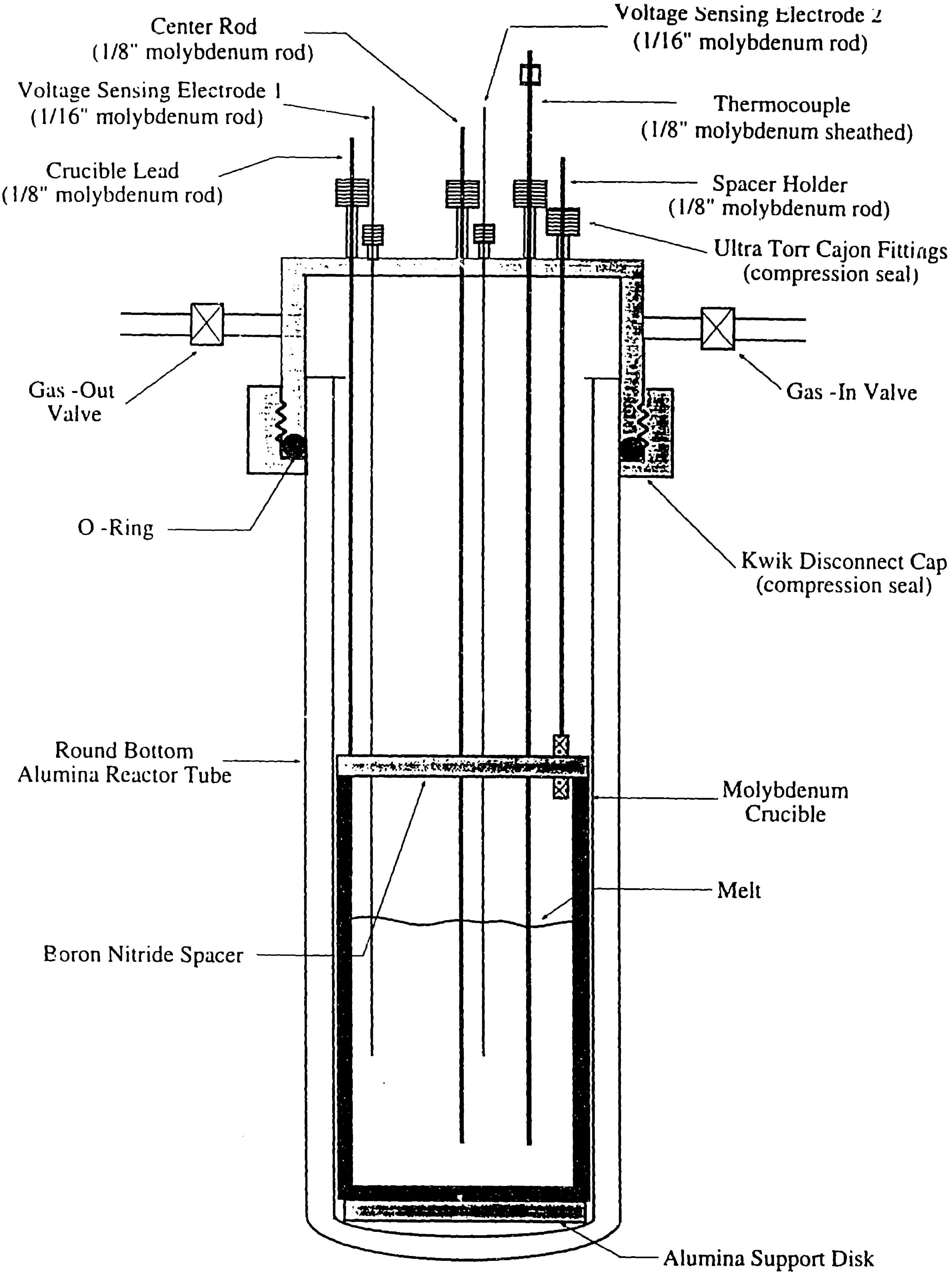

Figure 5.02: The Conductance Cell

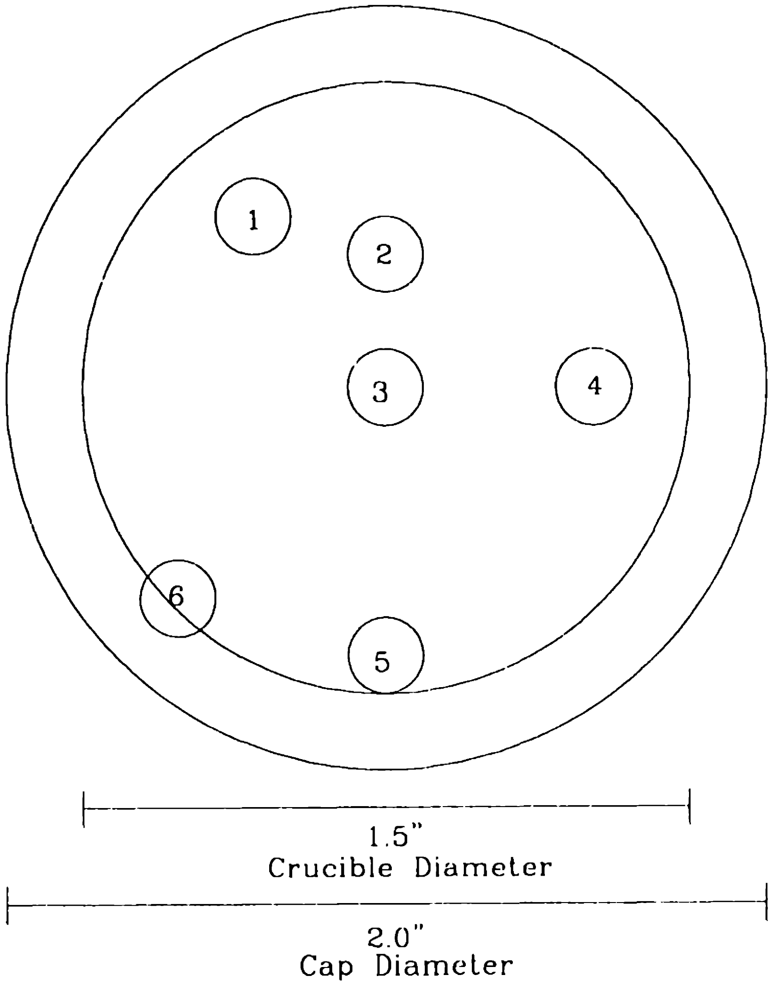

Port	Center to Center Distances:	Angles
#1 Spacer Support Rod	1-3: 0.60"	∡ 132 = 45°
#2 Inner Voltage-Sensing Electrode	2-3: 0.25"	∡ 234 = 90°
#3 Center Electrode 3 :	center	
#4 Thermocouple	4-3: 0.56"	∡ 435 = 90°
#5 Outer Voltage-Sensing Electrode	5-3: 0.625"	∡ 534 = 90°
#6 Crucible Electrode	6-3: 0.711"	∡ 635 = 45°

Figure 5.03: Relative Locations of the Ports on the Cap

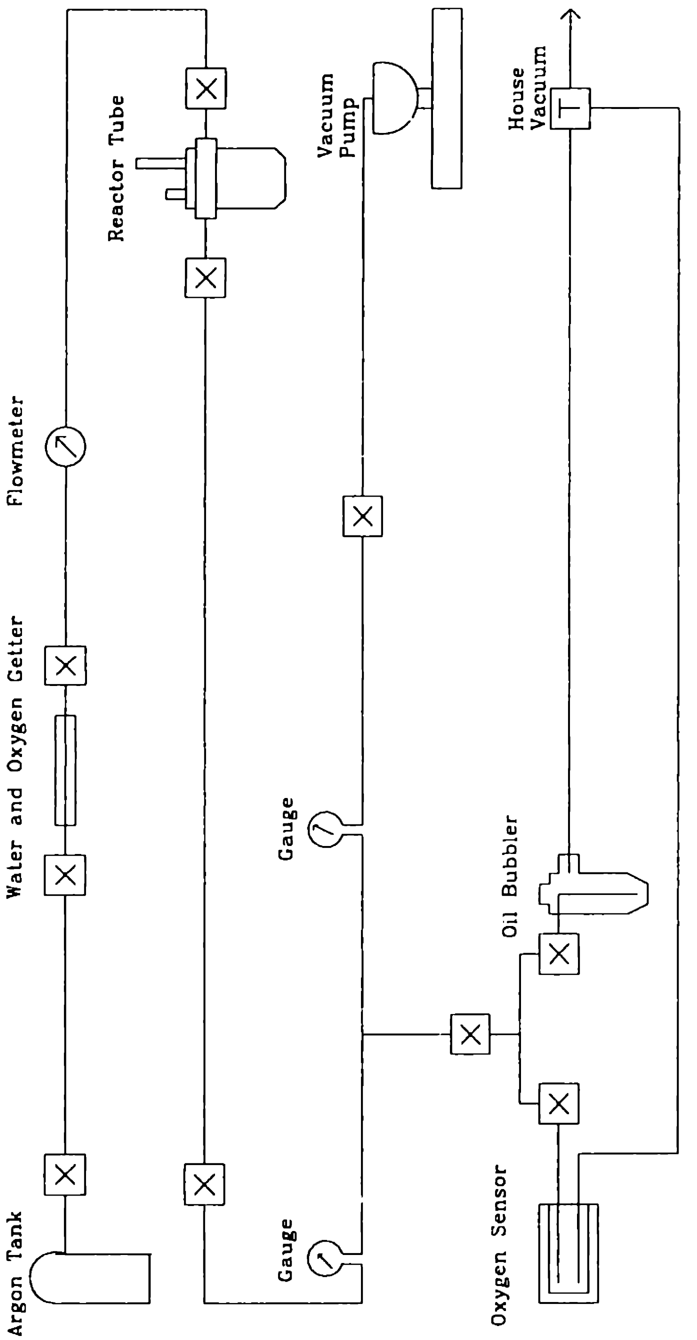

Figure 5.04: The Atmosphere Control System

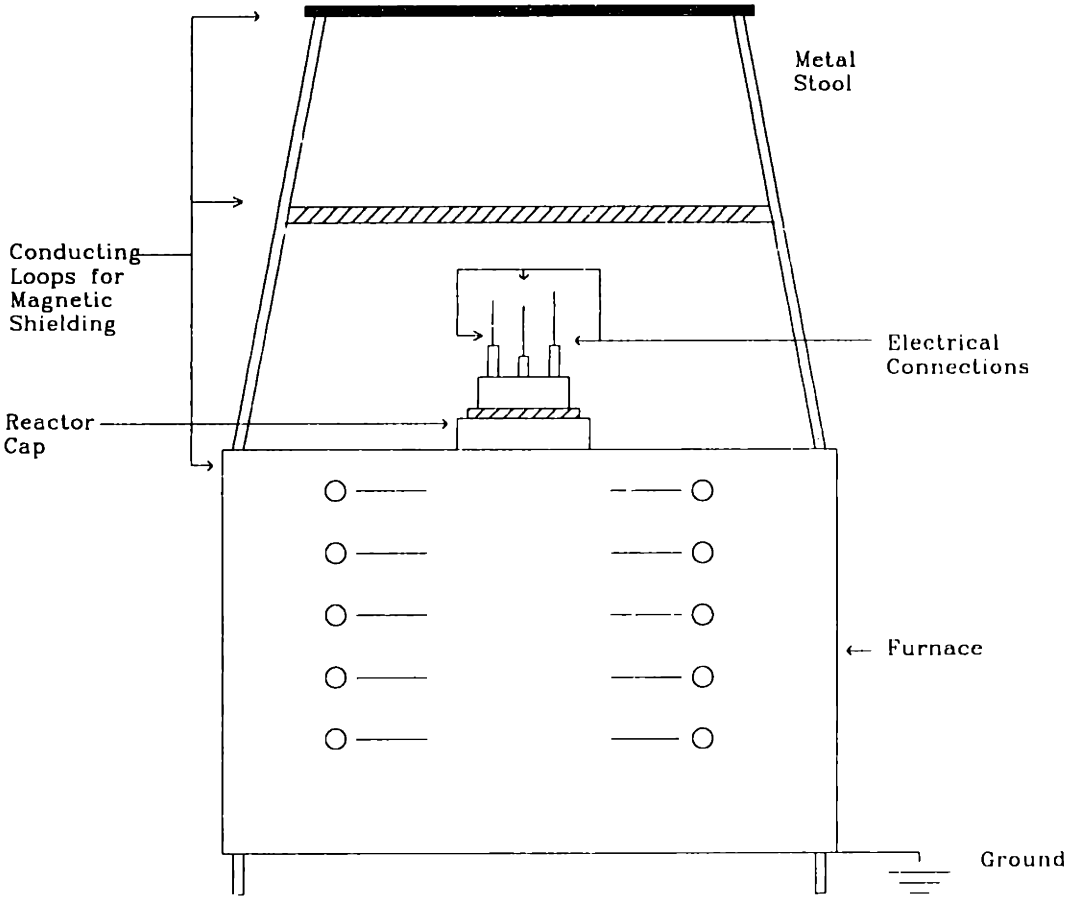

Figure 5.05: Apparatus for Magnetic Shielding

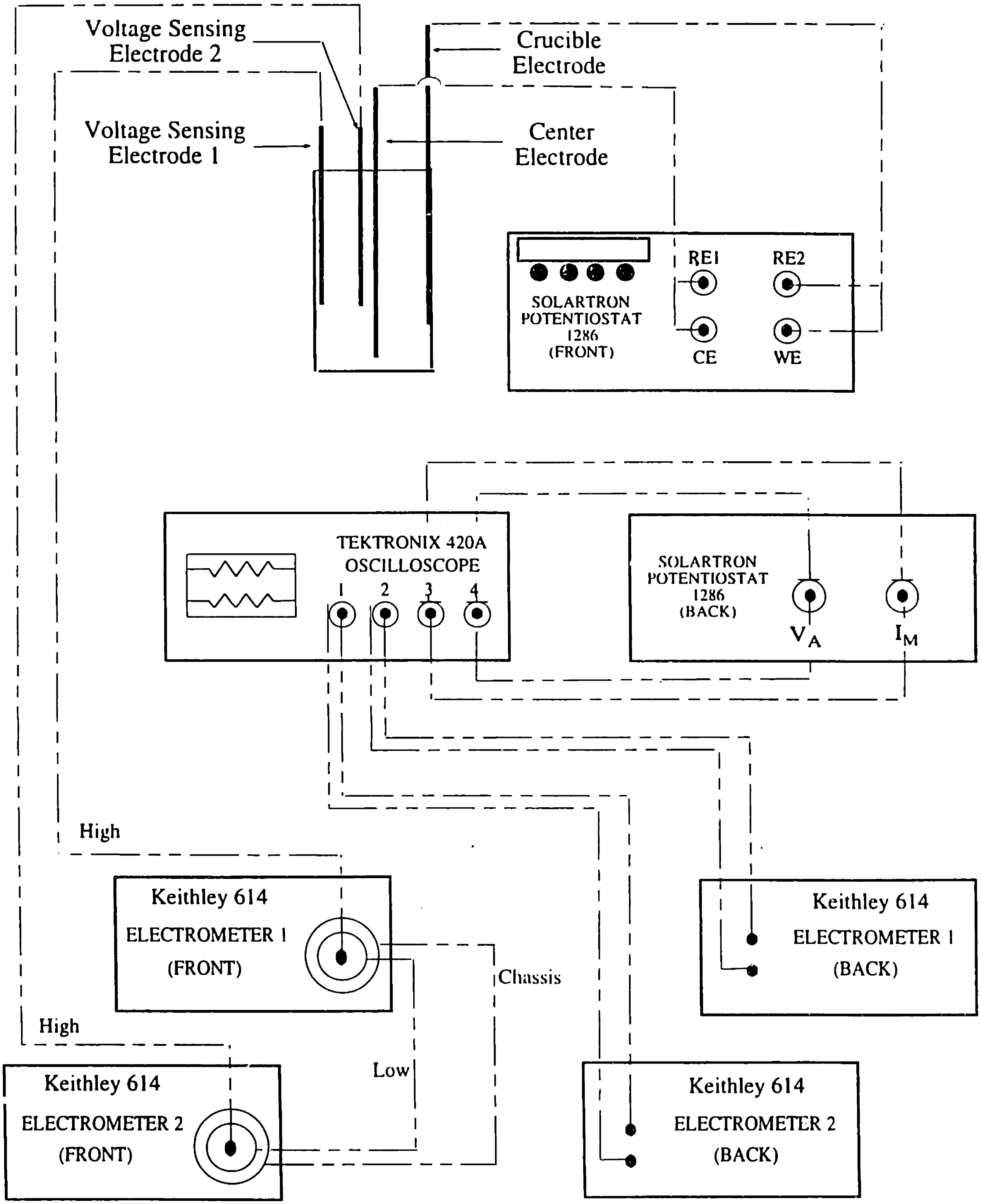

Figure 5.06: Electrical Connections for Conductivity Measurements of Systems with a High-impedance, Electrode-electrolyte Interface

Table 5.1 Weights of Powders Used for the Calibration Solution

salt	weight (grams)
NaCl	55.72 g
KCl	12.80 g

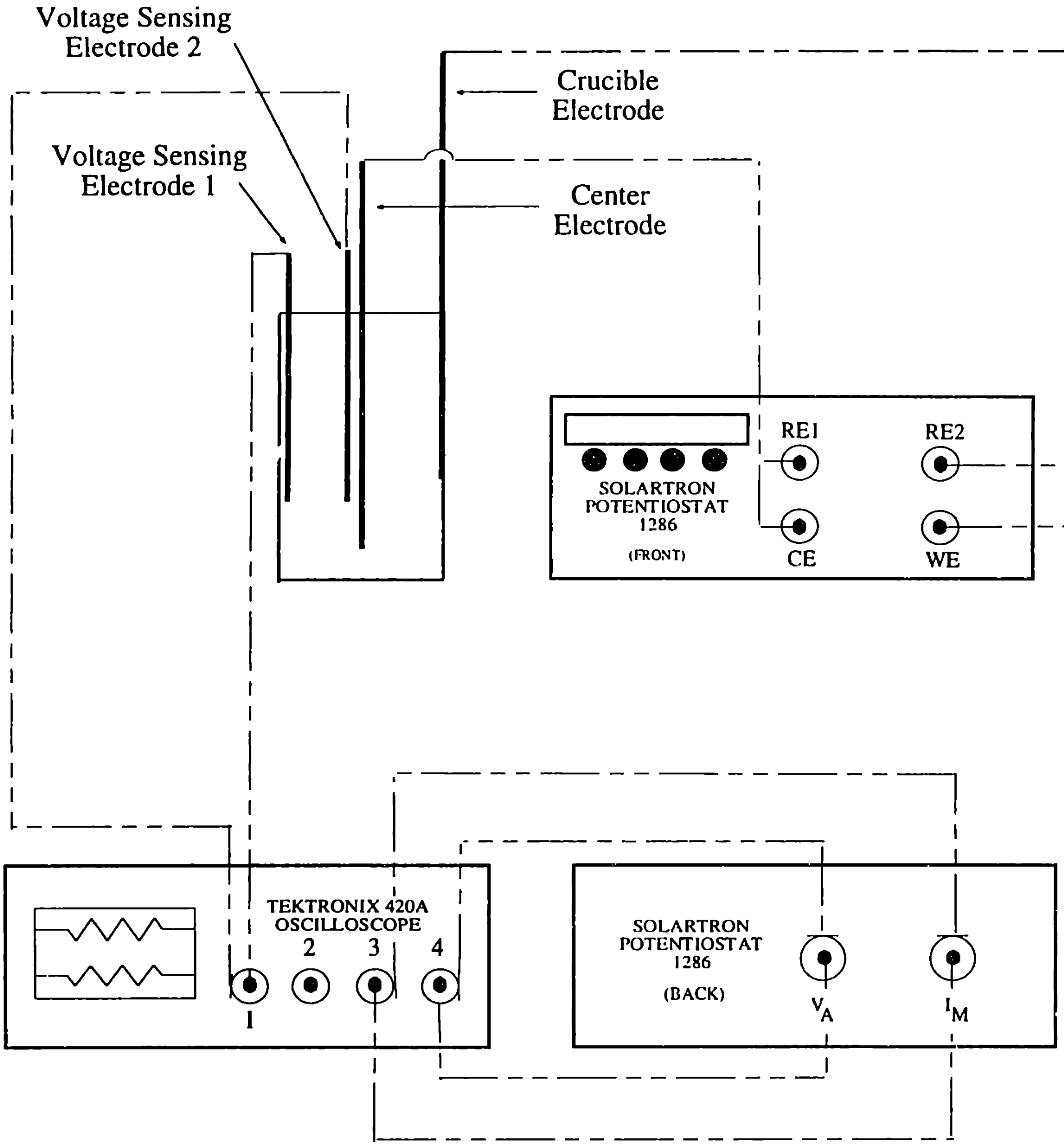

Figure 5.07: Electrical Connections for Conductivity Measurements of Systems with a Low-impedance, Electrode-electrolyte Interface

Table 5.2: Weights of Powders Used in the Molten Titanate Experiments

powder	33:67 mol% BaO:TiO_2 weight (grams)	27:73 mol% BaO:TiO_2 weight (grams)
BaO	98.01	83.67
TiO_2	103.60	117.91
MoO_2	2.03	2.02

Chapter 6: Results and Analysis

This chapter provides a detailed description of the data analysis protocol. The results are summarized and tested against various models.

6.1 Data Analysis Protocol

6.1.1 Data Analysis Technique for the Calibration Curve

6.1.1.1 Measurement Validity

In the system comprised of the chloride melt with blocking molybdenum electrodes, the electrode-electrolyte interface is modelled as a double-layer capacitor. (Figure 3.05 gives the equivalent circuit.) The model predicts that the application of a triangular voltage excitation yields a square wave current response and a square wave voltage that can be measured at the sensing electrodes. A square wave current response and corresponding square wave melt voltage were generally observed in the chloride system, as illustrated in Figure 3.06. When the current and resulting melt voltage failed to display square wave character[87], the likeliest cause was excessive electrical noise or contamination from the triangular excitation voltage, in which case the data were discarded.

6.1.1.2 Calculation of Melt Resistance of the Chloride Melt

The melt resistance between the voltage-sensing electrodes is found from the quotient of the voltage drop between these electrodes and the total current. The resistance calculation is performed as follows. First, the cell current and melt voltage data files

---

[87] The shape of the current and melt voltage responses were observed on the screen of the oscilloscope as they were measured.

stored in binary by the oscilloscope were converted to ASCII format using a utility provided by Tektronix.[88] Electrometers[89] measured the voltage at each of the two sensing electrodes. The absolute melt voltage was found by calculating the difference between these two voltages using the math utility "Diff_dat." The resulting melt voltage measurement was then smoothed using a 27-point running median and a 17-point mean algorithm. Smoothing removed noise and random spikes from the voltage measurement; DC offset was removed from both the voltage signal and current using "Zero_dat."[90] The selection criteria for the resistance values computed by dividing the voltage by the current are described below.

The current response in the molten chloride system was not perfectly square, but approximately square during one half-cycle (when the center electrode was negative) and triangular during the other half-cycle. The square half-cycle showed an initial transient response corresponding to the formation of the double-layer. Once the double-layer had formed, the current across it appeared as a flat region in the current response curve.

During the alternate half-cycle in which the center electrode was driven positive, the current response was triangular. This response may have been a result of the electrode acting in a non-blocking manner. Since the electrodes were made of molybdenum, an aliovalent metal, the non-blocking behavior may have been caused by a valence shift in trace amounts of molybdenum dissolved in the melt. Another possibility is that the anodic corrosion of the molybdenum electrode caused the observed behavior. Alternatively, excess chloride ions at the electrode during this phase of the cycle could have lead to the formation of molybdenum chloride ($MoCl_6$), which has a free energy of formation of 0.14 V at 873°C [52]. However, with an excitation signal of

---

[88] Tektronix "Cnvrtwfm" program was used to create files in ASCII format for use in spreadsheets.

[89] The electrometers shared a common reference ground from which to measure the voltage.

[90] Dr. Kevin Rhoads, MIT, Cambridge, MA

0.1 V, the formation of this compound is unlikely because the required voltage for this to occur must be in excess of the thermodynamic value plus an overpotential which can easily measure 100 mV.

Calculation of the melt resistance was made using measurements from the square wave half-cycle when the current and voltage were "flat." To identify this range, the beginning of each square wave half-cycle was found by locating the zero crossing, at which point the sign of the current changed. Next, the resistance values were examined within each square half-cycle to identify a minimum of four successive resistance values differing by less than 2%. In addition, resistance values corresponding to the invariant (flat) portion of the current and voltage signals were identified. Resistances identified in each cycle were averaged and the resulting average resistance (tabulated based on flat regimes of the resistance, current, or voltage) with the lowest standard deviation was accepted as the value of the raw melt resistance. This resistance was scaled according to the magnification factor of the electrometer and the current range of the 1286 to yield the reported resistance value.

6.1.1.3 Calculation of the Calibration Curve

From the resistance at each temperature and the corresponding theoretical electrical conductivity reported by Van Artsdalen *et al.* [51], the cell factor was calculated using equation (6.1).

$$G(\sigma) = \sigma \bullet R \tag{6.1}$$

$G(\sigma)$ is the conductivity dependent cell factor in cm^{-1}

σ is the electrical conductivity in S/cm

R is the measured resistance in Ω

Appendix C contains the resistances (in chronological order of collection), temperatures, accepted values of conductivities, and cell factors for the 15:85 mixture of KCl:NaCl used to calibrate the cell.

The dependence of cell factor on conductivity was found by plotting the derived cell factor against the theoretical conductivity for each temperature.[91] Figure 6.01 displays the calibration curve, (i.e., the relationship between cell factor and conductivity) for the crucible cell and electrode positions described in Chapter 5.

The cell factor as a function of conductivity for the calibration standard was fit to the linear function:

$$G(\sigma) = a + b\sigma \qquad (6.2)$$

$G(\sigma)$ is the conductivity dependent cell factor in cm^{-1}

a is the intercept of the calibration curve in cm^{-1}

b is the slope of the calibration curve in S

A good approximation for these data was achieved with a truncated power series ($a+b\sigma$ where $a=1.5816 \pm 0.02872$ $b=-0.39215 \pm 0.008593$), demonstrated graphically in Figure 6.01.[92] Figure 6.02 shows little change when a quadratic fit was used.[93] Therefore, it was determined that the linear fit adequately captured the relationship between cell factor and conductivity, and nothing was gained with the addition of higher order terms.

---

[91] Calibration of a conductance cell is typically done at a constant temperature of 25°C where the concentration of the solution is varied to give different conductivities. Typically these concentrations are 1.0, 0.1, and 0.01 demal KCl. For molten halide calibration standards, each temperature represents a unique conductivity and thus can be viewed as an independent standard.

[92] From Taylor's theorem, over a limited range of the independent variable, any function without singularities or cusps can be represented with a power series.

[93] Also, the goodness of a quadratic fit was statistically very low.

6.1.1.4 Statistical Check of the Calibration Curve

Statistical tests of the calibration were conducted to confirm the goodness of fit. First, the existence of a correlation between cell factor and conductivity was tested. The Kendall test of correlation yielded a confidence level of 95% that the data were indeed correlated and not random. The Spearman test of correlation reported a probability of correlation of 98%.[94] Appendix C contains a summary of these statistical results.

Following the correlation between the cell factor and conductivity, the data were fit to a line. A very small χ^2 [95] of 0.002 was calculated, implying a good fit of the data to the line. Additionally, a Gaussian linear R^2 value of 0.922 was calculated. However, both of these measures of goodness of fit are based on assumptions about the data that cannot be confirmed. χ^2 is used to determine of the goodness of fit of data to a model when the weighting of each data point is known. The relative weightings were not known for these data and, as a result, the χ^2 measure has questionable validity. For the linear Gaussian R^2 an assumption of Gaussian distribution of the error in the data is assumed. Again, the distribution of error in the cell factor and conductivity are unknown. Statisticians recognize that these measures of goodness of fit (χ^2 and R^2) are often poor indicators of the fit between a data set and a model [53]. Typically a poor χ^2 value is accepted for data in which a good visual fit is found. Figure 6.01 displays the linear fit of the data. Appendix G provides a detailed error analysis of the uncertainty in the calibration curve and the measured molten oxide conductivities.

---

[94] The Spearman test, Kendall test, and statistical fittings were conducted using the program "Fit_find" written by Dr. Kevin Rhoads.

[95] χ^2 is calculated based on the difference between an actual data point and the fit. The lower the χ^2 the better the fit. However, the magnitude of the data will have a tremendous influence over the magnitude of the χ^2 value. χ^2 is more useful in comparing the relative goodnesses of two fits of the same data set.

6.1.2 Data Analysis Technique for the Molten Oxides

6.1.2.1 Calculation of the Melt Resistance of Molten Oxides

The equivalent circuit for the molten titanates is given in Figure 3.04. Owing to a low-impedance interfacial path modelled as a resistor, triangular voltage excitations produce triangular currents, yielding triangular voltages across the sensing electrodes.

The melt voltage and total current measurements recorded by the oscilloscope were converted from binary to ASCII. Smoothing was unnecessary because the oxide current and voltage measurements exhibited good signal-to-noise ratios. Both signals were zeroed. The mathematical operations of dividing matching time-based melt voltages by currents and then averaging the resulting resistances to produce a melt resistances value for each temperature was accomplished using "Read_Dat," a program written expressly for this investigation[96].

In the resistance calculation, very small currents (less than 10% of the average current value) and the corresponding voltages were discarded to minimize the inclusion of any erroneous, extremely large resistances. Additionally, the two measurements of voltage and current before and after each zero crossing were eliminated because the 1286 potentiostat displayed a discontinuity in the applied voltage near the zero value. The remaining resistance values were averaged within each cycle and the computed cycle average was taken as the raw melt resistance. Raw melt resistances with a high standard deviation relative to the other values were also discarded. Each remaining raw resistance was scaled in accordance with the 1286 current measuring range used to calculate the actual resistance value.

---

[96] Dr. Kevin G. Rhoads, MIT, Cambridge, MA

6.1.2.2 Calculation of the Electrical Conductivity

The electrical conductivity of the molten titanates was calculated at each temperature using the measured resistance and the functional relationship between cell factor and conductivity derived from the chloride calibration. Combining equations (6.1) and (6.2) yields:

$$\sigma = (1/R)(a + b\sigma) \qquad (6.3)$$

which can be rearranged to give:

$$\sigma = a/(R - b) \qquad (6.4)$$

Based on this result, the intercept from the calibration curve (a) was divided by the difference between the measured resistance and the calibration curve slope (b) to give the conductivity of the molten oxide. Appendix D contains the resistances and resulting conductivities for the molten oxides measured.

6.1.2.3 Calculation of Transference Numbers

Transference numbers are used to indicate the fraction of the total conductivity carried by the specific species [54]. The sum of the anionic and cationic transference numbers is the ionic transference number. The electronic transference number represents the sum of the transference numbers of the electronic species or the percentage of the total conductivity carried by electronic carriers. The sum of the ionic and electronic transference numbers is one.

$$t_{ionic} + t_{electronic} = 1 \qquad (6.5)$$

$t_{electronic}$ is the transference number of all electronically conducting species

t_{ionic} is the transference number of all ionic species

Transference numbers for the molten oxides were calculated from the current response to the application of a stepped potential. The value of the initial peak represents the total current and is proportional to the total melt conductivity. At equilibrium, the only current flowing is from the electronic charge carriers. Taking the ratio of the equilibrium current to initial current gives the electronic transference number (equation (6.6)).

$$t_{electronic} = I_{field\ equilibrium} / I_{field\ initial} \qquad (6.6)$$

$I_{field\ equilibrium}$ is the long-term current under an applied field

$I_{field\ initial}$ is the initial current under an applied field

The difference between the equilibrium current and the initial current divided by the initial current is the ionic transference number (equation (6.7)).

$$t_{ionic\ field} = (I_{field\ initial} - I_{field\ equilibrium})/I_{field\ initial} \qquad (6.7)$$

The ratio of the relaxation current after removal of the applied field to the initial current is a second method for computing the ionic transference number (equation (6.8)).

$$t_{ionic\ relax} = I_{relaxation} / I_{field\ initial} \qquad (6.8)$$

$I_{relaxation}$ is the initial relaxation current when the applied field is removed

The values of the ionic transference numbers calculated by equations (6.7) and (6.8) were in good agreement, differing by less than 3-5% for all compositions and temperatures. Table 6.1 lists the computed transference numbers as a function of temperature and composition.

All the square wave measurements displayed a non-zero, DC current offset of 100-150 mA at open circuit. This current is possibly a result of a small potential difference due to compositional differences between the molybdenum crucible and rods. The average current offset was calculated and subtracted from the entire current response wave. Figure 4.02 displays a typical plot after removal of the DC offset. Appendix E contains a summary of the relative current peak responses for the oxide melts investigated. Appendix F contains the graphs of the square wave response of the two compositions at the various temperatures. For ease of viewing, all graphs were plotted with the initial response to the applied voltage[97] inverted.

6.2 Analysis and Results

6.2.1 Electrical Conductivity as a Function of Composition

At constant temperature, the electrical conductivity of TiO_2-BaO melts is lower for higher TiO_2 concentrations across the compositional range examined. Figure 6.03 displays electrical conductivity as a function of temperature for the two compositions studied. Examination of isotherms of the 67:33 and 73:27 TiO_2:BaO melts reveals a higher total conductivity in the 67 mol% TiO_2 melt at all measured temperatures. The magnitude of the conductivity for the 67 mol% TiO_2 melt ranged from 3.97-3.99 over the temperature range 1327-1477°C and 3.96-3.97 for the 73 mol% TiO_2 melt from 1387-1477 °C.

---

[97] The applied voltage for the 67 mol% TiO_2 melt was -0.1 V. Because of the limitations of the ammeter in the 1286, -0.08 V was used for the 73 mol% TiO_2 melt.

6.2.2 Electrical Conductivity as a Function of Temperature

The aim of this section is to examine the nature of the charge carriers in molten TiO_2-BaO based upon the temperature dependence of conductivity, beginning with a brief summary of the types of electrical conduction.

6.2.2.1 Summary of Types of Electrical Conductivity

The electrical conductivity of a material can be classified according to the type of charge carrier: electron (or hole) or ion. Within the category of electronic conductors, there is metallic and semiconducting behavior. In metals, the conduction band is partly full. Because the conduction band of a metal has many carriers, increasing temperature results in a decrease in the conductivity as lattice vibrations increase and the mean free path decreases.

Semiconductors, another class of electronic conductors, have some carriers in the conduction band. The class of semiconductors can be further divided into: intrinsic semiconductors which show increasing conductivity with increasing temperature; and extrinsic semiconductors which display decreased conductivity as temperature is increased[98].

Materials displaying ionic conduction are generally divided into three groups: those that are electrolytes, others that display fast ion conduction, and insulators.

---

[98] At sufficiently high temperatures, extrinsic semiconductors show the same temperature dependence as intrinsic semiconductors.

6.2.2.2 General Temperature Dependence of Electrical Conductivity for TiO_2-BaO Melts

For the compositions examined, the temperature coefficient of conductivity was positive (i.e., as temperature increased, conductivity increased). Several models for conductivity as a function of temperature were tested and the most plausible model identified. The following sections review the various models tested and assess how well each fits the data measured in this study.

6.2.2.3 Ionic Conduction Model

The electrical conductivity of ionic melts such as molten salts is often fit to an Arrhenius-type model [55]. The general expression for ionic conductivity is [56]

$$\sigma = ne^2/kT\ D_o \exp(-E_D/kT) \qquad (6.9)$$

n is the particle density in molecules/cm^3

e is the charge on an electron in C

D_o is the pre-exponential diffusion constant factor in cm^2/s

When the dependence on T^{-1} in the pre-exponential term in equation (6.9) is weak, it can be absorbed into a σ_o term to give equation (6.10).

$$\sigma = \sigma_o \exp(-E_D/kT) \qquad (6.10)$$

Over limited temperature ranges for some materials, a plot of ln σ vs 1/T will be linear. The temperature dependence of conductivity of molten salts is often fit using equation (6.10) [55].

Ionic glasses, a class of materials relevant to this study, have been well characterized. Ionic glasses exhibit only one conduction process with a single activation energy over the entire temperature range [57]. Typical activation energies of conduction for ionic solids are the sum of the defect formation activation energy (2 to 4 eV) plus the migration activation energy term (0.05-1 eV) for a total activation energy greater than 2 eV. For the class of ionic materials known as fast ionic conductors, where ion transport can occur on partially-occupied, disordered sublattices, the concentration of charge carriers is larger and normal activation energies are smaller, on the order of 0.05-1 eV [56].

The activation energy for ionic conduction in liquids is generally lower than that in solids. For example, molten chlorides, nitrates, and carbonates have activation energies of 0.15-0.3 eV [58].

Figures 6.04 and 6.05 show that the data for both compositions fit well to a plot of ln σ vs 1/T. The activation energy calculated from these fits was 0.01 eV. This activation energy, however, is inconsistent with the magnitude of the activation energy generally measured for ionic glasses. The activation energy is also an order of magnitude smaller than that of fast ion conductors or ionic liquids. However, if the data are fit to an expression for ionic conductivity in which the temperature dependence is not absorbed into the pre-exponential term (lnσ•T vs 1/T), the activation energy calculated is 0.15-0.16 eV, a magnitude in keeping with values reported for ionic liquids.

6.2.2.4 Semiconducting Model

For intrinsic semiconductors, the temperature dependence of conductivity is primarily a function of changes in carrier concentration. For annealed III-V amorphous semiconductors and chalcogenide glasses [59], the electrical conductivity displays an exponential dependence on 1/T. That is, ln σ vs 1/T is linear.

While ionic melts and semiconducting melts can exhibit the same temperature dependence (ln σ vs. 1/T is linear), semiconducting materials display separate high and low temperature activation energies while ionic melts display a single activation energy.

Due to the high temperatures at which the conductivity of the molten titanates were measured, even if the melt is modeled as a semiconductor, only a single, high temperature activation energy may be observed. It is also possible that the conductivity of this melt was measured in only one of the two possible semiconducting regimes.

The direct band-gap for many common semiconductors at room temperature is around 0.4-0.7 eV [60]. The band-gap energy can be considered the activation energy of the conduction process, that is the amount of energy needed to inject carriers into the conduction band. MacKenzie [61] calculated the activation energy for a semiconducting vanadium glass with barium and germanium to be around 0.5 eV. For liquid semiconductors, activation energies of 0.2-0.3 eV have been reported [62]. The magnitude of the activation energy for a semiconductor is an order of magnitude larger than that calculated for these melts, making it unlikely that this melt is a pure semiconductor.

6.2.2.5 Polaron-Hopping Conduction Model

Polaron hopping, a form of semiconduction used to explain the behavior of solid TiO_2, is another potential model for the conduction mechanism in this system. Polarons are quasi-particles associated with band-bending and electron trapping. In solid transition-metal oxide glasses with mobile cations, this conduction processes contributes differently to the electrical conductivity at different temperatures, resulting in different values of activation energies [63]. The polaron hopping model of electrical conduction gives the following relationship between conductivity and temperature:

$$\sigma_{dc} = (\gamma N e^2 R^2/kT) C(1-C) \exp(-2\alpha R) \exp(-W/kT) \qquad (6.11)$$

γ is the characteristic phonon frequency

N is the number of transition metal ion sites/cm^3

R is the site spacing

C is the mole fraction of site occupied by electrons

α is the electron wave function decay constant

W is the activation energy arising from electron lattice interaction and/or static disorder

$W = W_h + 1/2W_d$ for $T>\theta_{D/2}$

$W = W_d$ for $T<\theta_{D/4}$

W_h is the polaron hopping energy.

W_d is due to static disorder

θ_D is the Debye temperature ($\theta=\gamma/k$)

This model predicts a linear relationship between ln $\sigma \bullet T$ and $1/T$. Furthermore, materials with polaron hopping are expected to show transitions at critical temperatures. The conductivity and temperature data from the TiO_2-BaO melts displayed a good linear fit between $\ln(\sigma \bullet T)$ and $1/T$. See figures (6.06) and (6.07). No transition or change in the slope of the $\ln(\sigma \bullet T)$ vs $1/T$ plot was observed, although it is possible that this transition occurred at a temperature outside the range studied.

The activation energy calculated from a plot of ln $\sigma \bullet T$ vs $1/T$ was on the order of 15 kcal/mole or 0.2 eV. The activation energy for polaron hopping is estimated to be 0.3-0.4 eV [64], making polaron hopping conduction a possible conduction model for this system.

6.2.2.6 Mixed Conductor Model

Mixed conduction occurs in materials where both ionic and electronic conduction occur. Mixed conductors such as $Li(Na)_xMo_2O_4$ [44] display the following relationship between electrical conductivity and temperature:

$$\sigma=1/T \bullet A\exp(E/kT) \qquad (6.12)$$

Plots of ln(σ•T) vs 1/T are linear for mixed conductors. In studying the $Ce_{1-x}Gd_xO_{2-x/2}$ system, Kudo *et al.* [65] found mixed conduction with an ionic activation energy of 0.55 to 1.3 eV and an electronic activation energy of 0.5 eV.

For a mixed conducting system depending on the temperature regimes and the relative activation energies, one mechanism appears to dominate. The activation energy predicted by this model for the molten oxides is appropriate for a mixed conductor and will be discussed in more detail following an examination of other measurement results.

6.2.3 Magnitude of Conductivity Near the Melting Point

The conductivities measured for the solid were of the same order of magnitude as those of the liquid. The TiO_2-BaO melts did not exhibit a large, abrupt change in conductivity typical of ionic melts. For electronic melts, conductivity is a smooth function of temperature in the neighborhood of the melting point.

Figure 6.08 shows the conductivity of the 73 mol% TiO_2 above and below the melting point (ca. 1317°C). The appearance of a higher conductivity in the solid can be explained by recognizing that this melt is a eutectic mixture whose frozen compounds differ in composition from that of the original liquid. Furthermore, this mixture goes through a two-phase (liquid and solid) regime in which the liquid has a lower TiO_2 content than the original liquid. It has been observed that mixtures of lower TiO_2 content display higher conductivities. The phase diagram for this system is given in Figure 1.01.

The purpose of this measurement was to determine if a large discontinuity existed in the conductivity at the melting point. The measurement of the conductivity of the solid was not optimal but served to indicate the relative magnitude of the solid and liquid conductivities. The conditions under which the conductivities of the solid and liquids were measured were not identical. Specifically, the measurements of the solid were made with the thermocouple frozen in the specimen, while the measurements of the liquids were done with the thermocouple retracted from the melt. During the solid measurements, the thermocouple, sheathed in a conducting molybdenum tube, distorted the electric field relative to the field in the liquid measurements, which in turn caused a change in the current path and affected the cell factor.

6.2.4 Results from the Stepped Potential Experiments

6.2.4.1 Shape of the Response Current Response Curve

The shape of the response current during the application and removal of a stepped potential (square wave) can be used to determine the nature of the melt conductivity. For all compositions and liquid temperatures examined, the melt showed a finite, long-term decay in the current response. The long-term current was non-zero, indicating an electronic component to the melt. Furthermore, the removal of the square wave resulted in a non-zero relaxation current indicating the presence of an ionic current[99] in the melt. Figure 4.02 is a typical response curve. Appendix F contains the complete set of responses measured.

6.2.4.2 Transference Numbers

The method for calculating the transference numbers was given previously. Table 6.1 reports the transference number for each melt as function of temperature. Both melts exhibited non-zero electronic and ionic transference numbers. An examination of the transference numbers as a function of composition, indicate that, on average, as the titanium content of the melt decreased, the ionic transference numbers increased.

---

[99] The ionic current detected after the removal of the applied potential is a diffusional current, resulting from the concentration gradient of ions which develops during the applied potential.

For a given composition, an increase in temperature resulted in a slight increase in the electronic transference number and a corresponding small decrease in the ionic transference number. Figure 6.09 shows the electronic and ionic transference numbers as a function of temperature.

6.2.4.3 Calculation of the Ionic Activation Energy

The ionic portion of the total conductivity for the TiO_2-BaO melt was calculated by multiplying the total conductivity by the ionic transference number for each temperature at which the total conductivity and transference numbers were known:

$$\sigma_{ionic} = t_{ionic}\sigma_{total} \qquad (6.13)$$

σ_{ionic} is the ionic conductivity in S/cm
t_{ionic} is the ionic transference number
σ_{total} is the total conductivity in S/cm

Figure 6.10 shows the ionic conductivity as a function of temperature. The activation energy for the ionic process was found from the relationship between the natural log of the ionic conductivity and temperature (equation (6.10)). For the 67 mol% TiO_2 melt[100] an ionic activation energy of 10-13 kcal/mol (0.44-0.57 eV)[101]. This is in agreement with the activation energy for conduction, 15 ± 3 kcal/mol[102], for Ba^{2+} measured by Bockris [10] in a 55:45 mol% BaO:SiO_2 melt.

---

[100] There were too few points to calculate a reliable value for the ionic activation energy for the 73 mol% TiO_2.

[101] The calculation of 10 kcal/mole was based on the slope from the plot ln σ_{ionic} vs. 1/T. When ln (σ_{ionic}•T) vs 1/T is used, an activation energy of 13 kcal/mol is measured.

[102] Bockris reported the activation energy for a variety of silicate melts with lower BaO content. Clearly, as the BaO content increases, the activation energy decreases, making an activation energy of 10-13 kcal/mol reasonable for the melt studied in this work.

6.2.4.4 Calculation of Ionic Diffusion Constants

The diffusion constant for the ionic species in this melt was calculated from the Nernst-Einstein equation (6.14) which relates the diffusion constant to the conductivity.

$$D_i = kT\sigma_i/ne^2 \qquad (6.14)$$

D_i is the ionic diffusion constant in cm^2/s

σ_i is the ionic conductivity in S/cm

The ionic diffusion constants[103] for these melts were on the order of 5×10^{-5} cm^2/s. This figure is typical of diffusion constants for liquids.

6.2.4.5 Comparison of Total Conductivity Calculated from the Square Wave With the Total Conductivity Measured with the Triangle Wave

The square wave current-decay model presented in Chapter 4 postulates that the current in the $t=0^+$ region represents the total melt conductivity. As an additional check of the validity of this model, the total conductivity calculated from the $t=0^+$ current and melt voltage can be compared to the total conductivity measured when the triangle wave excitation was used. Table 6.2 presents the raw resistances measured at $t=0^+$ for the square wave, the resulting conductivities, and the resistances and conductivities calculated by triangle wave measurements at the same temperatures.

The peak current and melt voltage measurement after the square wave had been applied were used to calculate the melt resistance and total conductivity. Table 6.2 shows that the resistances measured at $t=0^+$ were generally 5-10% higher than the resistances measured with a triangle excitation signal. This discrepancy is most likely a result of

---

[103] The ionic diffusion constant was calculated based on a density estimate for these melts of 10^{22} molecules/cm^3.

instrumental measurement speed[104]. The small, systematic difference in resistances measured with the triangle and square wave excitation adds further credence to the model proposed in Chapter 4 for the source of the current decay.

6.3 Experimental Models for Molten TiO_2-BaO

In this section, the viability of potential conduction models is examined in light of the results and observations found through this research.

6.3.1 Macroscopic Model of Electrical Conduction

The positive temperature coefficient of conductivity is indicative of either an ionic, semiconducting, or mixed conducting mechanism. Metallic conduction can be excluded based on the temperature coefficient of conductivity.

The existence of electronic character in these molten oxides is indicated by the non-blocking behavior of the molybdenum electrodes at voltages below the decomposition voltage, particularly, in the shape of the current and melt voltage when a triangular waveform is applied. Non-blocking behavior occurs only in systems with a common element in the melt and electrode, or when there is an electronic pathway in the melt. Since there is no common element in the electrodes and melt, this system must have at least some degree of electronic conduction.

Though the activation energy predicted by the ionic conduction model when the temperature dependence in the pre-exponential term is not ignored was reasonable for an ionic liquid, the TiO_2-BaO melts examined are not purely ionic. Unlike purely ionic melts, compositions of TiO_2-BaO did not display a significant discontinuity in

---

[104] The oscilloscope was collecting current and melt voltage measurements at a rate of 5 measurements per second during the square wave experiment. This rate may not have been fast enough to catch the true $t=0^+$ values before diffusion currents began to contribute to the values.

conductivity when melting. Additionally, the non-zero long-time current measured when a DC square wave was applied is not characteristic of purely ionic materials.

Similarly, it is unlikely these melts are purely semiconducting because the activation energy calculated from the data based on a semiconducting model, 0.01 eV, was an order of magnitude smaller than that expected for a purely semiconducting melt (0.2-0.3 eV.)

Based on the goodness of the fit of ln $\sigma \bullet T$ vs 1/T and the activation energy calculated from this model (~0.15 eV), these melts can best be modelled as displaying mixed conduction, namely ionic and semiconducting. The activation energy calculated from the mixed conductor model agrees with that found for solid semiconducting materials. There is also a good fit to the polaron hopping model.

The presence of mixed conduction is also supported by the incomplete decay in the melt current response to the application and removal of a square wave. The transference numbers derived from this experiment indicate a predominantly electronic melt with a 10-20% ionic character.

6.3.2 Atomistic Model

The macroscopic model of mixed ionic and semiconducting character can be extended to include a molecular explanation. An increase in the barium oxide composition in these melts results in an increase in the total conductivity and an increase in the ionic transference number. The data indicate that barium oxide, a known ionic conductor, is responsible for the ionic conduction present. Based on the correlation between increased titanium dioxide and decreased ionic transference numbers, the titanium ion, in any form[105], cannot be responsible for the ionic character of the melt.

Titanium dioxide, a known solid semiconductor when non-stoichiometric, may be responsible for the electronic character of the melt. This is supported by the observation that an increase in the titanium dioxide content results in an increase in the electronic character of the melt.

The titanium ion is aliovalent, displaying +2, +3, and +4 oxidation states. The electronic conduction by the titanium dioxide is postulated to be a hopping mechanism in which an electron jumps from tri-valent to tetra-valent ions. Because of the high TiO_2 content, a tri-valent titanium ion is expected to easily find at least one tetra-valent neighbor, making the current path from electrode to electrode fairly linear at these composition ranges. Small additions of titanium dioxide to the composition are expected to have minimal effect on this conduction path. As a result, changing the TiO_2 composition from 67 to 73 mol% (a 9% increase) only marginally increases the electronic conduction but significantly decreases the ionic conductivity. The corresponding, 30% relative change in the ionic barium is significant. Each additional molecule of barium oxide is expected to contribute directly and noticeably to the overall ionic conductivity. Because the change in ionic character dominates, the net effect of decreased titanium dioxide content is a small increase in overall conductivity.

The possible existence of an extended, three-dimensional titanate polymer network analogous to that found in silicate systems is consistent with the observed electrical behavior of this melt. The decrease in total conductivity observed when the TiO_2 content rises is consistent with the hypothesis that a polymer network is being increased.

---

[105] In a melt, an ion of titanium is not likely to exist as a naked Ti^{4+}, but rather as part of an anionic complex with oxygen. Aluminum is an example of a metal ion that exists in a complexed form when ionized. Aluminum is found in cryolite as either as AlF_4^- or AlF_6^{3-}.

However, Handfield, *et al.* [66] reported that high TiO_2 content melts exhibit low viscosity, an observation inconsistent with the presence of a polymer network.

In summary, the data suggest that these melts are mixed conductors with barium carrying the ionic charge and titanium dioxide responsible for the electronic conduction. TiO_2 conducts via a semiconducting mechanism in which electrons hop from one titanium ion to another. The existence of TiO_2 in an extended polymer network is neither proved nor disproved by the data. Spectral data are needed to determine the presence of a polymer network.

6.4 Comparison of these Results with those in the Literature

The results of this work show the electrical conductivity of these molten titanates to be around 4 S/cm. Appendix G provides estimates of the uncertainty in these measurements. There is no work in the literature that is directly comparable with the present study because of significant differences in composition.

These results are on the edge of agreement with Van Arkel's value of 10 ± 5 S/cm for pure TiO_2 at an unspecified temperature. Klinchikov's report for the conductivity of titanium dioxide with the divalent counter-oxide, magnesium, at various compositions range from 13.5 S/cm for high magnesia materials to 25.6 S/cm for a 50:50 mixture. It is not possible to reconcile the results of this work with Klinchikov's since the experimental details and temperature were not reported.

Desrosiers *et al.* reported electronic conduction for melts of similar titanium dioxide content (66-79 wt% TiO_2) but containing a variety of other elements including multivalent iron and chromium. Desrosiers' slags, containing 66-79 wt% TiO_2, exhibited conductivity in the range 24-57 ± 10-30 S/cm. The high iron content of these slags makes a comparison with this study problematic. Desrosiers' conclusions about the conductivity mechanism are, however, in agreement with the models proposed in this work. Desrosiers concluded that the conductivity was a function of the oxidation state of titanium. The mechanism was postulated to be a random walk of electrons between tetra-valent and tri-valent titanium dispersed in the melt. Desrosiers *et al.* report an activation energy of 0.1 ± 0.04 eV for a 66% TiO_2 slag based on the Arrhenius-type model, an order of magnitude larger than that found when the data in this study were fit to an Arrhenius-type model.

Mori [8], who worked with iron titanates with a titanium dioxide composition nearly identical to one used in this work, reported that at 1430°C a melt of 68 mol% TiO_2 has a specific electrical conductivity of 50 S/cm. This study measured an electrical conductivity of 3.966 S/cm for a 67 mol% TiO_2 melt at 1433°C.

The presence of iron in Mori's melt results in a major difference between his work and this study. In addition, a significant source of error in Mori's measurements results from calibration of his crucible cell with 0.01N KCl (conductivity of 0.01 S/cm.) As discussed earlier, calibration of a crucible cell with a standard that differs by 2-3 orders of magnitude from the conductivity of the specimen under investigation makes accurate measurements impossible. Mori's observation that conductivity increases when the titanium dioxide content of the melt exceeds 40% was not confirmed by this study.

This study supports the observation of Denisov *et al.* of a weak temperature dependence and the existence of semiconduction in the melt. The magnitude Denisov reported (150-180 S/cm) for iron titanate slags in the range of 80-90% titanium dioxide is not consistent with this work. This discrepancy may be attributed to the iron content of Denisov's slags and the use of a low-accuracy crucible or dipping-electrode cell.

Bockris *et al.* studied the binary of silica and 10% titanium dioxide. The conductivity calculated for this silica rich melt was 6.3×10^{-4} S/cm. This measurement was done with a two point crucible style cell and the cell factor was calculated based on geometry. The activation energy for the conductance process, based on the movement of cations from one interstitial hole in the silicate network to the next, was reported to be 50 kcal/mol (2.2 eV) at 1800°C. The magnitude of Bockris' activation energy is indicative of ionic transport, in contrast to this study that found an activation energy of 0.15-0.16 eV. Bockris' high silica and low titanium dioxide concentration is the most likely source of the divergence in reported values.

In summary, the results reported here differ from those available in the literature. The primary factors contributing to these discrepancies are: (1) most commonly, the use of compositions with significant iron content, and (2) the use of inaccurately calibrated conductance cells. In view of the improved accuracy of the four-point crucible technique developed for this research over the existing techniques, the measurements of TiO_2-BaO melts presented in this work are considered to be more reliable and accurate than those found in the literature.

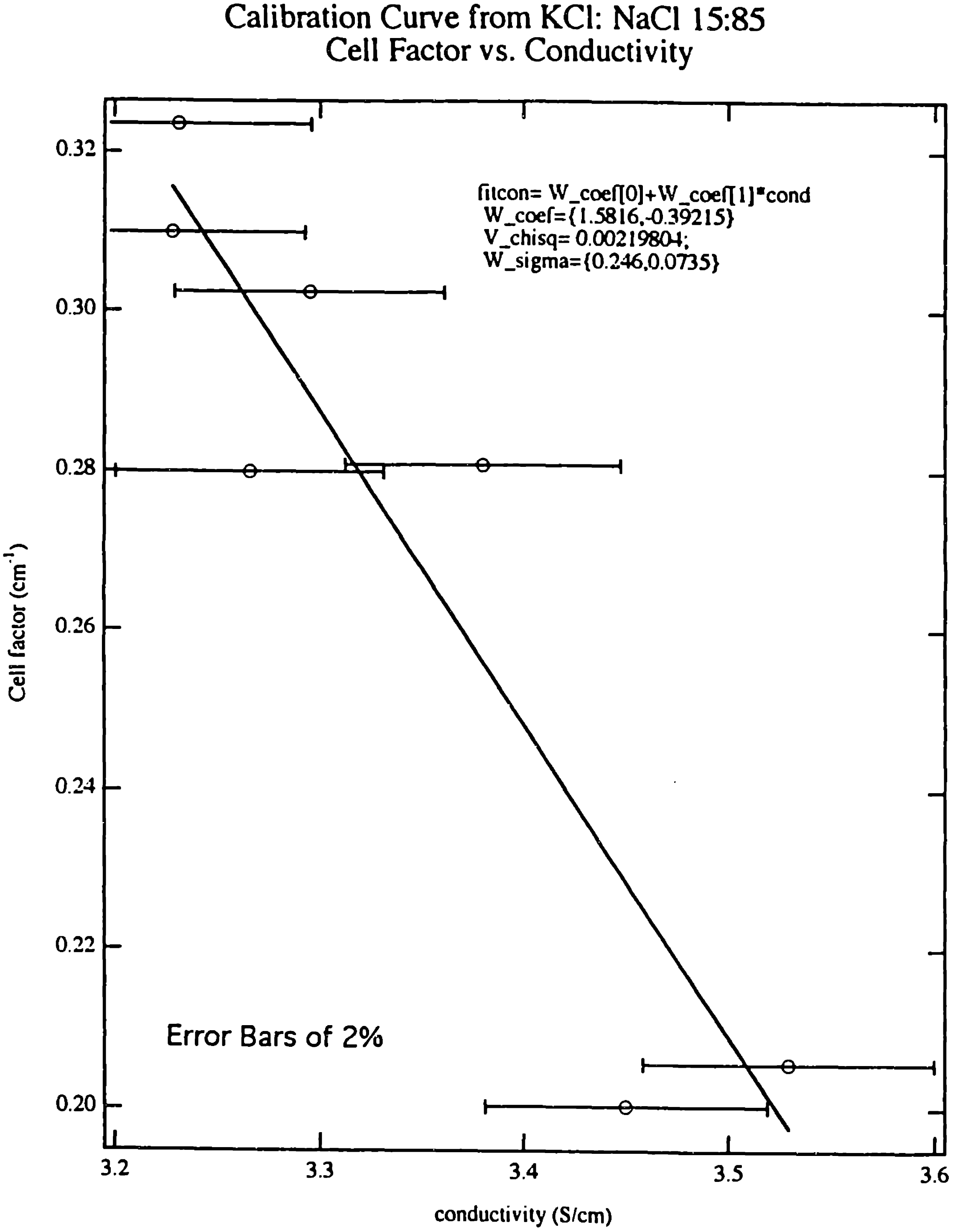

Figure 6.01: Linear Fit of Cell Factor vs. Conductivity for Chloride Calibration Standard

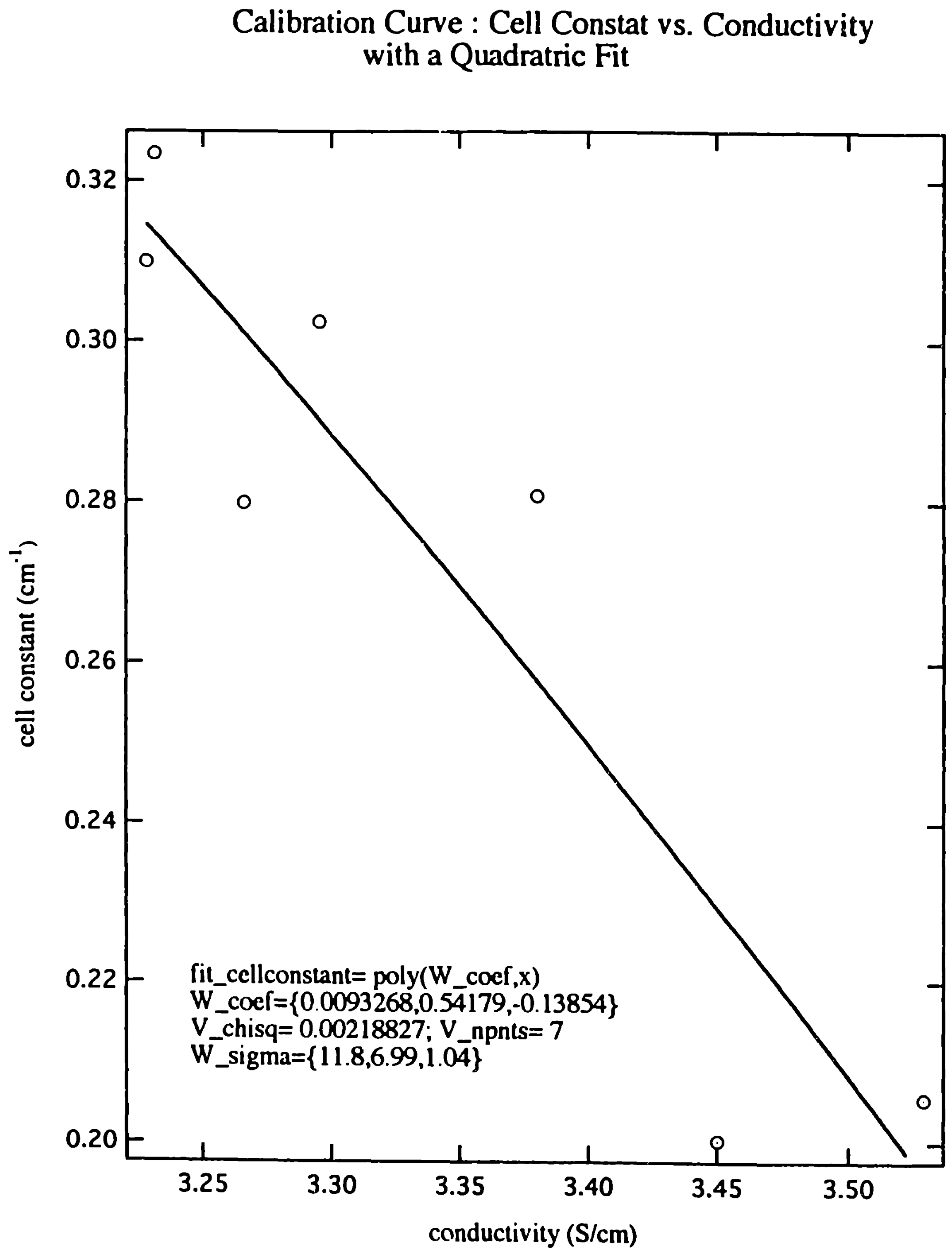

Figure 6.02: Quadratic Fit of Cell Factor vs. Conductivity for the Chloride Calibration Standard

Table 6.1: Transference Numbers for Melts of TiO$_2$-BaO

67:33 TiO$_2$:BaO

T (°C)	Ionic (Field)	Ionic (No Field)	Ionic (Average)	Electronic (Field)	Electronic (1-Iavg)	Total (Iavg+Efield)
1328	0.198	0.198	0.198	0.802	0.802	1.000
1355	0.174	0.181	0.178	0.826	0.822	1.004
1401	0.163	0.170	0.167	0.837	0.833	1.003
1417	0.170	0.157	0.163	0.830	0.837	0.993
1448	0.152	0.146	0.149	0.848	0.851	0.997
1487	0.138	0.138	0.138	0.862	0.862	1.000

73:27 TiO$_2$:Ba0

T (°C)	Ionic (Field)	Ionic (No Field)	Ionic (Average)	Electronic (Field)	Electronic (1-Iavg)	Total (Iavg+Efield)
Frozen						
1210	0.005	0.016	0.011	0.995	0.989	1.005
1268	0.021	0.032	0.026	0.979	0.974	1.005
1323	0.067	0.057	0.062	0.933	0.938	0.995
1354	0.126	0.105	0.115	0.874	0.885	0.990
Transition						
1400(s1)	0.201	0.182	0.192	0.799	0.808	0.990
1400 (s2)	0.216	0.173	0.194	0.784	0.806	0.978
Liquid						
1402	0.119	0.093	0.106	0.881	0.894	0.987
1419	0.139	0.127	0.133	0.861	0.867	0.994
1444	0.114	0.103	0.109	0.886	0.891	0.995
1477	0.096	0.090	0.093	0.904	0.907	0.997

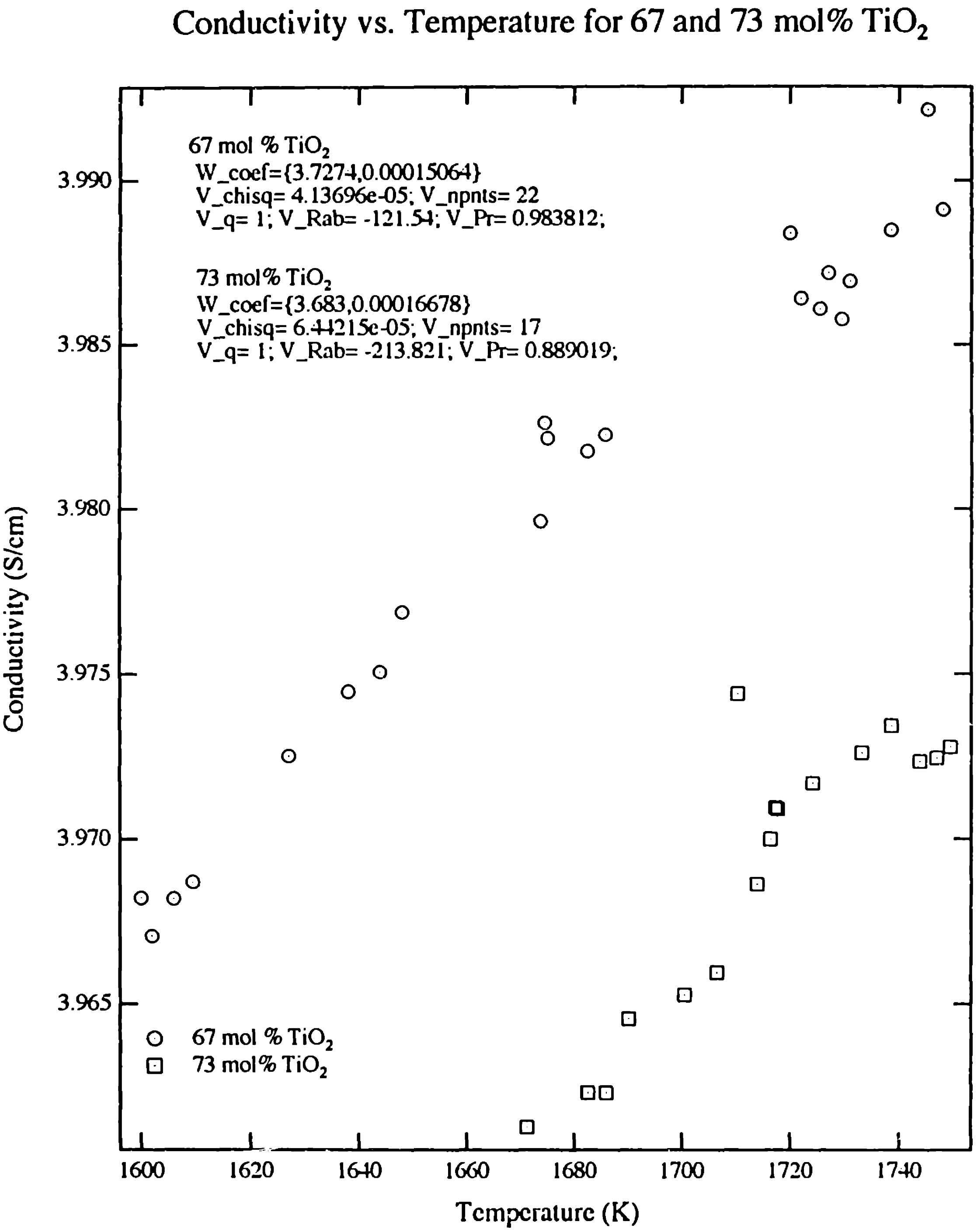

Figure 6.03: Conductivity as a Function of Temperature for TiO_2-BaO

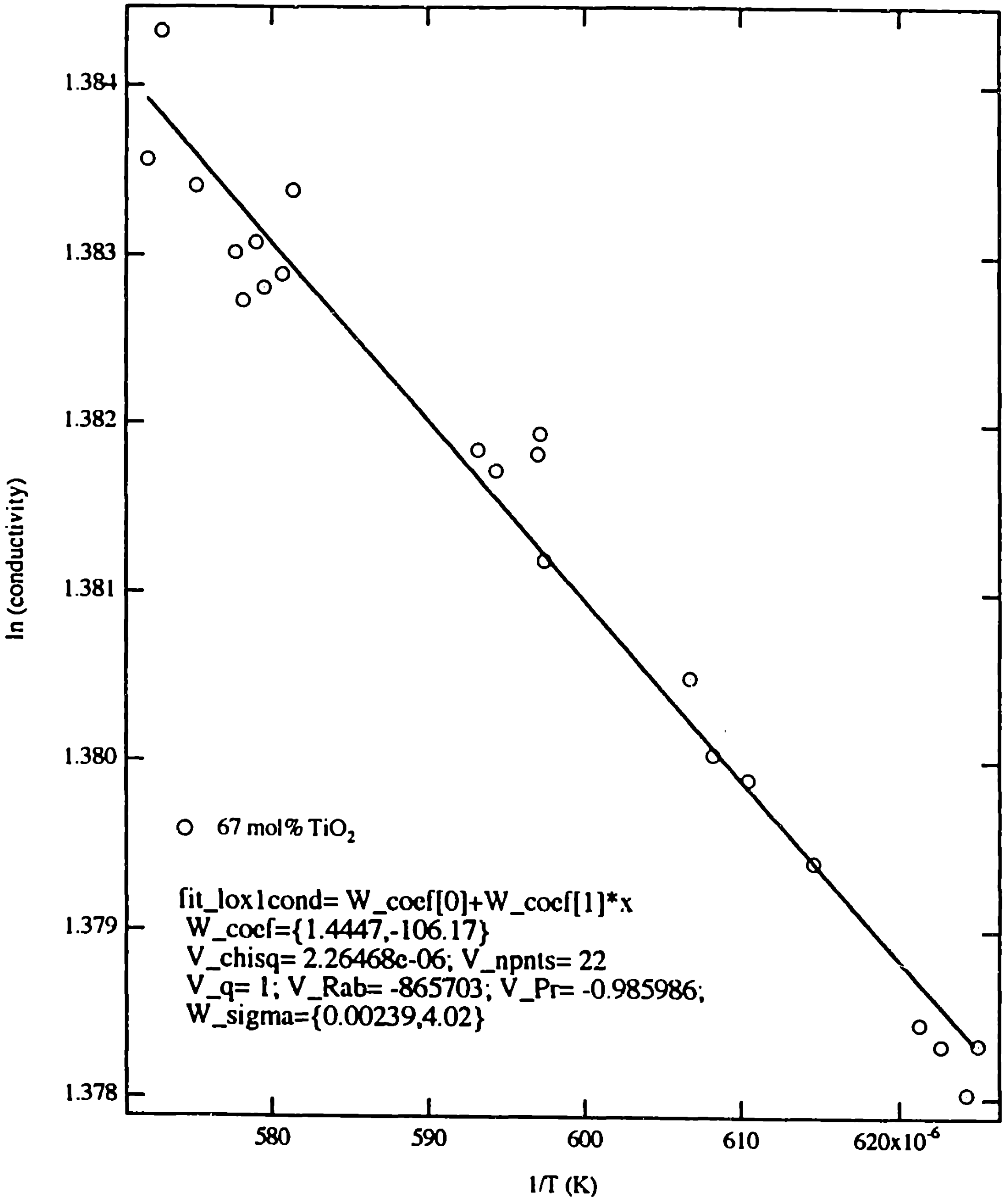

```
fit_lox1cond= W_coef[0]+W_coef[1]*x
 W_coef={1.4447,-106.17}
 V_chisq= 2.26468e-06; V_npnts= 22
 V_q= 1; V_Rab= -865703; V_Pr= -0.985986;
 W_sigma={0.00239,4.02}
```

Figure 6.04: ln(σ) vs. 1/T for 67 mol% TiO$_2$

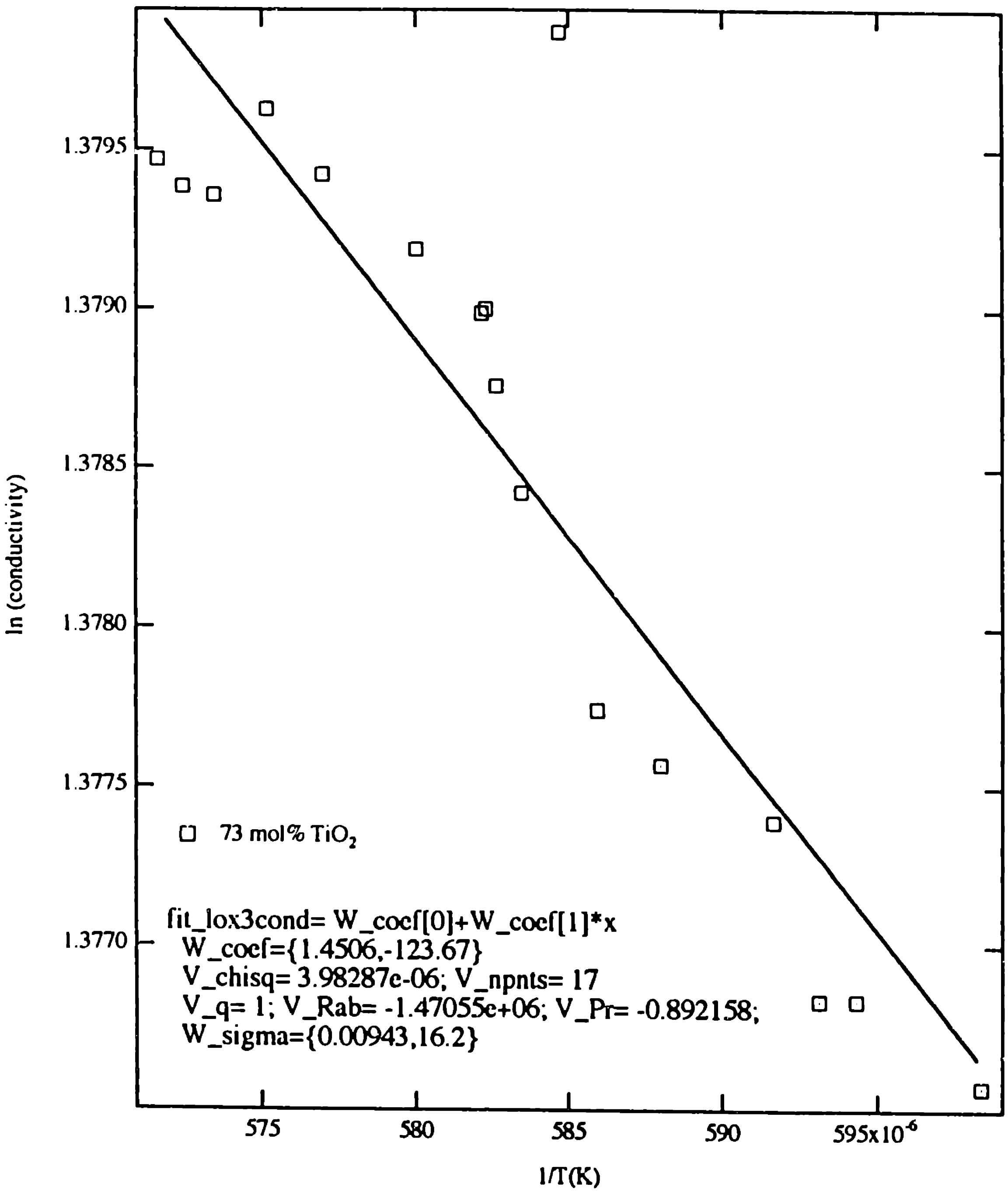

Figure 6.05: ln(σ) vs. 1/T for 73 mol% TiO_2

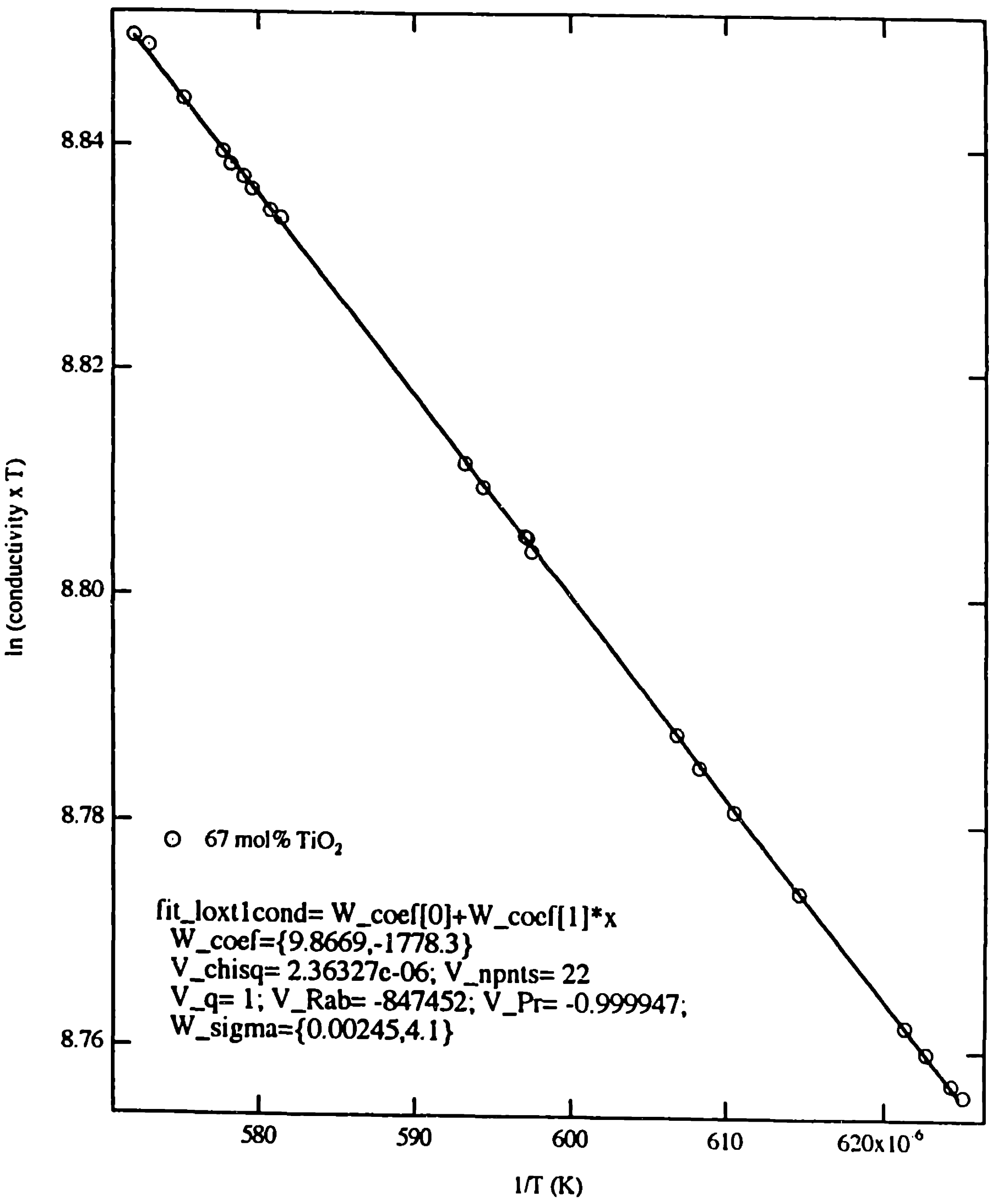

Figure 6.06: ln(σ•T) vs. 1/T for 67 mol% TiO_2

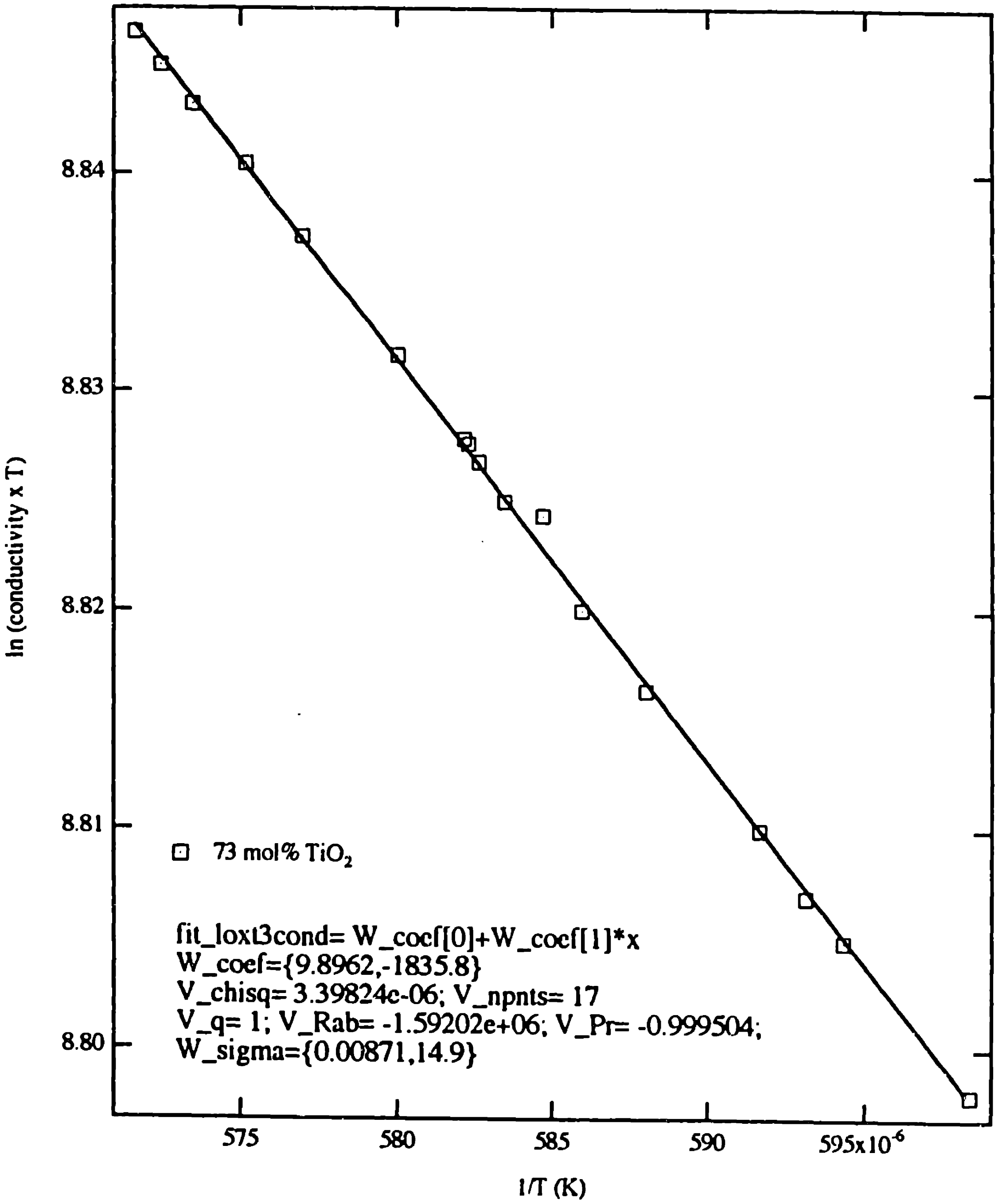

```
fit_loxt3cond= W_coef[0]+W_coef[1]*x
W_coef={9.8962,-1835.8}
V_chisq= 3.39824e-06; V_npnts= 17
V_q= 1; V_Rab= -1.59202e+06; V_Pr= -0.999504;
W_sigma={0.00871,14.9}
```

Figure 6.07: ln(σ•T) vs. 1/T for 73 mol% TiO_2

Conductivity vs. Temperature Above and Below the Melting Point
73 mol% TiO_2

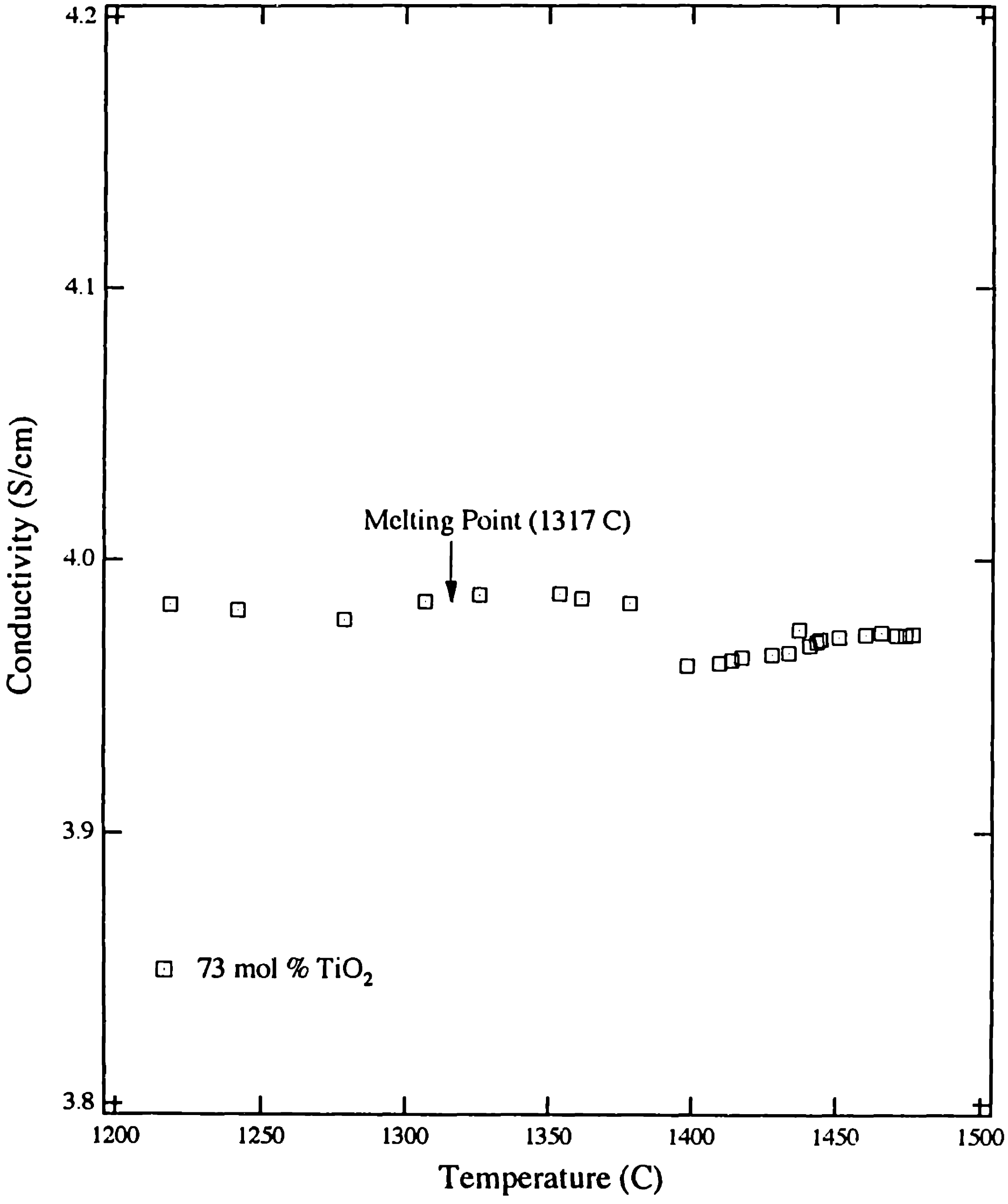

Figure 6.08: Conductivity as a Function of Temperature Above and Below the Melting Point for 73 mol% TiO_2

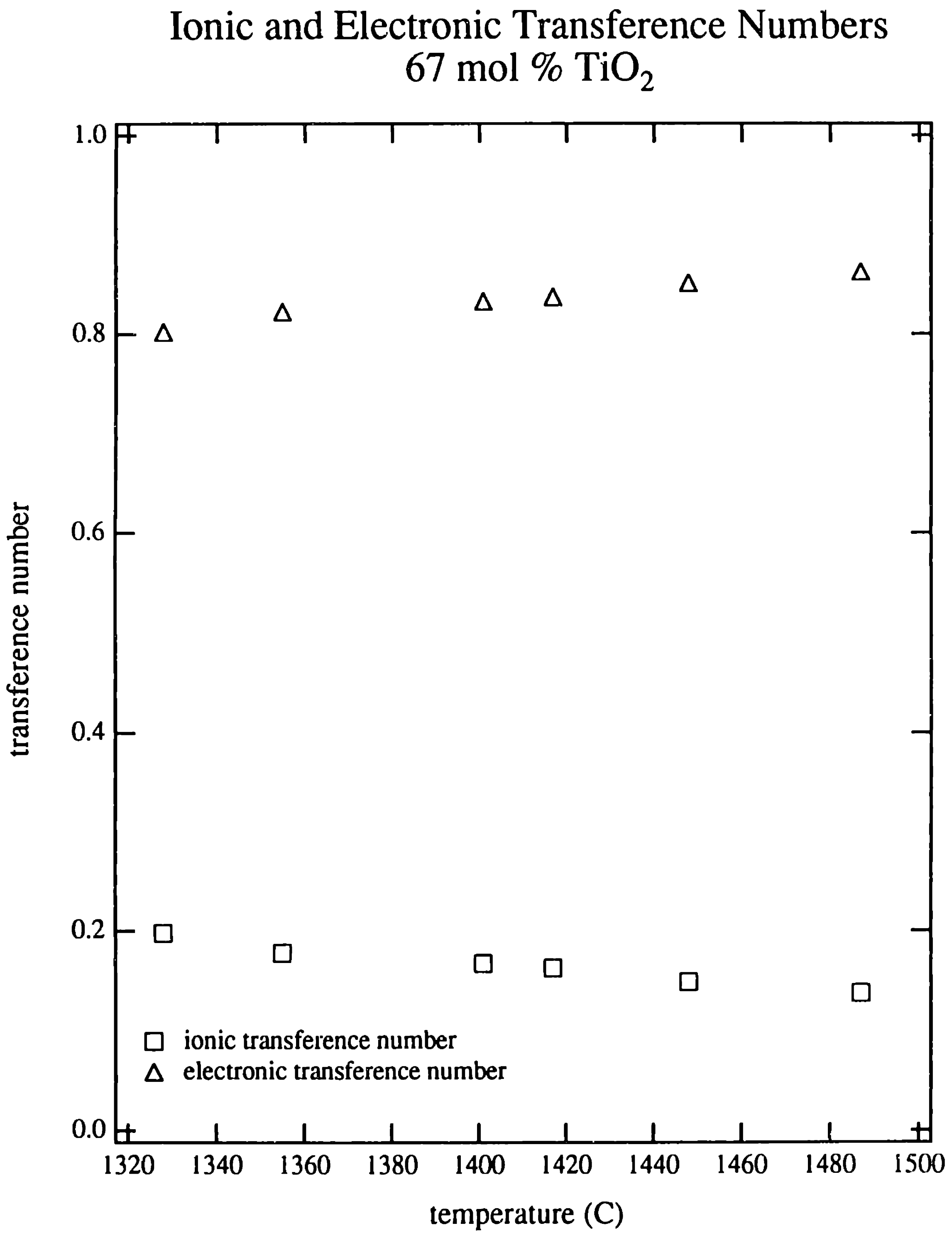

Figure 6.09: Electronic and Ionic Transference Numbers as a Function of Temperature

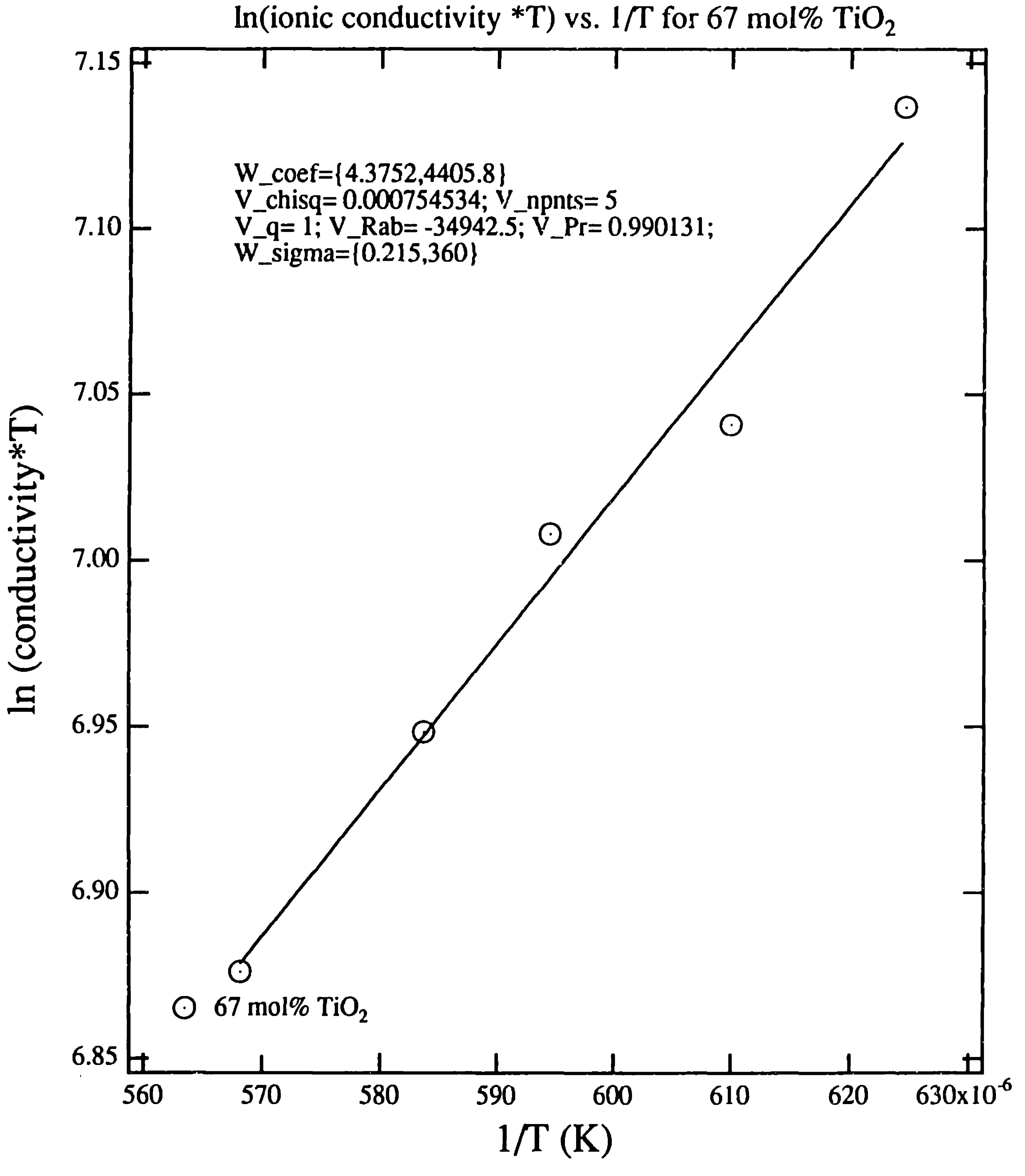

Figure 6.10: Ionic Conductivity as a Function of Temperature

Table 6.2: Resistance Values Calculated From the Triangle Wave and the Square Wave ($t=0^+$)

	Excitation Signal			
	Triangle Wave			**Square Wave**
Temperature	Resistance	Conductivity	Conductivity	Resistance
		67 mol% TiO_2		
1448	0.0045	3.9939	3.9884	0.0049
1401	0.0053	3.9826	3.9826	0.0056
1328	0.0065	3.9682	3.9682	0.0065
		73 mol% TiO_2		
1400	0.0071	3.9613	3.9613	0.0080
1444	0.0061	3.9709	3.9709	0.0067
1477	0.0060	3.9728	3.9727	0.0069
1402	0.0050	3.9819	3.9819	0.0058

Chapter 7: The Direction of Future Work

This chapter discusses ways in which the investigation of molten TiO_2 and the measurement techniques can be continued and expanded. There is also a discussion of the potential for the future extraction of titanium by molten oxide electrolysis.

7.1 Further Study of the Measurement Techniques

7.1.1 Coaxial-Cylinders Electrode Technique

Using the theory and methodology developed for the high accuracy four-point crucible cell, the applicability of the coaxial-cylinders electrode technique could be extended. The range of solutions in which the CCE technique could be deployed could be greatly broadened if the cell were calibrated with a solution of conductivity that matched or bracketed the conductivity of the test medium. However, because the CCE technique would require using calibration standards in these ranges, it would eliminate one of the advantages of this design, namely, a cell factor based on geometry[106].

7.1.2 Four-Point Crucible Technique with Matched Calibration Standards

It would be useful to confirm the accuracy of the four-point crucible technique over a wider conductivity range through the use of other standard solutions. In particular, it would be helpful to determine if the conductivity/cell-factor relationship established for the range of conductivities considered in this investigation is maintained over an even broader span of conductivities, or if there are conductivity extremes at which the relationship between conductivity and cell constant cannot be successfully modelled. It is expected that the limiting factor in the use of the four-point cell will not be the cell

---

[106] When a cell based on the CCE had been built but the test medium was subsequently found to exhibit a conductivity outside the range that the geometric cell-factor could be reliably used, this extension of the CCE technique with matched calibration standards would be useful.

itself, but rather the inability of electrical equipment to measure accurately very high and very low resistances.

It would also be worthwhile to develop a model for the electric field in the four-point crucible cell. In particular, understanding the effect of calculating conductivity with a cell factor that is too high or too low would assist in interpreting work in the literature. There are many reports of conductivity in which a crucible cell has been used with a calibration standard differing from the conductivity of the test specimen.

7.1.3 The Diffusion-Drift Model for the Square Wave Current Decay Technique

The derivation of the current response to the application of a square wave for mixed conductors in the transient regime would complete the drift-diffusion model presented in this work.

Furthermore, an examination of all three time regimes for a finite-length center and crucible electrodes would be interesting. This model could be developed by examining one region in which the center and crucible electrodes are present and another in which only the cylinder electrode is present. The boundary conditions between these two regions would have to be matched and the solutions properly combined.

7.2 Continuing the Investigation of Molten TiO_2

7.2.1 Higher Temperatures

The composition range over which TiO_2-BaO is liquid increases with temperature. For example, a composition of 40-50 mol% TiO_2 melts at approximately 1700°C. The ability to reach higher temperatures would enable researchers to study a wider range of compositions to determine if alternate conduction modes occur in this system. In the vicinity of 1700°C, binary mixtures of silica and titanium dioxide could also be investigated.

7.2.2 Silicate Melts Containing TiO_2

A high silica mixture could be used to test the electron hopping theory of conduction. The electron hopping model proposed in this work requires that the concentration of TiO_2 be high enough to allow easy hopping from one ion to a neighboring ion. An experiment in which TiO_2 is diluted in SiO_2 could be used to confirm or disprove the polaron hopping model.

7.2.3 Variations in Oxygen Partial Pressure

A study of these melts as a function of partial pressure of oxygen would help confirm the semiconduction mechanism. The electrical conductivity of classical semiconductors show a dependence on partial pressure of oxygen: this relationship could be used to ascertain the validity of classical semiconduction. Since the use of tungsten or molybdenum (both refractory metals) limits the range of oxygen pressure in the system, an all-platinum cell would have to be employed.

7.2.4 Raman Spectroscopy

The use of Raman spectroscopy to study the molecular nature of these complexes is another area for future research. The study of the molecular structure could be used to confirm the proposed conduction mechanism.

7.2.5 Confirmation and Extension of Transference Number Measurements

Electrolysis trials on melts of TiO_2-BaO would verify the relative ionic and electronic transference numbers. The effect of the substitution of barium chloride for barium oxide in the melts investigated could help explain if the ionic carrier in these melts is barium or oxygen.

7.3 Engineering Extensions

Although this research has shown that conductivity in the melt is partially ionic, the transference numbers suggest that an industrial process using 67-73 mol% TiO_2 and BaO would have a current efficiency of at most 10-20%, limiting its feasibility. Financial viability of this process requires a suitable supporting electrolyte with higher ionic transference numbers than those measured in this work. If the electronic conduction occurs strictly by a hopping mechanism, dilute solutions of TiO_2 in an ionic electrolyte such as high content BaO could be a suitable system. To maintain thermal and electrical stability in industrial electrolytes, a high concentration of supporting electrolyte is required. The ability to achieve higher temperatures would facilitate research on the suitability of a compositions of this type for molten oxide electrolysis.

The TiO_2-Li_2O binary is an additional candidate electrolyte worthy of study. Although it is difficult to find laboratory materials to contain lithium oxide, in an industrial cell the "frozen" melt could function as the cell's sidewall and eliminate problems of melt containment.

Additives that lower the melting point and increase ionicity could also be considered. Because the Hall-Heroult cell for aluminum extraction uses a mixed oxide-fluoride bath, basic research on the thermodynamics and electrical properties of a titanium oxide melt with small amounts of fluoride compounds would be of interest.

Following the identification of the optimal supporting electrolyte and suitable electrodes, electrolysis trials could begin.

Appendix A: Experimental Protocol and Data Analysis Procedure for the Coaxial-Cylinders Electrode Technique

The procedure described here was used to measure the electrical conductivity of molten TiO_2-BaO. The same general experimental protocol was followed when measuring the electrical conductivity of the calibration standard, molten potassium chloride, to determine the cell constant of the electrodes.

A.1 Melt Preparation, Apparatus, and Atmosphere Control

The titanate melts were prepared by mixing powders of the appropriate proportions in a dry box as described in Chapter 5. A six inch flat bottom molybdenum crucible was charged with the powder and lowered carefully into the alumina reactor tube. The compression fitting built out of a "Kwik disconnect cap,"[107] which sealed the reactor tube to the PMZ bellows apparatus,[108] was also placed on the reactor tube. The PMZ bellows device was then attached to the top of the Kwik disconnect cap. Finally, the top flange of the PMZ in which the electrodes and thermocouple had been mounted was bolted to the top of the PMZ (See Figure A.01). All compression fittings, bolts and nuts, and gas valves on the PMZ were closed and hand-tightened.

The reactor tube, containing the charged crucible and mounted to the PMZ, was removed from the glove box. A strap-wrench was used to further tighten the Kwik disconnect cap around the reactor tube and vice-grips were used to tighten the Ultra-torr fittings that held the electrodes and thermocouple in place on the top flange of the PMZ.. The gas inlet and outlet ports were attached to the gas flow manifold and the vacuum

---

[107] MDC Vacuum Products Corporation, Hayward, CA.

[108] The bellows, purchased from Huntington, part #PMZ-275-6, were customize with a 2" inner diameter. A Mitotoyo digital height-gauge, part #572-311, from Harbour Tools, Westwood, MA was mounted on the bellows.

manifold using red rubber tubing. The gaseous atmosphere in the reactor tube was controlled as described in Chapter 5.

A.2 Electrochemical Impedance Spectroscopy Apparatus

A Schlumberger Solartron 1260 Gain/Phase Analyzer was used to generate and process the alternating current excitation signal. Four, five-foot long BNC cables were used to carry the signal from the 1260 Gain/Phase Generator to the electrodes. The ports on the 1260 were labeled "generator output," "input," "V1 high," and "V1 low" (See Figure A.02). Prior to attaching the electrodes, the inner lead of the BNC cable from the "generator" port was electrically tied to the inner lead of V1 High, which measures the voltage before the signal was applied to the cell. Similarly, before connection with the electrodes, the inner lead of the BNC cable from the 1260 "input" port was tied to the inner lead of V1 Low, which measures the voltage after it passes through the test cell. See Figure A.02). The outer shields of all four BNC cables were tied together near the cell to provide a common ground. The inner leads of the generator and current BNC cables were mounted into banana plugs which fit snugly into receptacles on the leads at the top of the inner and outer cylindrical electrodes. The BNC cables were held securely in place by braiding them and placing them under hosecocks mounted to the wooden cabinet encasing the 1260. The secured cabling ensured that the inductive contribution to the measured impedance remained constant.

An IBM AT and the Z60 impedance program[109] were used in data acquisition, storage and analysis. With the aid of an IEEE GPIB bus, the computer was able to receive and display the impedance data as they were collected by the 1260. The experimental electrical parameters were set within menus of the Z60 program.

---

[109] Scribner Associates, Charlottesville, VA.

A.3 Experimental Electrical Parameters

When setting the experimental parameters of the 1260, it is important to understand how the instrument is constructed. In particular, there is a 50-Ω output impedance built into the 1260 that appears in series with the specimen under test for the configuration shown in Figure A.02. This is done to provide impedance matching with the 50 Ω RG-58 BNC cables and thus reduce reflections at high frequencies. Because this output impedance functions as a voltage divider, when measuring very small impedances, it is necessary to set the 1260 to generate a much higher voltage than is actually dropped across the test specimen. For example, when a 1-Ω specimen in series with the 50-Ω output impedance is measured, only 1/50th of the output voltage appears across the specimen. The lower the impedance of the specimen, the lower the voltage dropped across it. The lowest range of voltage measured by the 1260 is 30 mV and full accuracy occurs only for measurements in excess of 10% of this value, or 3 mV. For smaller voltages, the instrument gives a less accurate reading and errors would become more significant as the signal decreases. Also, the measurement signal-to-noise ratio decreases at small signal levels. Therefore, measurements at the highest voltage output level possible are preferred. For very small impedances the maximum applied voltage (3 volts) on the 1260 will achieve only millivolts across the test specimen. Alternatively, the 1260 can be run in current control mode but even in current control mode it cannot produce more than 3 V. For low-impedance measurements, a large excitation current is recommended.

In a typical conductivity experiment, an AC excitation signal of 60 milliamps with no DC bias is applied to the system under test. In current control mode, a log frequency sweep of 100 points per decade over the range of 1 MHz to 100 kHz, followed by a second log sweep of 25 points per decade for the interval 100 kHz to 1 kHz, was used. Neither the monitor function of the Z60 program nor the auto-integration capability of the 1260 was employed. The 1260 was programmed to collect data for 0.5 seconds at each frequency. No null file was indicated when the data was collected. The short-circuit null correction was applied to the data during the data processing phase.[110]

The Z60 program instructs the 1260 to float the outer shields in order to prevent a second grounding in addition to the one physically created by tying together the outer shields of the four BNC cables. If the Z60 program is instructed to ground the outer conductors, it will provide a second ground for the lead wires. Since there is current flowing through the generator, it is possible that this ground would be at a higher potential than the ground provided by the analyzer and undesirable ground loops could result.

The source of the impedance was calculated from the ratio, "V1/I," that is, the voltage measured by the 1260 divided by the current. Generally, all the parameters were stored as a batch file. The 1260 ran the entire batch and saved the data to the file names provided.

A.4 Physical Experimental Parameters

Once the electrodes were immersed approximately one centimeter into the melt, the position was noted with the height gage. That height was designated "position 1" with a relative height of 0 mm. All subsequent measurements of the conductivity at that temperature were referenced to this height.

The temperature at position 1 was noted as the conductivity data was collected. At the end of the conductivity measurement for position 1, the temperature was again measured to assure that the thermal fluctuation during the measurement was less than two degrees. Once a successful measurement at position 1 had been made, the electrodes were lowered 1-2 mm and a new position, "position 2," was established. The height of

---

[110] See Appendix A.5.3. for more detail.

the new location relative to the reference, position 1, was recorded. Again, the temperature on the thermocouple was read to ensure that it was within two degrees celsius of the temperature established for position 1 before conductivity data was collected at this depth. Following the successful measurement at position 2, the process was repeated for positions 3, 4, 5, and 6. All six measurements were made within two degrees of a common temperature. At the completion of the sixth position, the electrode was raised from the melt.

The next temperature was 50 celsius degrees higher than the initial temperature, the third temperature was 100 degrees higher than the initial, the fourth was 75 degrees higher, the fifth, 25 degrees higher, and the sixth and final temperature was 25 degrees cooler than the initial temperature. Each sample was measured six times at each of six different temperatures ranging over 125 degrees in 25-degree intervals.

When the conductivity data for the final temperature had been collected, the electrode and thermocouple were raised a final time and the temperature was raised 50 degrees and held for 30 minutes to allow the melt to drip off. The furnace was turned off and the melt was allowed to cool to room temperature under flowing argon.

A.5 Data Analysis Procedure

A.5.1 Overview

In EIS measurements, the solution resistance is not measured in isolation. Any raw measurement of the solution resistance contains the solution reactance (frequency-dependent impedance) as well as resistances and reactances associated with the electrodes and leads. To sort out the many components of a complex impedance measurement, it is necessary to rely on an equivalent electrical circuit model. Using this model, experimental techniques and data analysis procedures are developed to isolate the solution resistance. The following sections will systematically describe how the data from the complex impedance measurement was used to generate the information needed to calculate the solution resistance and the conductivity.

A.5.2 Equivalent Electrical Circuit Model

To derive the appropriate measurement techniques and data analysis procedures for the accurate calculation of solution resistance from the total impedance reported by the 1260 gain/phase analyzer, an equivalent electrical circuit was used. Without this model, appropriate data analysis could not be attempted.

An "equivalent circuit" model represents the components of the measured system in an electric circuit through which the AC excitation signal from the 1260 gain/phase analyzer travels as simple, lumped electrical elements such as resistors, capacitors, and inductors. For example, the lead wires from the 1260 to the coaxial-cylinders electrode were modelled by a resistor and inductor in series. The interface between the electrode and the solution under test, referred to as the double-layer capacitance, can be represented by a capacitor. The solution itself was best modelled by several elements in parallel: a solution resistance (which itself had radial and non-radial components) and a bulk capacitor. See Figure 2.04.

A.5.3 Null Measurements

The first step toward isolating the solution impedance, Z_{sol}, from the total measured impedance, Z_{tot}, was to remove the lead wire impedance, Z_{lead}. For a fixed frequency, these impedances were related by equation (A.1):

$$Z_{tot} = Z_{sol} + Z_{lead} \qquad (A.1)$$

Once Z_{lead}, modelled by a resistor and inductor in series, was known, it was subtracted from Z_{tot} to give Z_{sol}. To evaluate the lead wire impedance, a null measurement was carried out.

The lead wire impedance was found during the null experiment by measuring the total impedance when no solution was present between the electrodes over the same frequency range. To measure electrode resistance and induction, a shorting bar of solid silver (for temperatures below 900°C) or liquid silver (for temperatures above 1200°C) was inserted between the electrodes to complete the electrical circuit between the inner and outer electrodes. Silver was the metal of choice as it forms no solid solutions or liquid alloys with the molybdenum used to construct the electrodes.[111] Silver is highly conductive, and added negligible resistance to the measurement of the lead wire impedance. This data set, known as a short circuit null measurement, was stored and subsequently subtracted from the total impedance.

A series of null measurements were taken over the temperature interval of interest. For example, for conductivity measurements on molten sodium chloride and potassium chloride, null data was collected on the interval, 775°C to 925°C. The electrode and lead were configured as they would be for conductivity measurements on the molten salts, and the shorting bar was inserted. The null measurements were done using the same electrical parameters used in the collection of the actual conductivity data.

Once a library of null measurements was established, the program "Inull," written by Dr. Kevin Rhoads, was used to create linear interpolation of null files for intermediate temperatures at which null data was not collected. For example, the library might contain null measurements of the electrodes at 800, 825, 850, 875, and 900°C. If the conductivity

---

[111] While liquid silver is immiscible with molybdenum, it was necessary to remove excess sliver from the surface of the molybdenum electrode after the shorting measurement. After a review of the literature, it was found that HI (hydriotic acid) was capable of dissolving the silver without attacking the molybdenum.

of molten sodium chloride was measured at 857°C, the null measurements of the two closest temperatures (850 and 875°C) available from the null library were used to create a null file for 857°C. The Inull program created the interpolated null file by using a linear weighting of the two end-point temperatures. Once a null file for 857°C was created, the Inull program proceeded to subtract the impedance of the electrodes and leads in the null file from the total impedance of the sodium chloride at each frequency. Since simple subtraction of impedances can only be done when the frequencies are matched, it was essential that the null measurement and the conductivity measurement be collected at the same frequencies.

In addition, it was critical that the configuration of the electrodes used during the collection of null data be identical to the configuration of the electrodes during the actual conductivity measurements. Varying the spacing between the cables attached to the lead results in changes in lead wire inductance. Care must also be taken that the lead wire resistance not be changed by faulty, or intermittent, contacts between any of the electrical junctions through which the excitation signal passes. Any change in the configuration that results in a variation in the lead wire impedance would make the short circuit null measurement useless in isolating the solution impedance from the total measured impedance.

A.5.4 Separation of Reactances from Resistances

Once the raw impedance data was nulled using the short circuit null measurement, only the impedance of the solution remained. The next step in the data analysis procedure was to isolate the solution resistance from the two capacitances. Since capacitance is frequency-dependent while resistance is frequency-independent, the ability to vary the frequency of the overall impedance measurement was exploited to separate the resistance from the capacitance.

The three remaining impedances were modelled as follows. The solution resistance and capacitance, acting in parallel to each other, were in series with the double-layer capacitance (see the equivalent circuit model in Figure 2.04). Plotting these impedances in the complex plane, where the real component of the impedance was represented by the x-coordinate while the imaginary component of the impedance was represented by the y-coordinate, was helpful in further isolating the solution resistance. A plot in the complex plane of an ideal resistor and capacitor, in parallel with each other and in series with a capacitor, is shown in Figure A.04. From this figure, the value of the resistance in this equivalent circuit model can be directly found from the intersection of the plot with the x-axis where the impedance was frequency independent.

A typical plot of actual impedance data, after nulling, is shown in Figure A.05. The shape of the solution impedance was very similar to the ideal plot in Figure A.04. The circuit resistance in the ideal plot was found from the intersection of the plot with the x-axis. Similarly, though the plot of the actual data does not touch the x-axis, the impedance at the point of closest approach to the x-axis can be taken to represent the solution resistance. The impedance at this point was composed almost entirely of resistance and the value of the frequency dependent capacitances was approximately zero.

The value of the solution resistance was found by examining the real component of the impedance when the imaginary component was at a minimum. The computer program, Minnull, written by Dr. Kevin Rhoads, scanned all the values of the impedance from a file containing nulled data and presented the impedance with the smallest imaginary component, displaying the real and imaginary components, as well as the frequency. The real component at this frequency was then accepted as the value of the solution resistance.

A.5.5 Separation of Radial and Fringe Solution Resistances

The solution resistance isolated using the Minnull program is composed of two parts. The first part is called the radial solution resistance because it arose from the resistance of the solution between the electrodes. The second component is the fringe solution resistance. The fringe solution resistance reflects the measured resistance of solution beyond the bottom of the electrode, in the fringing field and at the free surface of the liquid. See Figure A.06.

Only the radial solution resistance is used to calculate the solution conductivity. Fortunately, once the electrode is immersed in the solution, the fringe solution resistance is a constant while the radial solution resistance varies with electrode position. In this way, the radial solution resistance is eliminated from the total solution resistance by taking measurements at a variety of positions and then examining the differential solution resistance. This is achieved experimentally by measuring the total impedance at several depths of immersion as described above.

Provided that the conductivity of the electrode is much greater than that of the solution, the non-radial component of the resistance is constant as long as the electrode does not approach the bottom of the crucible too closely. Experiments have shown that a distance of twice the difference in radii of the coaxial-cylinders electrode is adequate to assure that the fringing field is not disturbed and the fringe solution resistance remains constant.

A plot of solution resistance (R_{sol}) versus depth of immersion (l) was created for each temperature. A correction factor is applied to the measured depth to reflect the rise in the melt level due to the immersion of the electrode into the melt. The slope from this plot, $d(1/R_{sol})/d(l)$, is then used in equation (A.2) with an expression for the differential cell constant, $\{d(l/G)/d(l)\}$, calculated from the calibration procedure to yield the solution conductivity, κ.

$$\kappa = \{d(1/R_{sol})/d(l)\} \; / \; \{d(l/G)/d(l)\} \qquad (A.2)$$

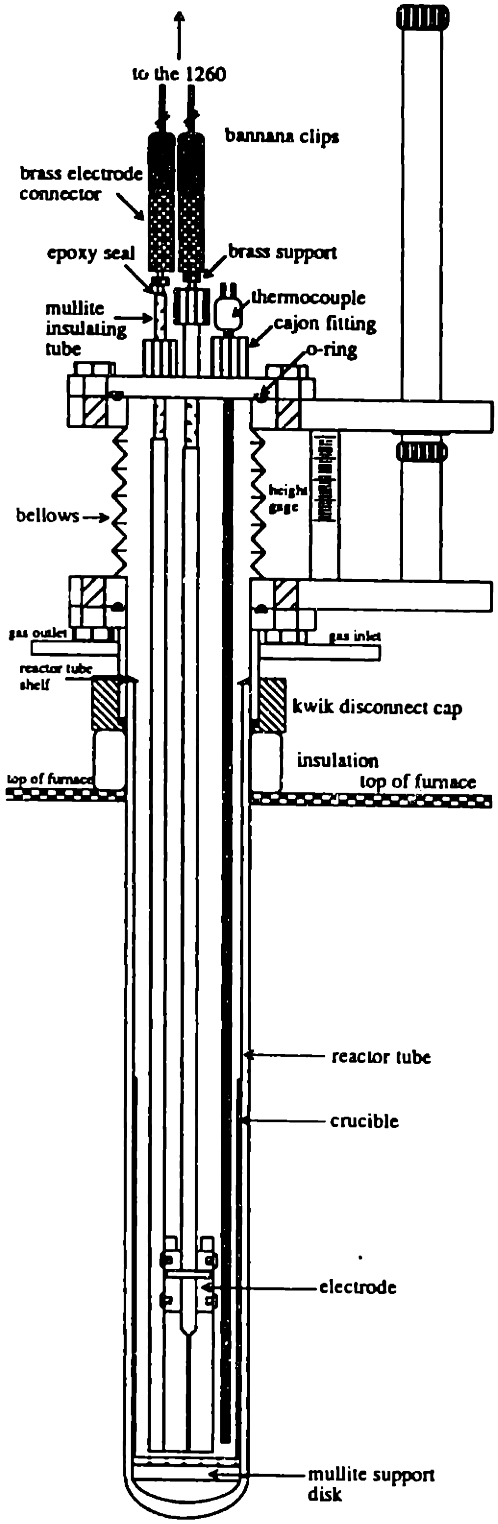

Figure A.01: Conductance cell, Reactor Tube, and PMZ-Bellows Apparatus Used to Measure the Electrical Conductivity with the Coaxial-Cylinders Electrode

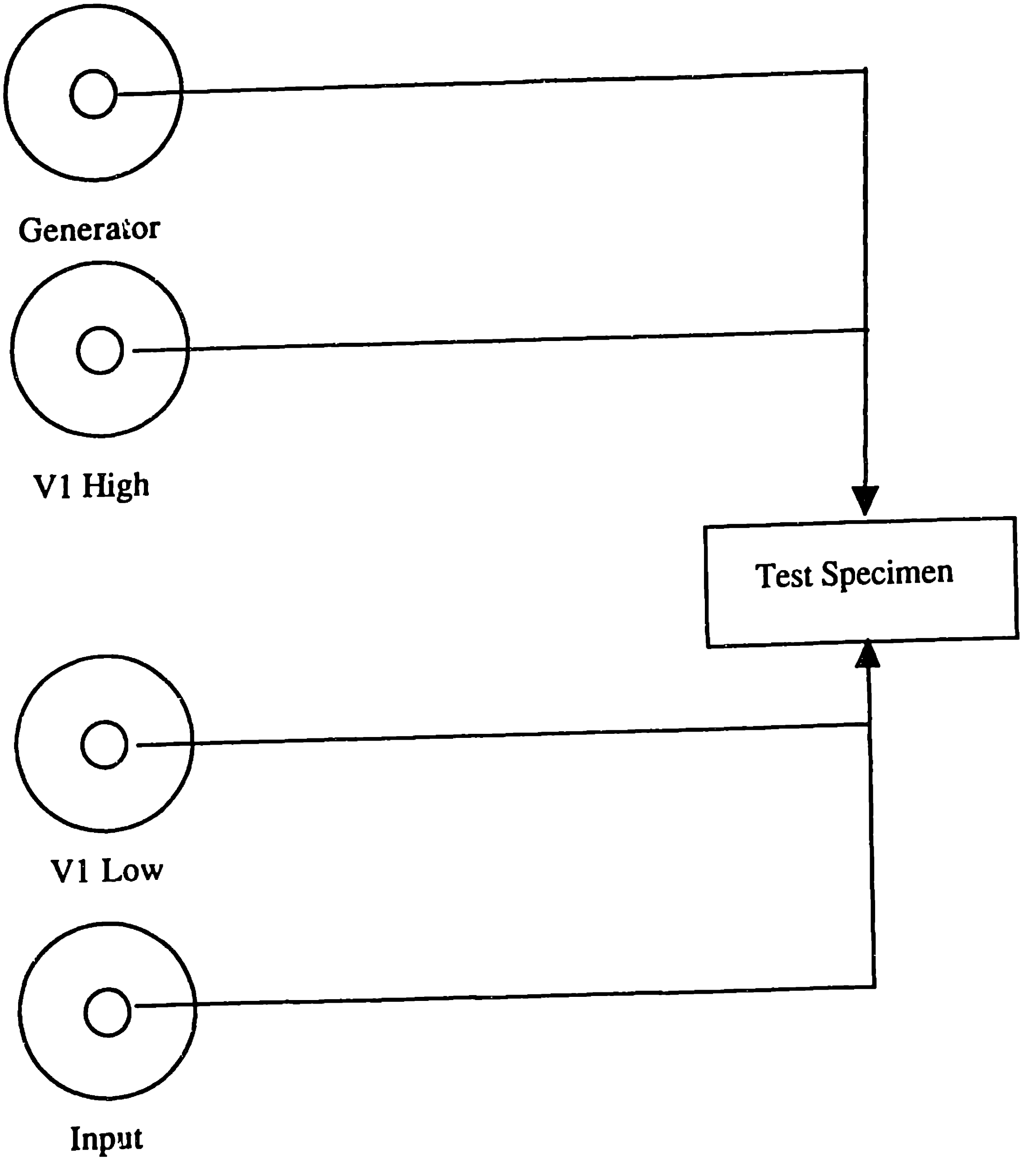

Figure A.02: Load Connection from the 1260 to the Coaxial-Cylinders Electrode

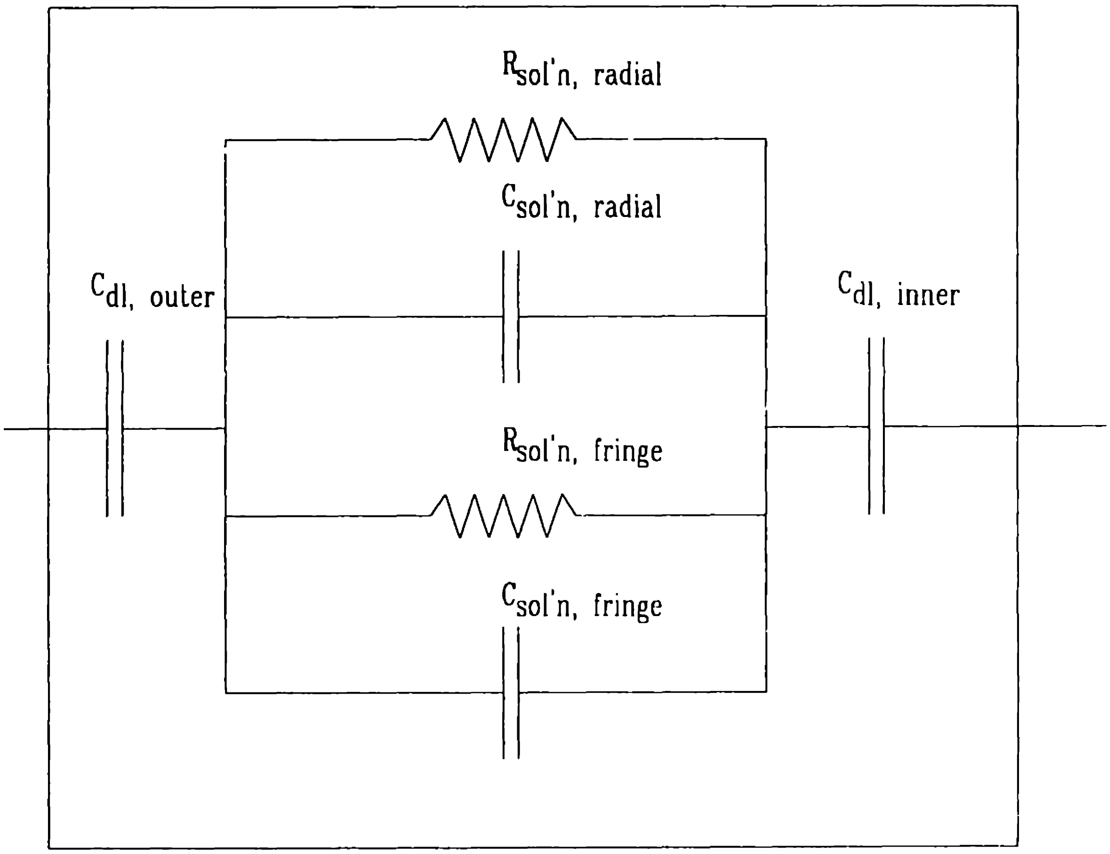

Figure A.03: Solution Model

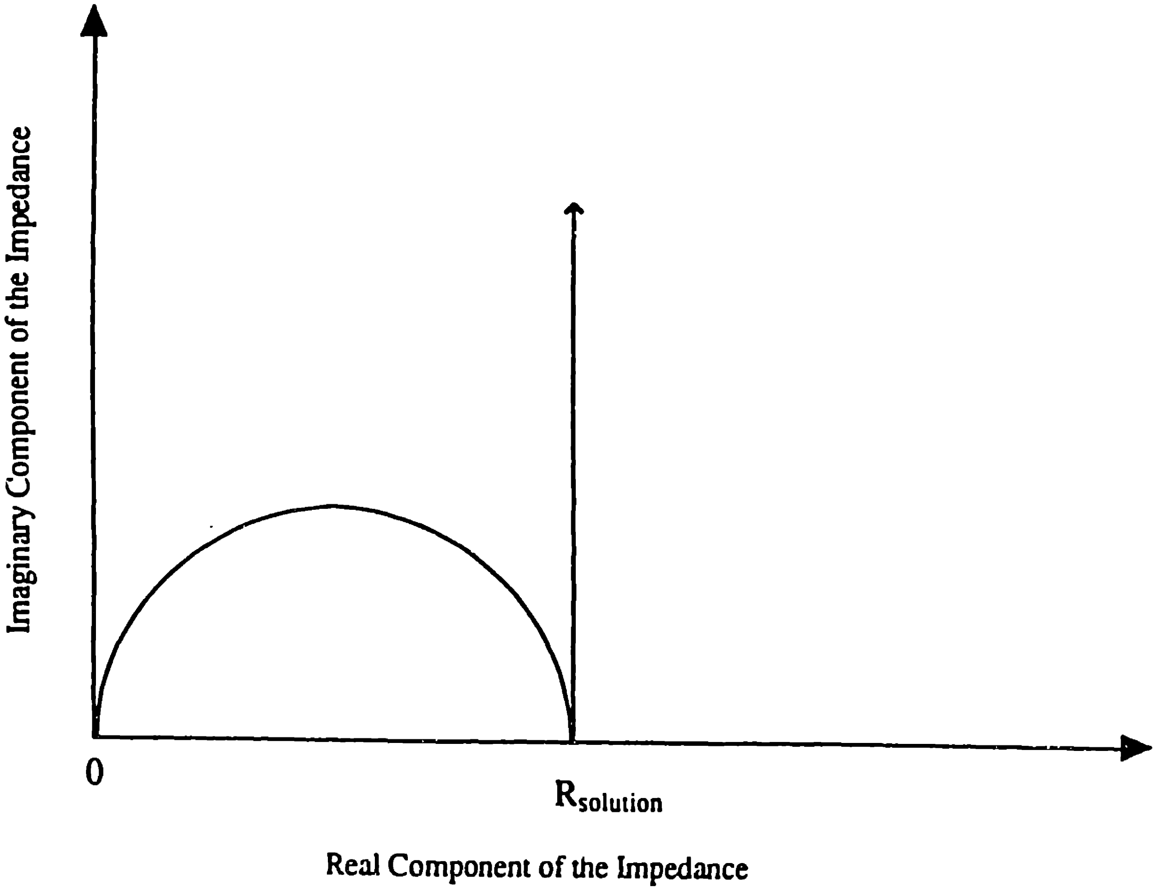

Figure A.04: Idealized Plot in the Complex Plane of a Resistor and Capacitor in Parallel

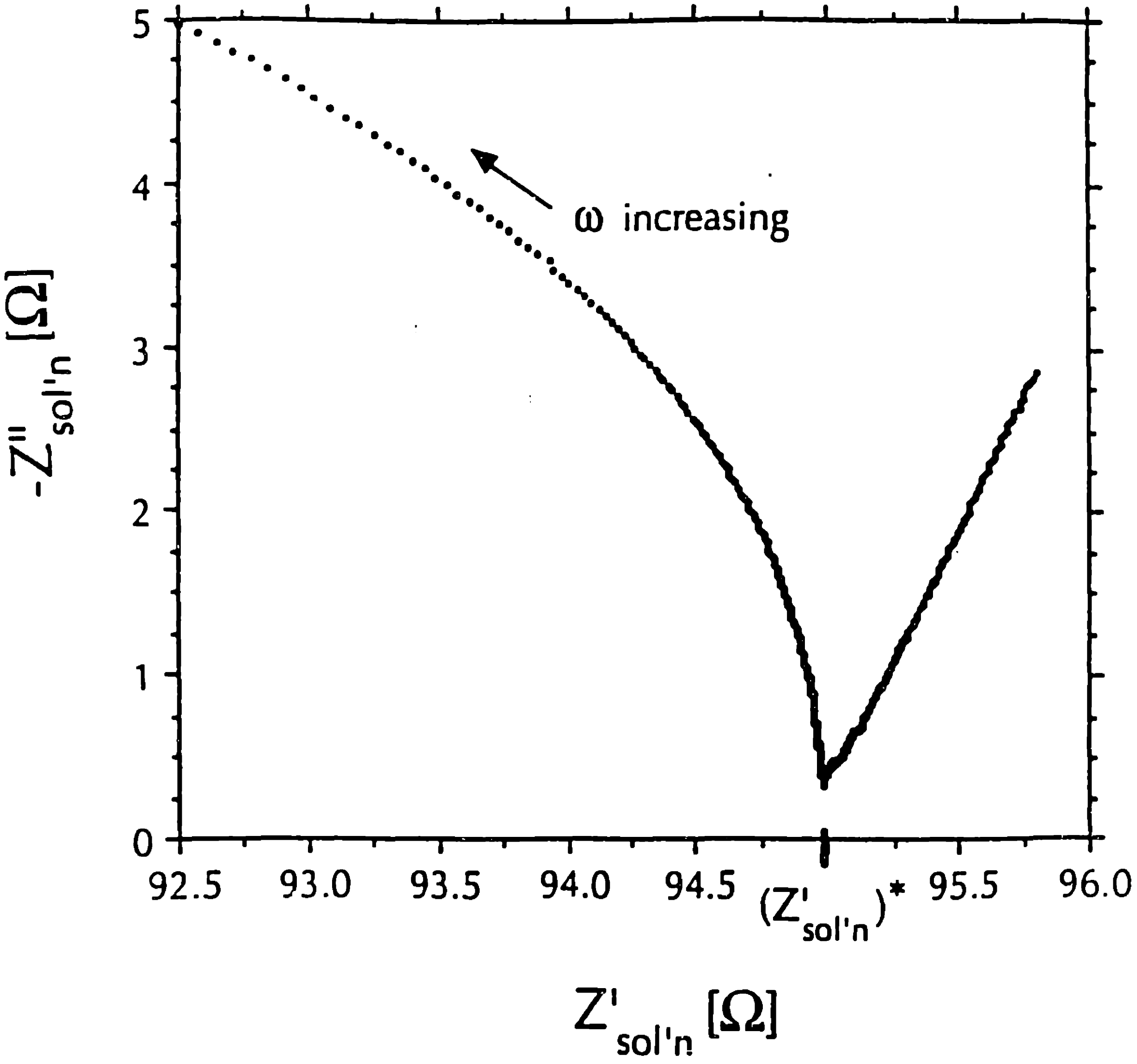

Figure A.05: A Plot in the Complex Plane of the Solution Impedance of 1.0 D KCl

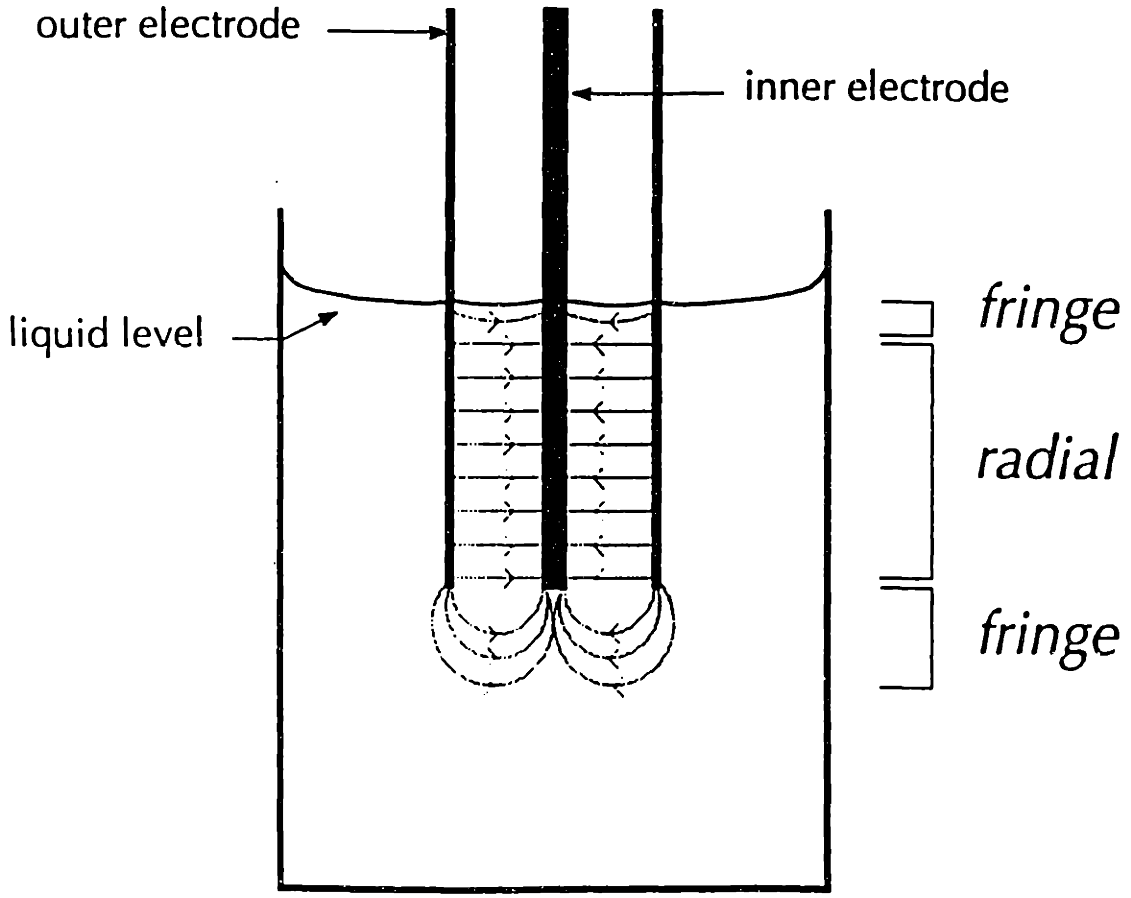

Figure A.06: Coaxial-Cylinders Electrode and Fringing Field

Appendix B: Application and Use of Shrink Tubing

The application of FEP shrink tubing to each of the molybdenum rods was necessary to provide electrical isolation between the metal cap and the current carrying electrodes, and the cap and the voltage measuring electrodes. As a precautionary measure the thermocouple and spacer holder were also insulated from the cap. The shrink tubing had to tightly adhere to the rods to maintain the integrity of the atmosphere in the reactor tube.

The shrink tubing was applied to the rods through a heating process. Depending on the size of a given rod, FEP tubing of an appropriate diameter was cut into a sleeve of specified length (see recipes below.)

Because the rods had to be raised and lowered, it was necessary to provide shrink tubing along the entire travelled length. Because the temperature in the reactor tube increased as the hot zone was approached, longer lengths of shrink tubing experienced higher temperatures. The maximum working temperature for FEP shrink tubing is 400°F, making it necessary to use the minimum length of shrink tubing to accomplish the electrical isolation. Unlike the chloride calibration run where the maximum working temperature was 925°C, melting shrink tubing was of a particular concern in the experiment with oxides in which temperatures approaching 1500°C were used. The shrink tubing recipes were modified to reflect the higher temperatures of the oxide experiments.

To facilitate good adherence of the plastic to the molybdenum rods, the rods were thoroughly cleaned with soapy water, acetone, and distilled water before the application of the polymer. In order to keep the shrink tubing from "slipping" during the experiment, the rods were preheated before application of the shrink tubing which was followed by very slow heating of the shrink tubing on the rod. The rod was held horizontally in front of a stationary heat gun at the maximum possible temperature and slowly rotated and moved horizontally. Great care was taken when applying shrink tubing to rods significantly smaller than the diameter of the shrink tubing. In these cases, the shrink tubing had a tendency to buckle if heated too rapidly.

Shrink Tubing Recipe for the Experiment with Chlorides

To each of the 0.0625" voltage-sensing electrodes was attached 5.375" of AWG 18 1.3:1 FEP shrink tubing attached 10.125" from the bottom of the rod.

To the 0.125" center electrode was attached 6.125" of 0.125 1.6:1 FEP shrink tubing 10" from the bottom of the rod.

To the 0.125" crucible electrode was attached 3" of 0.125 1.6:1 FEP shrink tubing 14" from the bottom. When a 0.118" rod was used, 0.1875 1.6:1 FEP shrink tubing was used instead of the 0.125" material.

To the 0.125" thermocouple was attached 5" of 0.125 1.6:1 FEP shrink tubing 9.625" from the bottom.

To the 0.125" spacer rod was attached 4" of 0.125 1.6:1 FEP shrink tubing 5.5" from the bottom.

Shrink Tubing Recipe for Use in Oxide Experiments

To each of the 0.0625" voltage-sensing electrodes was attached 4" of AWG 18 1.3:1 FEP shrink tubing attached 11.5" from the bottom of the rod.

To the 0.125" center electrode was attached 3" of 0.125 1.6:1 FEP shrink tubing 13.75" from the bottom of the rod.

To the 0.125" crucible electrode was attached 2.5" of 0.125 1.6:1 FEP shrink tubing 1.5" from the top. When a 0.118" rod was used, 0.1875 1.6:1 FEP shrink tubing was used instead of the 0.125" material.

To the 0.125" thermocouple was attached 4" of 0.125 1.6:1 FEP shrink tubing 10.625" from the bottom.

The spacer rod remained unchanged for both experiments.

Appendix C: Calculation of Conductivity-Dependent Cell Factor

Temperature, Resistance, Conductivity, and Cell Factor used to calculate the conductivity dependent cell factor for the crucible style cell with KCl:NaCl 15.23:84.77 mol%.

Temperature* (°C)	Resistance (Ω)	Standard Deviation	Conductivity (Theoretical)	Experimental Cell Factor
880	0.058066	0.0056	3.45015	0.20033
913	0.058262	0.0071	3.52909	0.20561
853	0.083089	0.0036	3.38007	0.28085
822.6	0.091077	0.0064	3.29527	0.30239
812.6	0.085705	0.0087	3.26601	0.27991
801	0.100130	0.0040	3.23122	0.32353
800	0.096007	0.0065	3.22818	0.30993

* The order of temperatures represents the chronological order of data collection.

```
Statistical Evaluation of the Conductivity Dependent Cell Factor

 Kendall reports: probability =    5.088575E-02
                          tau =  -6.190476E-01
                            z =      -1.952442

 Spearman reports: probability rs =    2.344880E-02
                                rs =  -8.214286E-01

 Spearman reports: probability d =   4.421142E-02
                                d =      102.000000
                               zd =        2.012081

 CONFIDENCE LEVEL that there is a correlation:    9.765512E-01

____________________________________________________________________
 QUADRATIC Coefficients are    9.315944E-03    5.417952E-01    -1.385411E-01

 CHI-squared for quadratic fit is     364.517400
 Goodness of Quadratic fit is (Q=)    0.000000E+00

 LINEAR Coefficients are          1.581569   -3.921483E-01
 Std. deviations      are    2.871491E-02    8.592809E-03
 Correlation among linear coefficients is   -9.994798E-01

 Gaussian Linear r =   -9.222168E-01
 CHI-squared for linear fit is    2.198031E-03
 Goodness of Linear fit is (Q=)        1.000000
```

Appendix D: Resistances, Temperatures, and Conductivities for Molten Oxides

67 mol% TiO_2

Temp.* (°C)	Resistance (scaled)	Standard Deviation	Conductivity
1456.5	4.664E-03	1.11E-05	3.9858
1458	4.548E-03	7.23E-06	3.9869
1454	4.524E-03	5.22E-06	3.9872
1465.5	4.393E-03	7.57E-06	3.9885
1475	4.331E-03	4.50E-06	3.9891
1472.2	4.030E-03	7.35E-06	3.9921
1452.5	4.632E-03	8.52E-06	3.9861
1449	4.600E-03	7.66E-06	3.9864
1447	4.403E-03	7.22E-06	3.9884
1412.8	5.014E-03	5.11E-06	3.9822
1409.5	5.063E-03	6.85E-06	3.9817
1402	5.024E-03	3.10E-06	3.9821
1401.5	4.977E-03	9.77E-06	3.9826
1400.8	5.273E-03	1.32E-05	3.9796
1375	5.550E-03	1.67E-05	3.9769
1371	5.731E-03	1.16E-05	3.9751
1365	5.790E-03	1.12E-05	3.9745
1354	5.984E-03	1.31E-05	3.9725
1336.5	6.365E-03	1.16E-05	3.9687
1333	6.418E-03	6.57E-06	3.9682
1329	6.531E-03	1.24E-05	3.9671
1327	6.415E-03	1.46E-05	3.9682

* Values are given in the chronological order they were measured.

73 mol% TiO_2

Temp.* (°C)	Resistance (scaled)	Standard Deviation	Conductivity S/cm
1398.3	7.118E-03	1.27E-05	3.9613
1409.6	7.011E-03	1.38E-05	3.9623
1413.8	6.907E-03	1.18E-05	5.0118
1417.2	6.786E-03	1.30E-05	3.9645
1427.6	6.715E-03	1.48E-05	3.9653
1433.6	6.645E-03	1.57E-05	3.9659
1440.9	6.375E-03	3.22E-06	3.9686
1443.4	6.240E-03	3.89E-06	3.9700
1444.8	6.149E-03	1.00E-05	3.9709
1460.2	5.976E-03	1.85E-05	3.9726
1465.6	5.894E-03	1.31E-05	3.9734
1470.8	6.003E-03	1.95E-05	3.9723
1473.9	5.992E-03	1.77E-05	3.9724
1476.4	5.959E-03	1.34E-05	3.9728
1451.1	6.069E-03	1.21E-05	3.9717
1444.4	6.143E-03	1.07E-05	3.9709
1437.3	5.797E-03	8.37E-06	3.9744

* Values are given in the chronological order they were measured.

Appendix E: Relative Peak Heights of Current Response

Relative Peak heights of the current response to an Applied Square Wave for the oxide melts

67:33 TiO_2:BaO

T (°C)	Initial Peak	Decay (Field)	Relaxation Peak	Decay (No Field)	Current Offset
1328	1.31	1.05	-0.27	-0.01	-0.05
1355	1.38	1.14	-0.25	0.00	-0.06
1401	1.53	1.28	-0.27	-0.01	-0.06
1417	1.53	1.27	-0.24	0.00	-0.02
1448	1.71	1.45	-0.26	-0.01	-0.07
1487	1.81	1.56	-0.26	-0.01	-0.09

73:27 TiO_2:BaO

T (°C)	Initial Peak	Decay (Field)	Relaxation Peak	Decay (No Field)	Current Offset
Frozen					
1210	1.82	1.81	-0.02	0.01	-0.15
1268	1.90	1.86	-0.05	0.01	-0.13
1323	1.93	1.80	-0.11	0.00	-0.13
1354	1.91	1.67	-0.21	-0.01	-0.12
Transition					
1400(s1)	1.54	1.23	-0.28	0.00	-0.10
1400 (s2)	1.62	1.27	-0.30	-0.02	-0.10
Liquid:					
1402	1.94	1.71	-0.20	-0.02	-0.13
1419	1.73	1.49	-0.24	-0.02	-0.10
1444	1.84	1.63	-0.20	-0.01	-0.12
1477	1.78	1.61	-0.16	0.00	-0.11

Appendix F: Current Response to the Application and Removal of a Square Wave

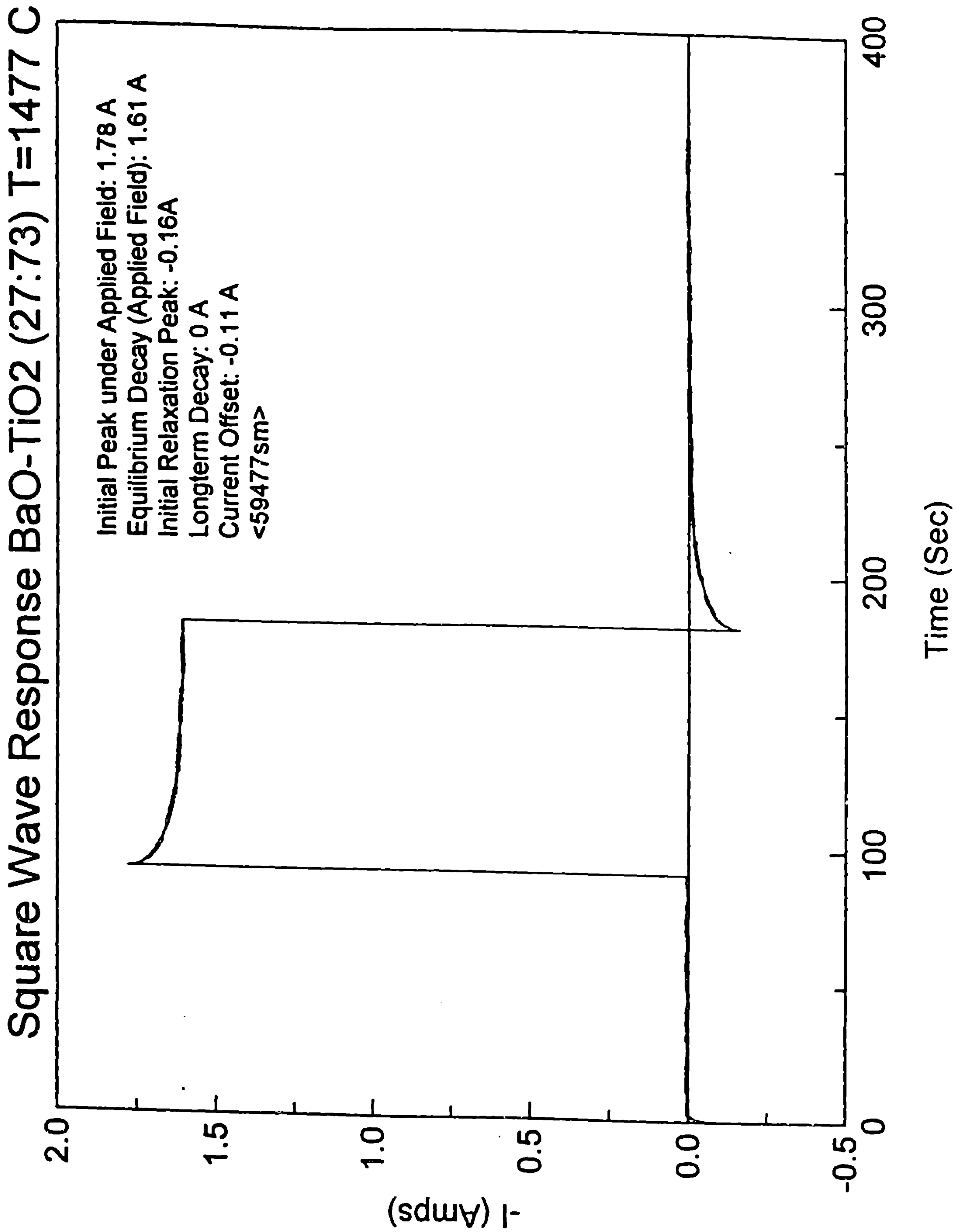

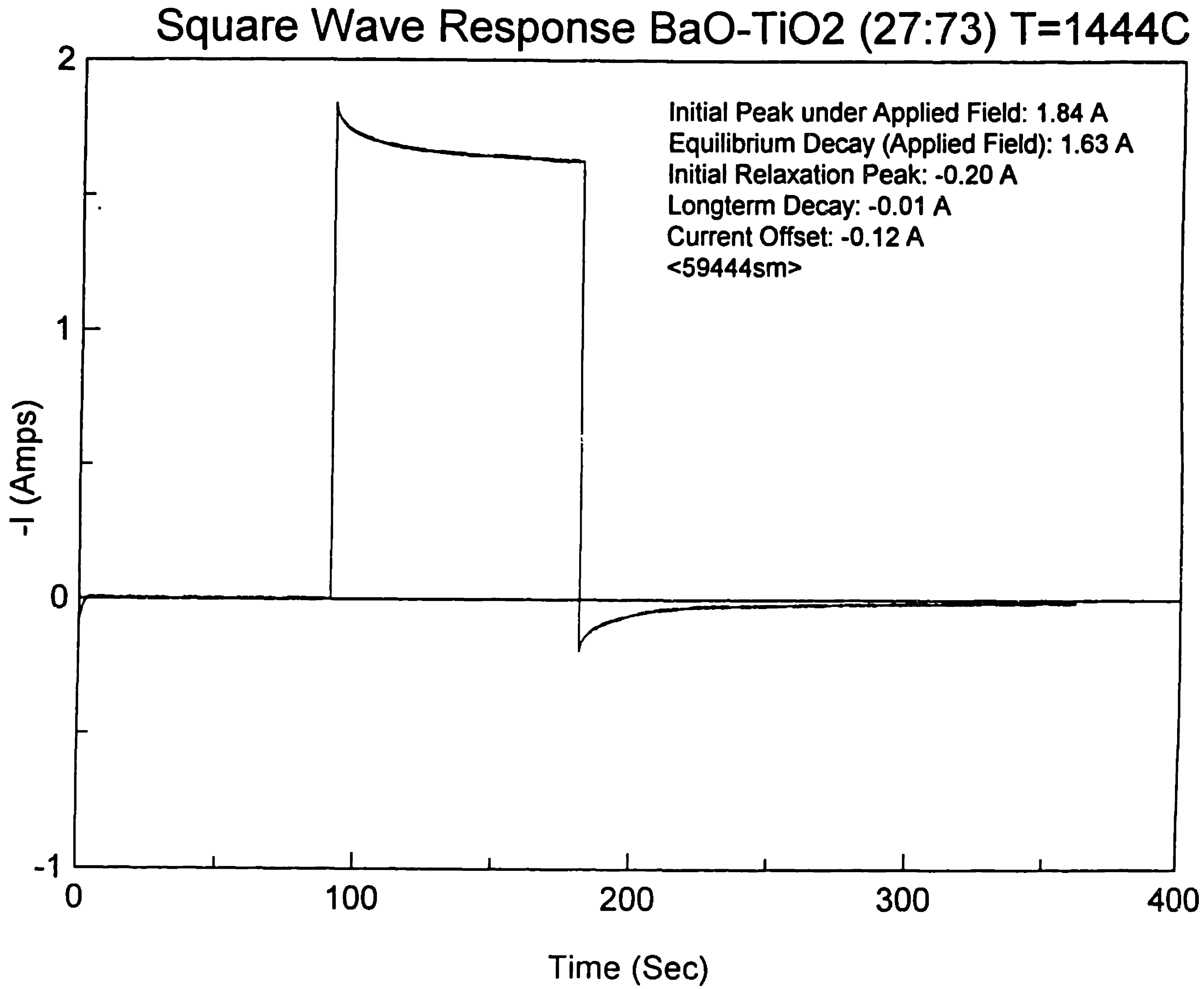
Square Wave Response BaO-TiO2 (27:73) T=1444C
Initial Peak under Applied Field: 1.84 A
Equilibrium Decay (Applied Field): 1.63 A
Initial Relaxation Peak: -0.20 A
Longterm Decay: -0.01 A
Current Offset: -0.12 A
<59444sm>
-I (Amps)
2
1
0
-1
0
100
200
300
400
Time (Sec)

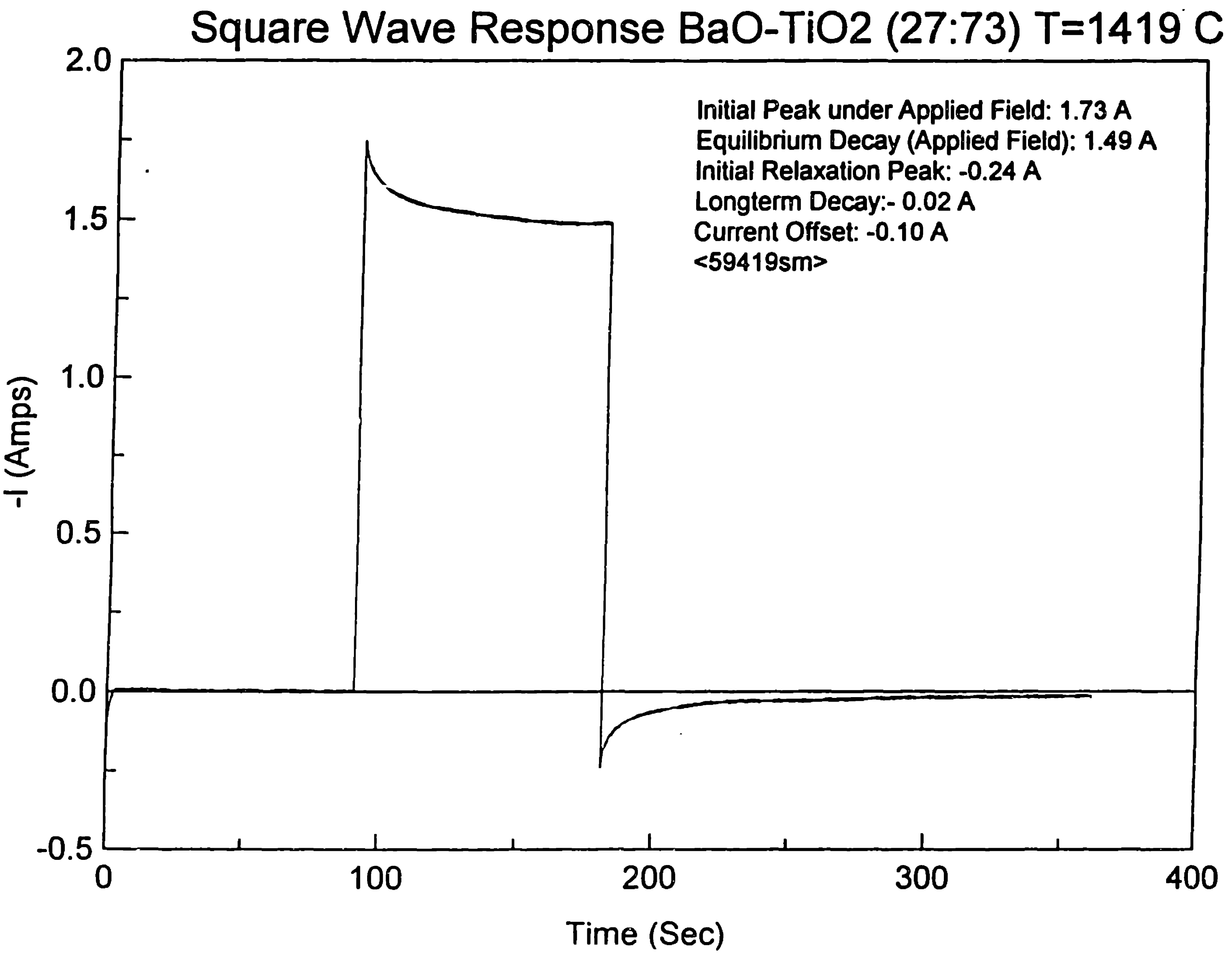
Square Wave Response BaO-TiO2 (27:73) T=1419 C
Initial Peak under Applied Field: 1.73 A
Equilibrium Decay (Applied Field): 1.49 A
Initial Relaxation Peak: -0.24 A
Longterm Decay:- 0.02 A
Current Offset: -0.10 A
<59419sm>
-I (Amps)
2.0
1.5
1.0
0.5
0.0
-0.5
0
100
200
300
400
Time (Sec)

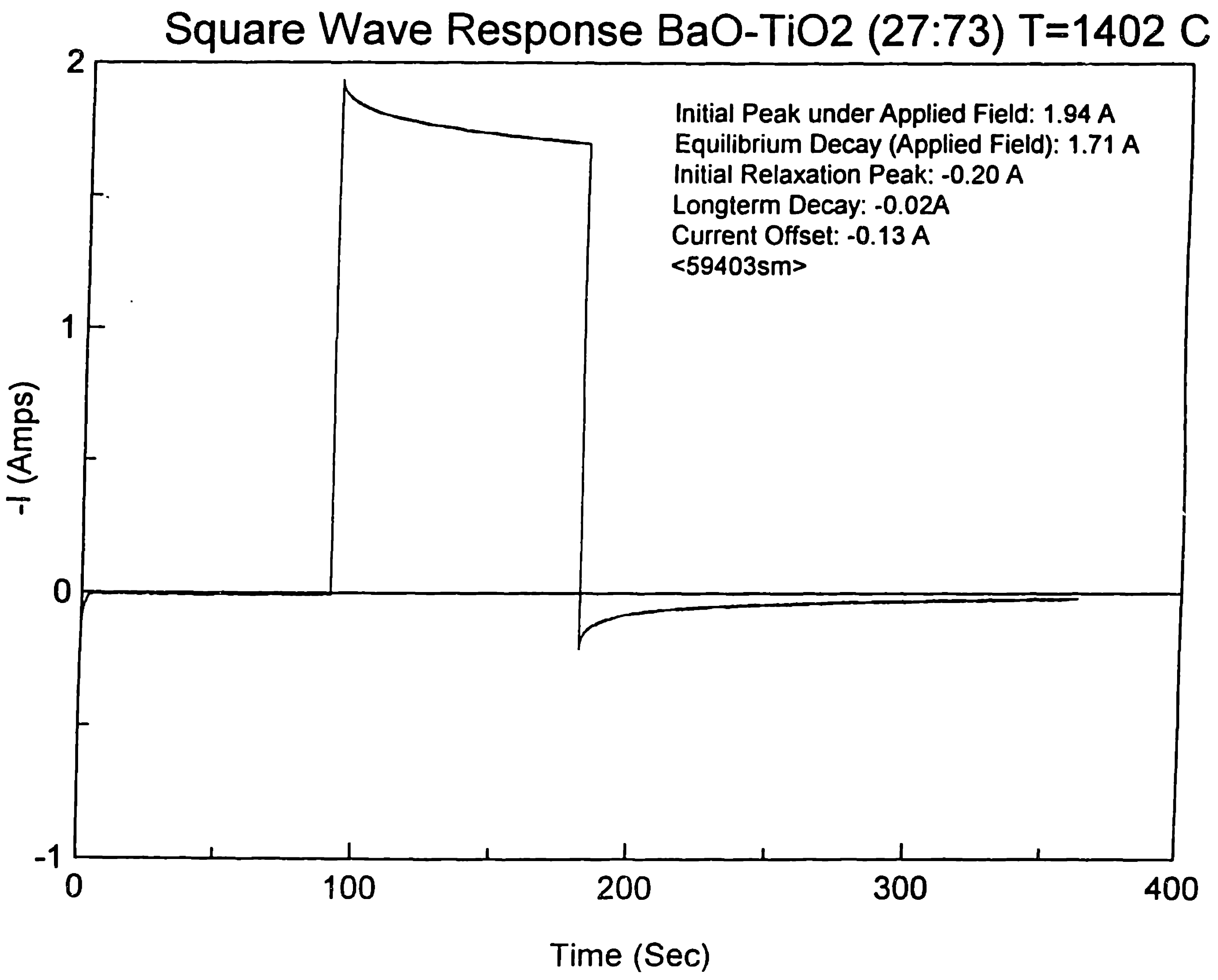
Square Wave Response BaO-TiO2 (27:73) T=1402 C
Initial Peak under Applied Field: 1.94 A
Equilibrium Decay (Applied Field): 1.71 A
Initial Relaxation Peak: -0.20 A
Longterm Decay: -0.02A
Current Offset: -0.13 A
<59403sm>
2
1
0
-1
-I (Amps)
0
100
200
300
400
Time (Sec)

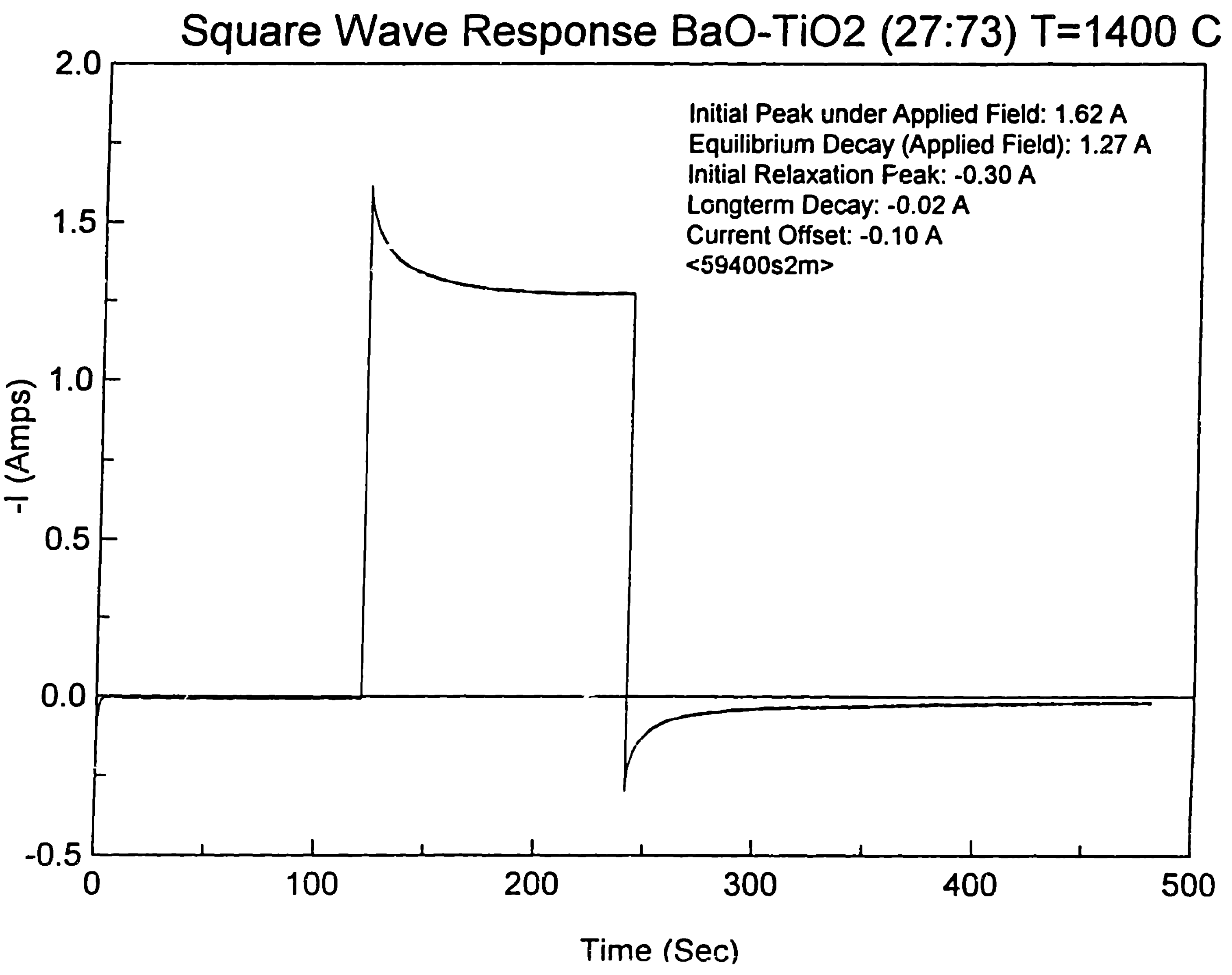
Square Wave Response BaO-TiO2 (27:73) T=1400 C
Initial Peak under Applied Field: 1.62 A
Equilibrium Decay (Applied Field): 1.27 A
Initial Relaxation Peak: -0.30 A
Longterm Decay: -0.02 A
Current Offset: -0.10 A
<59400s2m>
-I (Amps)
2.0
1.5
1.0
0.5
0.0
-0.5
0
100
200
300
400
500
Time (Sec)

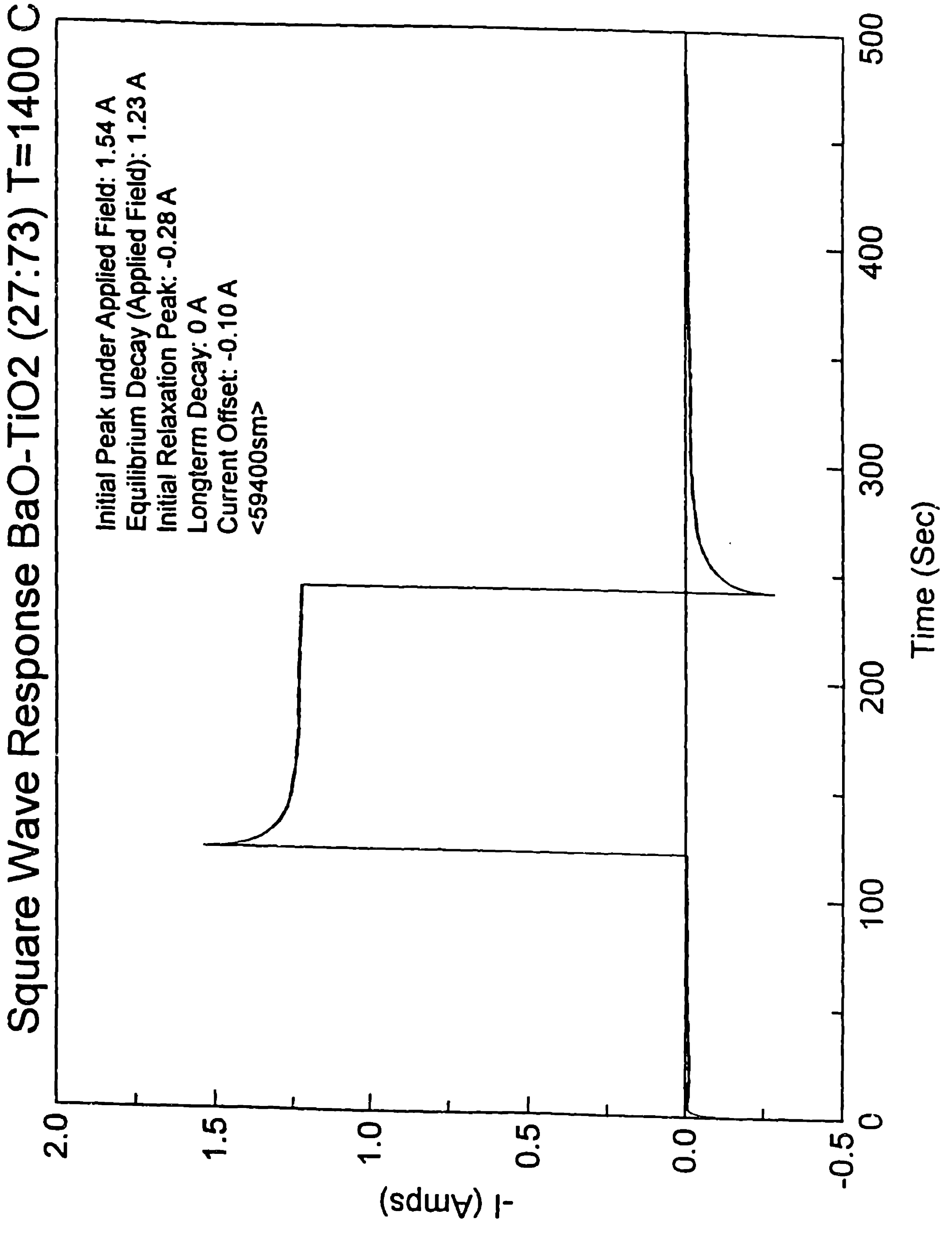
Square Wave Response BaO-TiO2 (27:73) T=1400 C
Initial Peak under Applied Field: 1.54 A
Equilibrium Decay (Applied Field): 1.23 A
Initial Relaxation Peak: -0.28 A
Longterm Decay: 0 A
Current Offset: -0.10 A
<59400sm>
-I (Amps)
2.0
1.5
1.0
0.5
0.0
-0.5
Time (Sec)
0
100
200
300
400
500

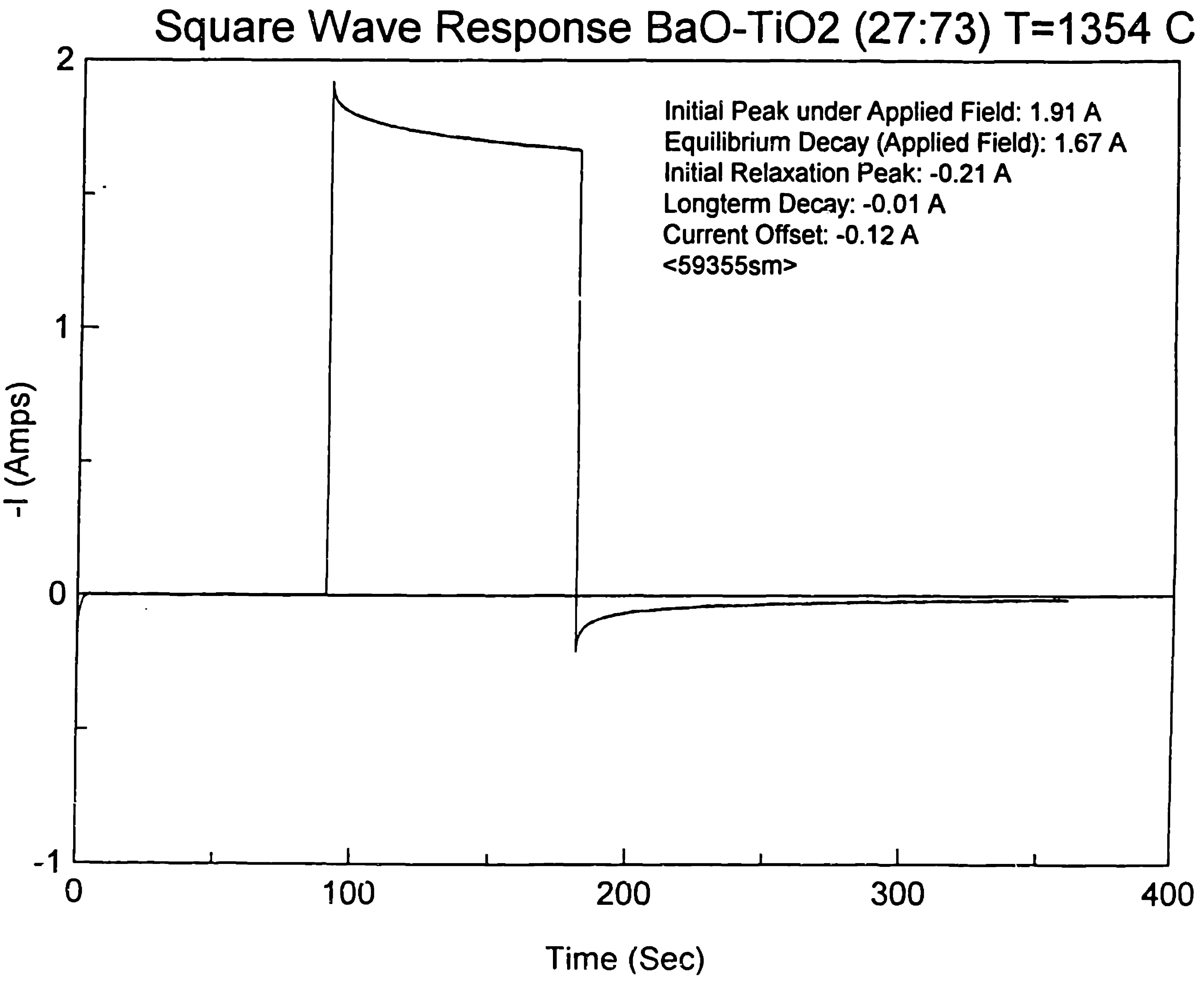
Square Wave Response BaO-TiO2 (27:73) T=1354 C
Initial Peak under Applied Field: 1.91 A
Equilibrium Decay (Applied Field): 1.67 A
Initial Relaxation Peak: -0.21 A
Longterm Decay: -0.01 A
Current Offset: -0.12 A
<59355sm>
-I (Amps)
2
1
0
-1
0
100
200
300
400
Time (Sec)

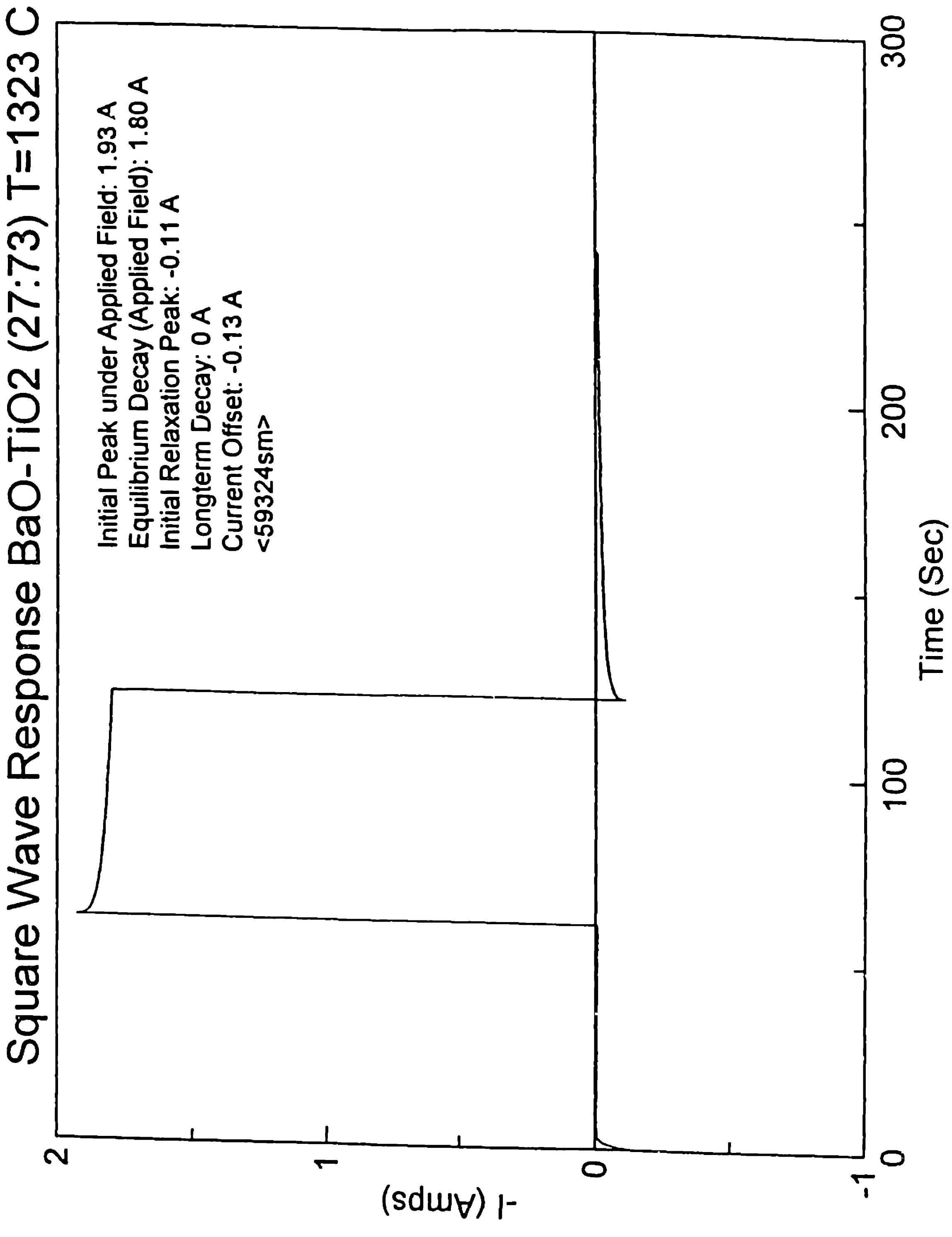
Square Wave Response BaO-TiO2 (27:73) T=1323 C
Initial Peak under Applied Field: 1.93 A
Equilibrium Decay (Applied Field): 1.80 A
Initial Relaxation Peak: -0.11 A
Longterm Decay: 0 A
Current Offset: -0.13 A
<59324sm>
-I (Amps)
2
1
0
-1
Time (Sec)
0
100
200
300

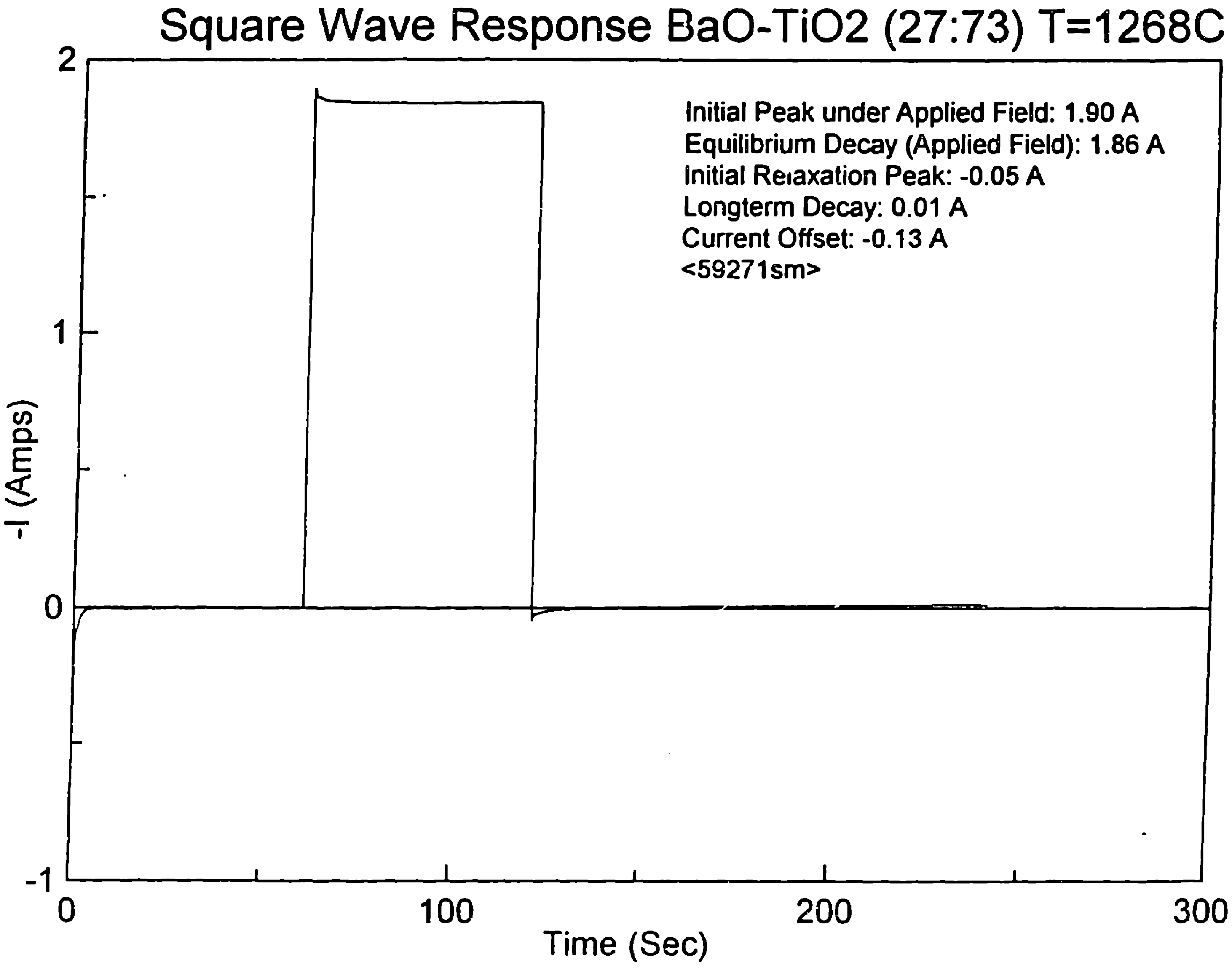
Square Wave Response BaO-TiO2 (27:73) T=1268C
Initial Peak under Applied Field: 1.90 A
Equilibrium Decay (Applied Field): 1.86 A
Initial Relaxation Peak: -0.05 A
Longterm Decay: 0.01 A
Current Offset: -0.13 A
<59271sm>
-I (Amps)
2
1
0
-1
0
100
200
300
Time (Sec)

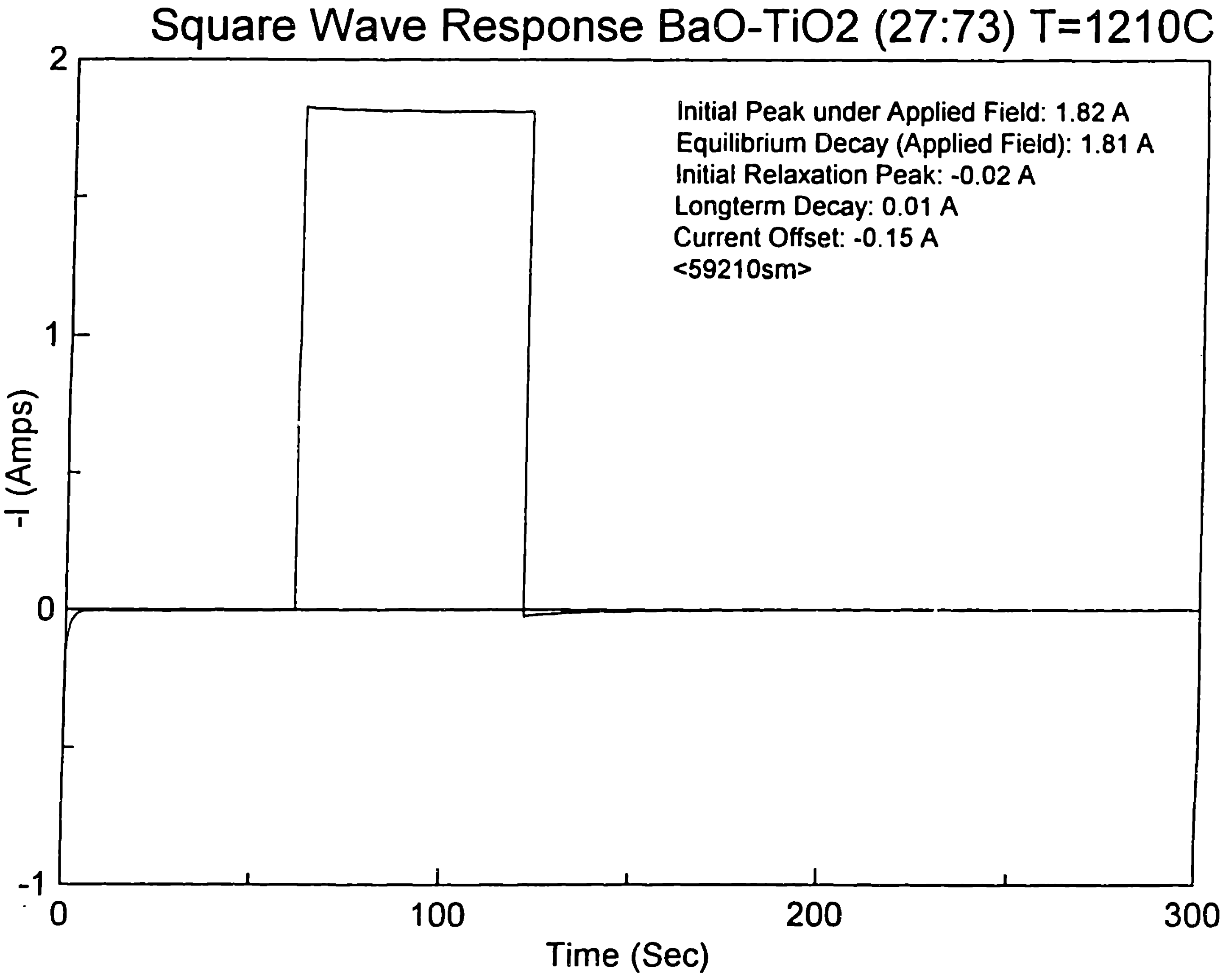
Square Wave Response BaO-TiO2 (27:73) T=1210C
Initial Peak under Applied Field: 1.82 A
Equilibrium Decay (Applied Field): 1.81 A
Initial Relaxation Peak: -0.02 A
Longterm Decay: 0.01 A
Current Offset: -0.15 A
<59210sm>
-I (Amps)
2
1
0
-1
0
100
200
300
Time (Sec)

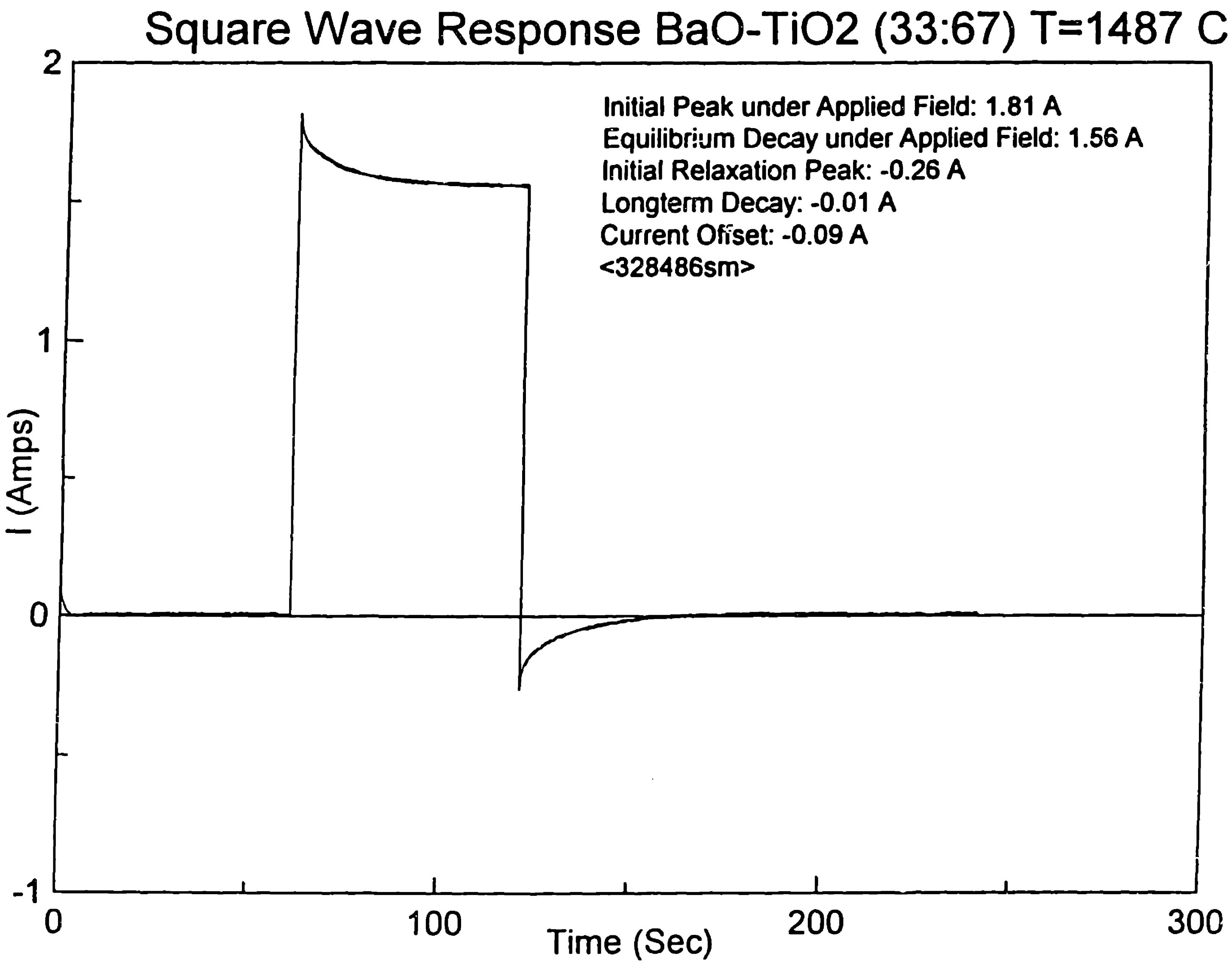
Square Wave Response BaO-TiO2 (33:67) T=1487 C
Initial Peak under Applied Field: 1.81 A
Equilibrium Decay under Applied Field: 1.56 A
Initial Relaxation Peak: -0.26 A
Longterm Decay: -0.01 A
Current Offset: -0.09 A
<328486sm>
I (Amps)
2
1
0
-1
0
100
200
300
Time (Sec)

Square Wave Response BaO-TiO2 (33:67) T=1448 C

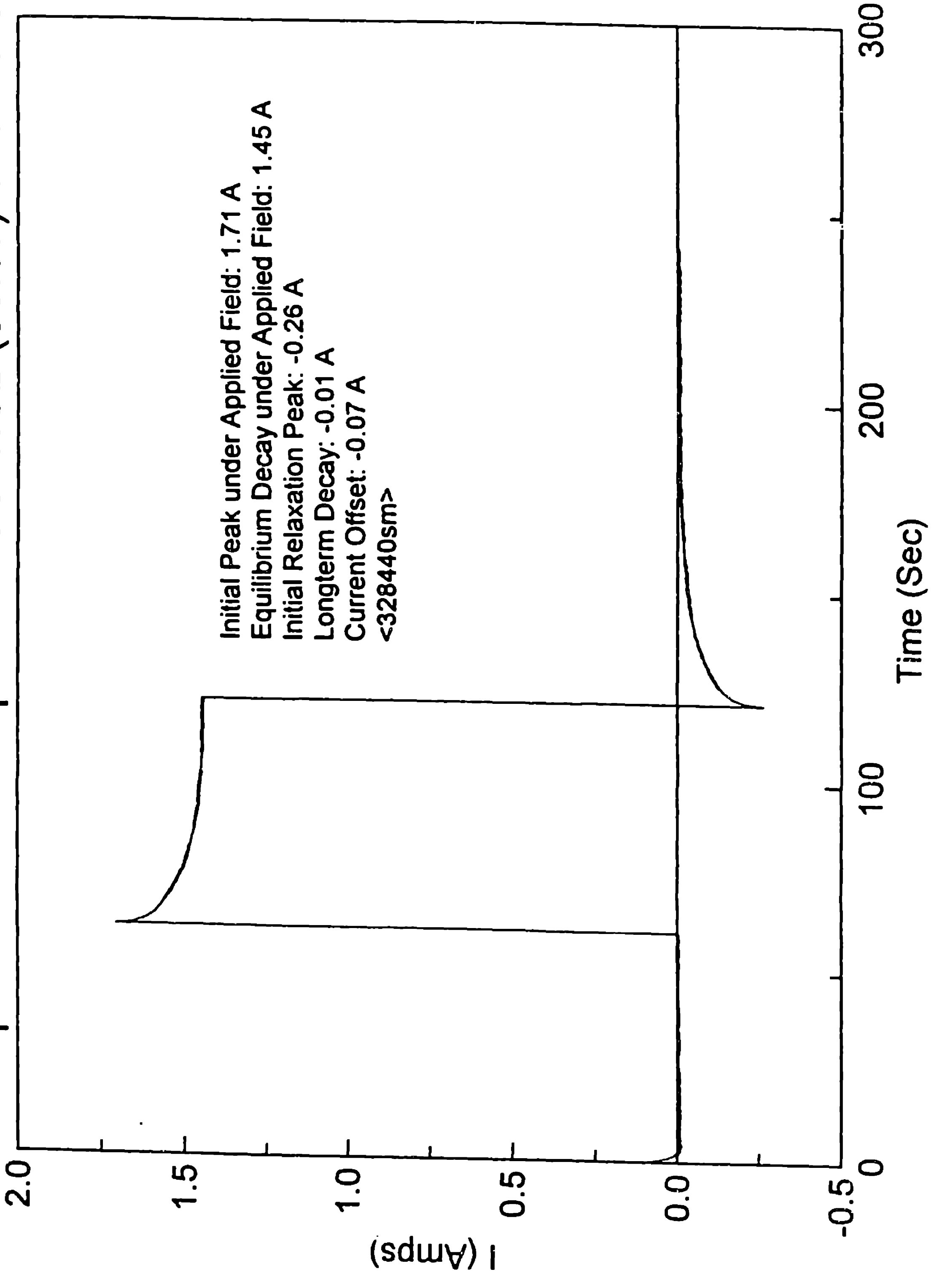

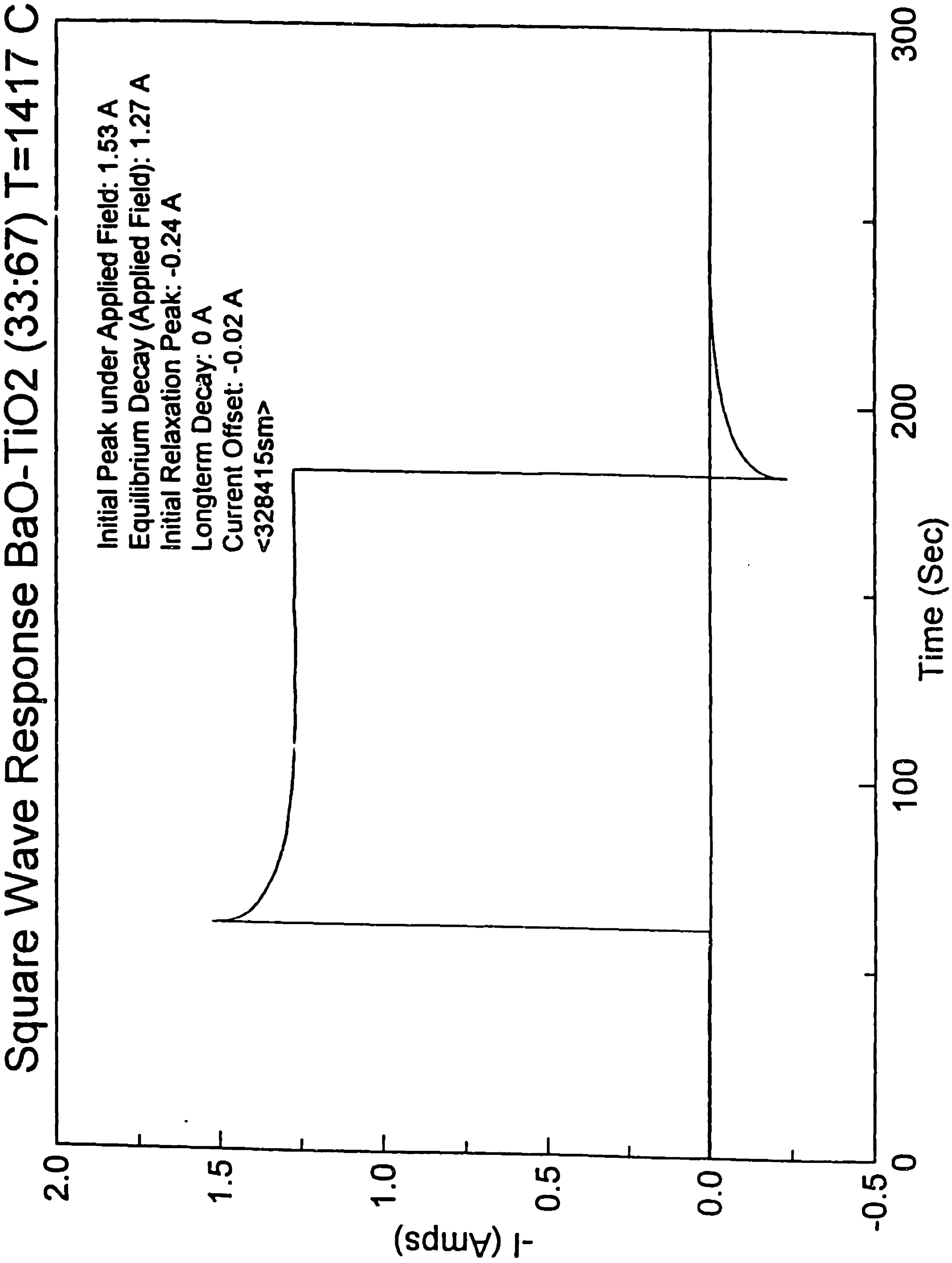
Square Wave Response BaO-TiO2 (33:67) T=1417 C
Initial Peak under Applied Field: 1.53 A
Equilibrium Decay (Applied Field): 1.27 A
Initial Relaxation Peak: -0.24 A
Longterm Decay: 0 A
Current Offset: -0.02 A
<328415sm>
-I (Amps)
2.0
1.5
1.0
0.5
0.0
-0.5
Time (Sec)
0
100
200
300

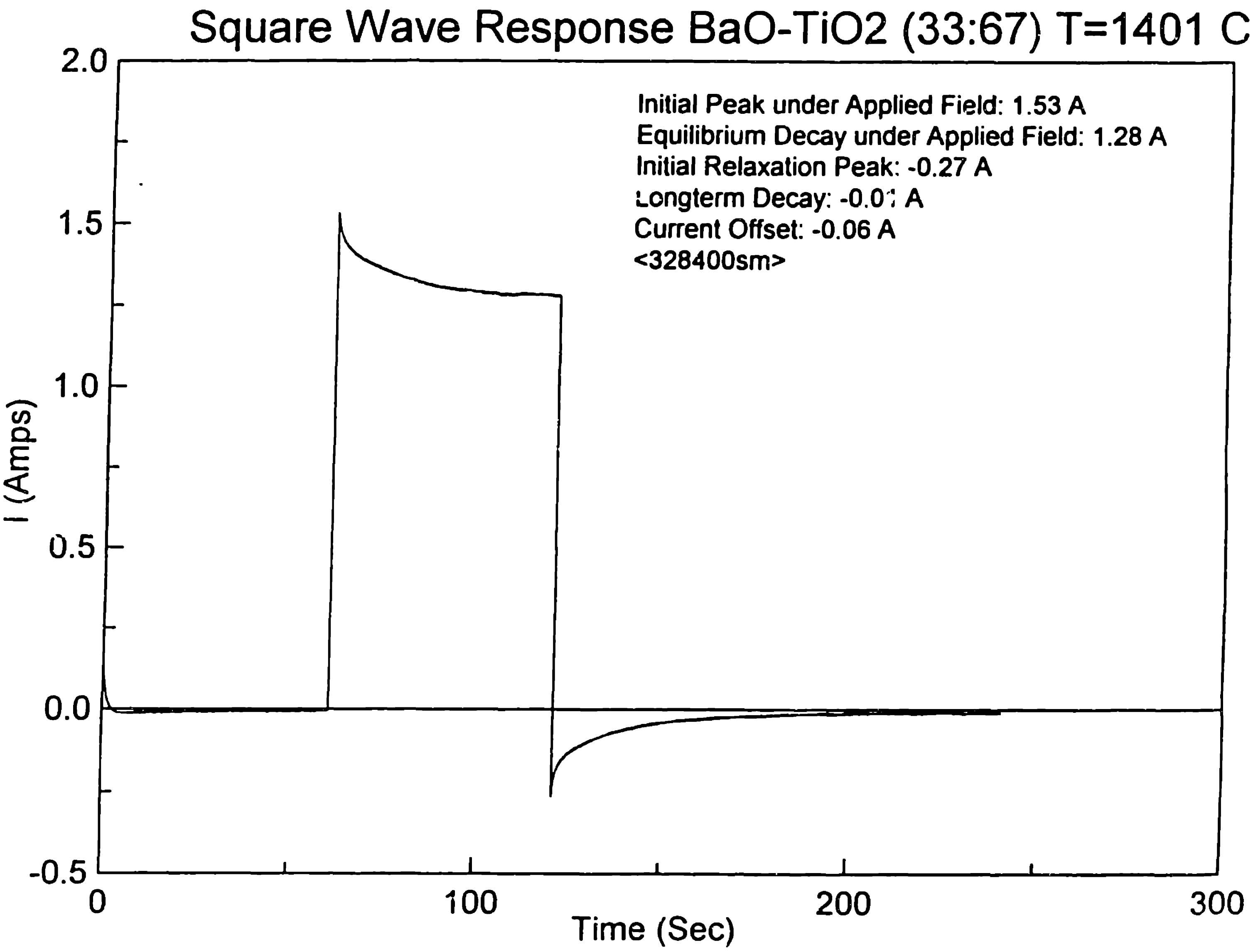
Square Wave Response BaO-TiO2 (33:67) T=1401 C
Initial Peak under Applied Field: 1.53 A
Equilibrium Decay under Applied Field: 1.28 A
Initial Relaxation Peak: -0.27 A
Longterm Decay: -0.01 A
Current Offset: -0.06 A
<328400sm>
I (Amps)
2.0
1.5
1.0
0.5
0.0
-0.5
0
100
200
300
Time (Sec)

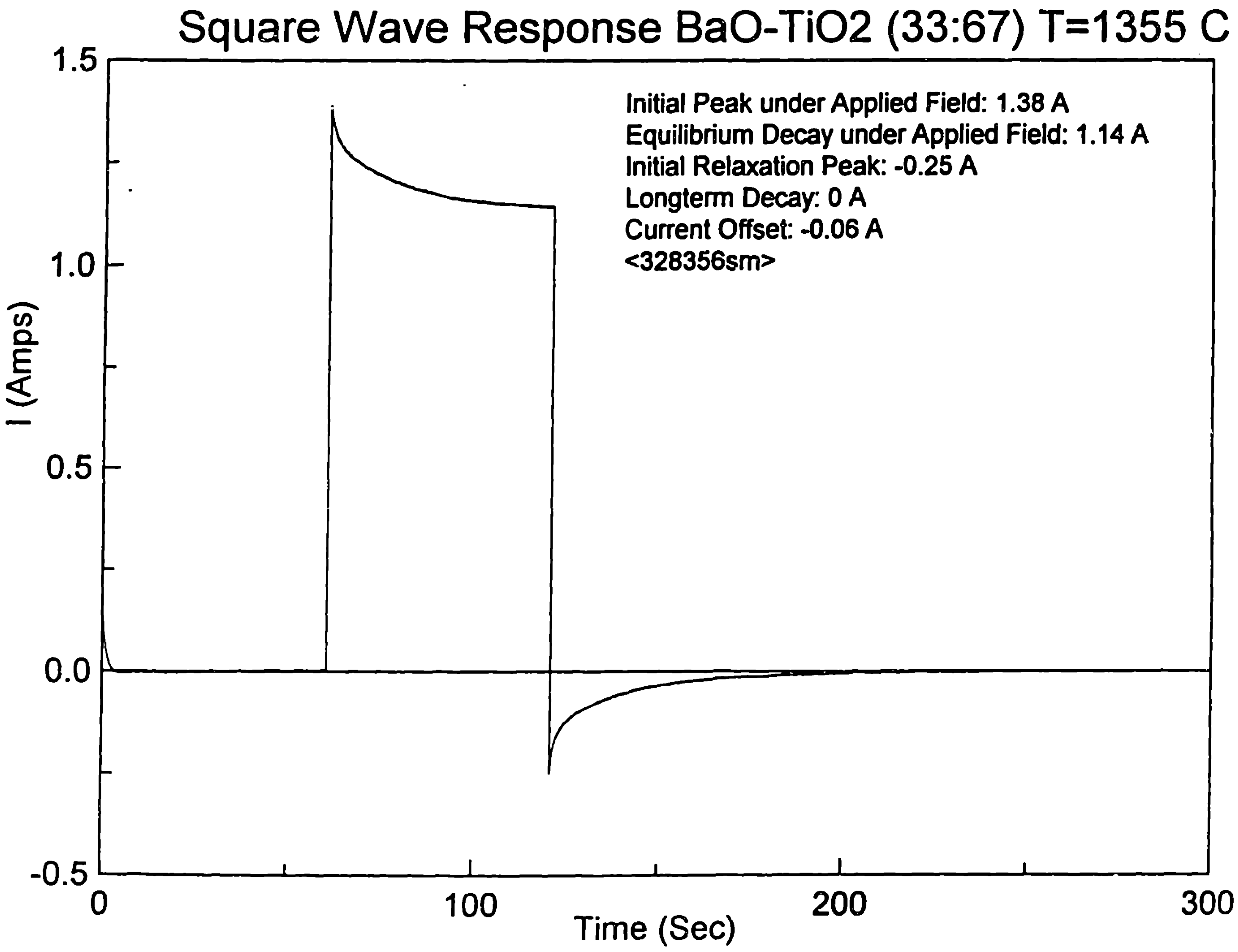
Square Wave Response BaO-TiO2 (33:67) T=1355 C
Initial Peak under Applied Field: 1.38 A
Equilibrium Decay under Applied Field: 1.14 A
Initial Relaxation Peak: -0.25 A
Longterm Decay: 0 A
Current Offset: -0.06 A
<328356sm>
I (Amps)
1.5
1.0
0.5
0.0
-0.5
0
100
200
300
Time (Sec)

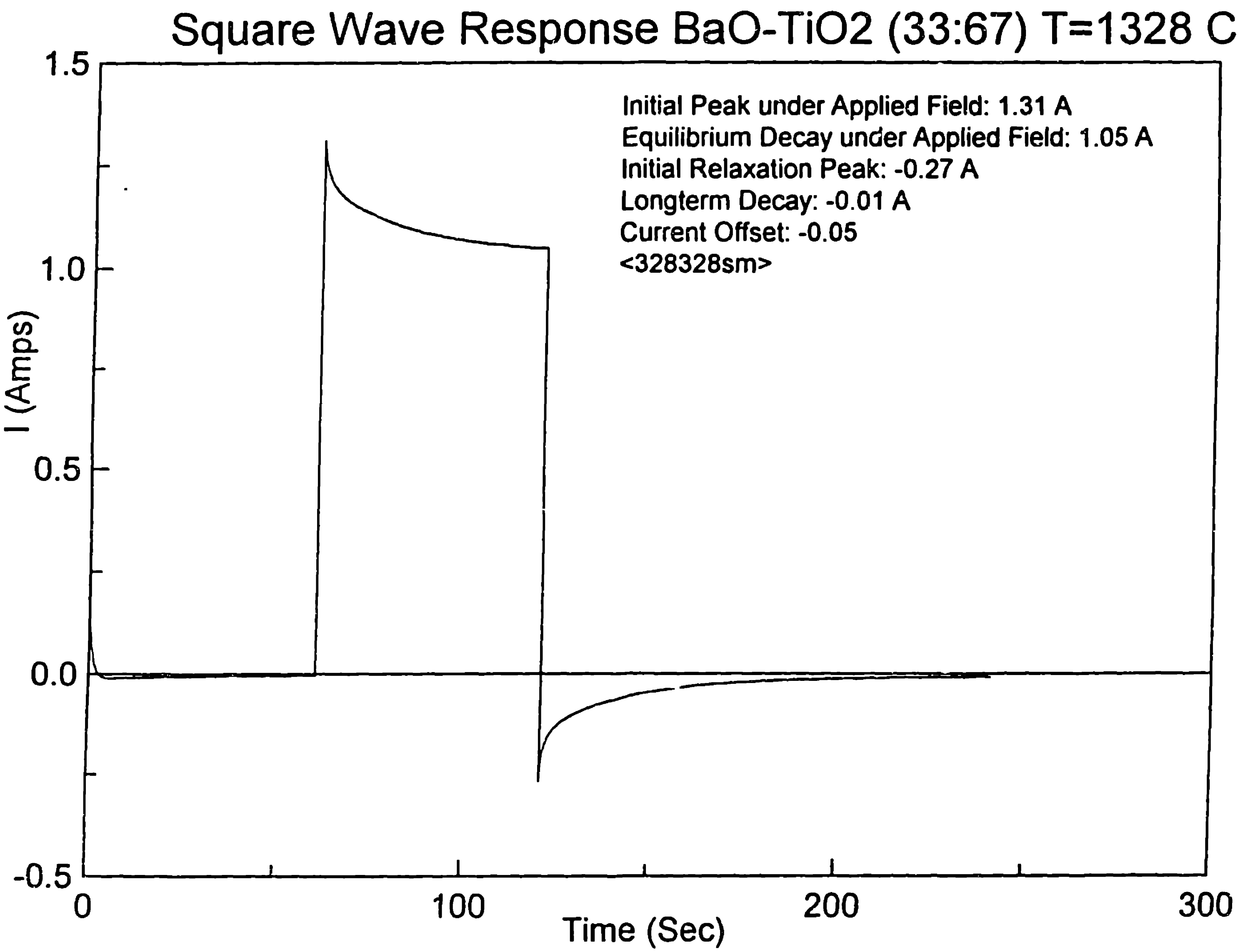
Square Wave Response BaO-TiO2 (33:67) T=1328 C
Initial Peak under Applied Field: 1.31 A
Equilibrium Decay under Applied Field: 1.05 A
Initial Relaxation Peak: -0.27 A
Longterm Decay: -0.01 A
Current Offset: -0.05
<328328sm>
I (Amps)
1.5
1.0
0.5
0.0
-0.5
0
100
200
300
Time (Sec)

Appendix G: Error Analysis

There are various approaches for determining the uncertainty in the measurements presented in this work. This section will estimate the uncertainty in the chloride and oxide measurements using various error analysis techniques.

G.1 Uncertainty in the Chloride Cell Factor-Conductivity Calibration Curve

Uncertainty arises from the physical limitations of the equipment measuring temperature, voltage and current. For the calibration curve, temperature was measured with a type-R thermocouple. The uncertainty in each temperature measurement was on the order of 2° per 800°C (0.25%). The voltage was measured by electrometers with an uncertainty of 0.08% and then recorded by the oscilloscope with an accuracy of 0.4%. Thus the total accuracy of the voltage measurement was 0.4%.[112] The current was measured by the 1286 potentiostat, with an accuracy of 0.3% over this frequency range and then recorded by the oscilloscope with an accuracy of 0.4%. The total current uncertainty was 0.5%. The uncertainty of the calculated raw resistance value (V/I) was 0.6% [67].

G.1.1 Simple Conductivity-Cell Factor Curve Error Analysis

A simple calculation of the uncertainty in the calibration curve is done using equivalent weightings for all the calculated cell factors. All cell factor values are equally weighted. The Fit_find program calculates the uncertainty in the slope and intercept of the conductivity-cell factor curve while performing a least squares regression on the data.

---

[112] To accumulate errors with multiple sources, the squares of the percent error were summed and the square root taken. This operation is also used whenever uncertainties from multiple sources must be multiplied or divided. For addition or subtraction, absolute errors are substituted for the percent error in the above equation.

A Gaussian error distribution is assumed by the least squares fitting routine which assigns some of the uncertainty to the cell factor, which is the dependent variable, and some to the independent variable, the conductivity. The value computed for slope was 0.39215 ± 0.008593 (2.2%) and an intercept of 1.5816 ± 0.02872 (1.8%)

G.1.2 Weighting the Cell Factor

The Fit_find program can perform the same analysis by weighting the cell factor values (the dependent variable) according to the standard deviation of the average resistance values that underlies it. The results based on the weighting of the cell factor in the least squares calculation of the line are reported here for completeness. The values calculated are a slope of 0.3989 ± 0.0693 (17%) and an intercept of 1.61072 ± 0.2311 (14.3%). The magnitude of the slope and intercept calculated with the cell factor weighted according to the standard deviation in resistance differs from the unweighted values by 1.7% for the slope and 1.8% for the intercept.

The increased uncertainty is due in large part to the fact that the number of points contributing to the average resistance was not the same for each temperature. The average resistance was calculated by examining the flat regime in each negative half cycle where the resistance values deviated from each other by less than 2%. The number of points per cycle, and thus per temperature, that contributed to the average resistance values varied from 20-40. A weighting based on the standard deviation of the resistance values is a weighting based on the number of points and not the goodness of the value.

G.2 Uncertainty in Oxide Conductivity

As with the chlorides, the experimentally measured components of the oxide conductivity calculation were voltage, current, and temperature. It is more difficult to make an accurate temperature measurement at 1300-1500°C. While the thermocouple table reliability is the same for a type-R thermocouple for this range and the chloride range (0.25%) [68], the percentage uncertainty of the measurement increases slightly to 4° in 1500 (0.3%).

The voltage is measured directly by the oscilloscope (accuracy of 0.4%). The current is measured by the 1286 potentiostat (accuracy of 0.3%) and then recorded by the oscilloscope (accuracy of 0.4%) for a net voltage uncertainty of 0.5%. Therefore, the uncertainty in each raw resistance measurement was the same as for the chlorides, 0.6%.

An analysis of the uncertainty in the individual conductivity measurements based on both the uncertainty in the cell factor and the standard deviation of the average resistance values is on the order of 3% for both compositions. The following outlines how that value is determined.

For the oxides, conductivity is calculated from equation (6.4):

$$\sigma = a/(R-b) \qquad \text{(G.1)}$$

σ is the conductivity

a is the intercept of the calibration curve

R is the measured melt resistance

b is the slope of the calibration curve

The uncertainty, or error, in σ is calculated by taking the square root of the sum of the percent error in (a) and in (R-b).

$$\%\text{ error in }\sigma=((\%\text{ error in a})^2+(\%\text{ error in (R-b)})^2)^{1/2} \qquad \text{(G.2)}$$

The percent uncertainty in "a" is found from the percent uncertainty reported for the intercept of the calibration curve (standard deviation in "a" divided by the absolute value of "a" times 100), given above in section G.1.1. The uncertainty in (R-b) is calculated using the formula for the uncertainty in sums.

uncertainty in (R-b)=((absolute error in b)^2 +(absolute error in R)^2)$^{1/2}$

The absolute error in "b" is simply the standard deviation in the slope of the calibration curve given above in section G.1.1. The absolute error in R is found from the standard deviation of the average R.

A typical conductivity uncertainty can be calculated by using the standard deviation in "a" of 0.02872 (1.8%), the standard deviation in "b" of 0.008593 (2.2%), and a standard deviation in R (at 1402°C) of 3.1×10^{-6} (0.1%). The resulting uncertainty in the conductivity is 0.1124 (2.8%).

G.2.1 Simple Calculation of Uncertainty in the Conductivity-Temperature Relationship

A simple calculation of the uncertainty in the ln ($\sigma \bullet T$) versus 1/T relationship is performed with each conductivity measurement given equivalent weighting. The uncertainty in the fit is found from the least squares regression of the ln ($\sigma \bullet T$) versus 1/T. This fit gives a slope of 1778 ± 383 (22%) and an intercept of 9.86 ± 0.2288 (2%) for the 67 mol % composition.

G.2.2 Weighted Calculation of Uncertainty in the Conductivity-Temperature Relationship

The standard deviations in the average measured resistance[113] of the oxide melt at each temperature can be used to weight the conductivity points in the conductivity-temperature relationship of the oxides. The slope and intercept are unchanged with the addition of resistance based weighting. However, the uncertainty in the slope decreased to 74 (4%) and the uncertainty in the intercept decreased to 0.0439 (0.4%)

---

[113] The variation in the number of points contributing to each average resistance was far lower than the variation in the number of points for an average chloride resistance measurement. Typically, 800 points were used.

G.2.3 Calculation of the Uncertainty in the Conductivity-Temperature Relationship Accounting for the Uncertainty in the Resistance Value and the Calibration Curve

The uncertainty in the conductivity-temperature relationship can also be measured by taking into account both the uncertainty from the calibration curve (using the simple, unweighted analysis) and the standard deviation of the underlying average resistance values. The uncertainty for each conductivity value, done in the manner outlined in section G.2, is then used as a weight when doing the least squares regression. The value of the slope does not change but the uncertainty calculated by a weighted least squares fit yields rises to 42%. The intercept remains unchanged but the uncertainty from the least square fit is found to be 4.4%.

The results generated by this error analysis technique are open to question. When combining errors from different sources to report the error in an experimental parameter, an assumption is made that the sources of error are not correlated. Clearly this is not the case for calculating the conductivity-temperature relationship for oxides. All points rely on the same cell-factor/conductivity relationship. The uncertainty associated with the cell-factor will be completely correlated among conductivity values and thus its inclusion will result in an overstatement of uncertainty.

G.2.4 Calculation of the Change in Slope from an Analysis of the Endpoints

Another method for examining the effects of uncertainty in the conductivity (based on the uncertainty in the underlying average resistance) on conductivity-temperature relationship is to do an endpoint analysis. The slope and intercept are recalculated in two different ways to yield a maximum and minimum slope.

In the first case, to calculate the steepest slope the percent uncertainty from the average resistance value is used to create an uncertainty in the conductivity. This is then added to the conductivity at the highest temperature (an endpoint of the line) and the appropriate percent is subtracted from the conductivity at the lowest temperature conductivity (the other end member).

The calculation of the minimum slope is done by subtraction of the uncertainty from the high temperature endpoint and the addition of the uncertainty to the low temperature end point. The resulting change in slopes are averaged as are the intercept. Taking the steepest and gentlest slopes for the 67 mol% titanium dioxide relationship, yields an average deviation in the slope of 12.97 (1%) and an average intercept deviation of less than 0.1%.

These analyses were carried out for the 73 mol% TiO_2 composition. All uncertainties were of the same order of magnitude.

G.3 Summary of Magnitude of Errors

In summary, the estimated uncertainty in the calibration curve is on the order of 3%. The estimated uncertainty in the individual oxide conductivity measurements are on the order of 3%. The estimated error in the resulting relationship between $\ln(\sigma \bullet T)$ versus $1/T$ is on the order of 5%.

Bibliography

1. *RWE Australian Business News*, May 11, 1996.

2. D.R. Sadoway, *Electrolytic Production of Metals*, U.S. Patent No. 5,185,068, 1993.

3. G. Heiken, D. Vaniman, B. French, Lunar Sourcebook: A User's Guide to the Moon, Cambridge University Press, New York, 1991 p.137.

4. A.E. Van Arkel, E.A. Flood, N.F.H. Bright, *Can. J. Chem.*, 31, 1953, pp. 1009-1019.

5. W.D. Kingery, H.K. Bowen, D.R. Uhlmann, Introduction to Ceramics, Wiley-Interscience Publications, New York, 1976, Second Edition, p. 868.

6. R. Desrosiers, F. Ajersch, A. Grau, *Nineteenth Annual Conference of Metallurgist, International Symposium on Metallurgical Slags*,Aug. 24-27, 1980. Halifax, Nova Scotia.

7. S.A. Klinchikov, E.F. Kustov, T.K. Maketov, G. Stazko, *Cryst. Res. Technol.*, 16(1) pp. k19-k20.

8. K. Mori, *Tetsu-to-Hagane*, 42(2), 1956, pp. 1024-1029.

9. S.I. Denisov, V.A. Degtyaev, *Izv. Akad. Nauk SSSR Metally*, 1(80), 1970, pp. 48-50.

10. J.O. Bockris, J.A. Kitchner, S. Ignatowicz, J.W. Tomlinson, *Trans. Faraday Soc.*, 48(75), 1952, pp. 75-91.

11. W.J. Zheng, R. Okyama, T. Esaka, H. Iwahara, *Solid State Ionics*, 35 (3-4), 1089, pp. 235-239.

12. V.I. Musithin, V.M. Lepinskikh, Y.A. Fomichev, *Tr. Inst. Met. Sverdlovsk*, 18, 1969, p.293.

13. D.E. Rase and R. Roy, *J. Am. Ceram. Soc.*, 38(3), 1955, p. 111.

14. D.R. Sadoway, K.G. Rhoads, N.A. Fried, S.L. Schiefelbein, *High Accuracy Calibration-Free Electrical Parameter Measurements*, U.S. Patent No. 5,489,849, 1996.

15. N.A. Fried, S.L. Schiefelbein, K.G. Rhoads, D.R. Sadoway, *Proceedings of the International Symposium on Molten Salt Chemistry and Technology*, 93-(9), 1993, pp. 296-305.

16. R.B. Michnick, K.G. Rhoads, D.R. Sadoway, *J. Electrochem. Soc.* (to be submitted 1996).

17. S. Schiefelbein, *Ph.D. Thesis*, Department of Materials Science, MIT, 1996.

18. H. Inouye, J.W. Tomlinson, J. Chipman, *Trans. Faraday Soc.* 49(7), 1953, pp. 796-801.

19. D.G. Lovering, R.J. Gale, Molten Salt Techniques, Vol.1, Plenum Press, New York, 1983, p. 93.

20. R. J. Gale, D.G. Lovering, Molten Salt Techniques, Vol. 2, Plenum Press, New York, 1984, p. 58.

21. J. Hives, J. Thonstad, A. Sterten, P. Fellner, *Electrochim. Acta*, 38 (15), 1993, pp. 2165-2169.

22. G.I. Zhmoidin, *Ind. Lab.*, 35, 1969, pp. 668-672.

23. K. Ogino, H. Hashimoto, S. Hara, *Tetsu-to-Hagane*, 64, 1978, pp. 225-231.

24. K.B. Kim and D.R. Sadoway, *J. Electrochem. Soc.* 139, 1992, pp. 1027-1033.

25. J.R. Melcher, Continuum Electromechanics, MIT Press, Cambridge, MA, 1981, p. 3.3.

26. J.J. O'Dwyer, The Theory of Electrical Conduction and Breakdown in Solid Dielectrics, Clarendon Press, Oxford, 1973, p. 300.

27. H.A. Haus, J.R. Melcher, Electromagnetic Fields and Energy, Prentice-Hall, Englewood Cliffs, New Jersey, 1989, p. 5.2.

28. J.D. Jackson, Classical Electrodynamics, John Wiley and Sons, New York, Second edition, 1975, pp. 42-43.

29. N.N. Lebedev, Special Functions and Their Applications, Dover Publications, New York, 1972, p.146.

30. J.J. Hauser, *Phys. Rev. B*, 31(4), 1985, pp. 2133-2139.

31. C.A. Hogarth, M.H. Islam, A.S.M.S. Rahman, *J. Mat. Sci.*, 28, 1993, pp. 518-528.

32. J.R. MacCallum, C.A. Vincent, eds., Polymer Electrolyte Reviews-1, Elsevier Applied Science, New York, 1987, pp. 237-274.

33. F. Delahaye, *Metrologia*, 29 (2), 1952, pp. 81-93.

34. R.D. Cutkosky, *IEEE Trans. Com. Elec.*, CE-70, 1964, pp. 18-22.

35. P.G. Bruce, J. Evans, C.A. Vincent, *Solid State Ionics*, 28-30, 1988, pp. 918-922.

36. M. Watanabe, M. Togo, K. Sanui, N. Ogata, T. Kobayashi, Z. Ohtaki, *Macromolecules*, 17, 1984, pp. 2908-2912.

37. M.W. Chase, Jr., C.A. Davies, J.R. Downey, Jr., D.J. Frurip, R.A. McDonald, A.N. Syverud, *J. Physical and Chemical Reference Data*, Supplement 14(1), 1985, pp. 753, 773.

38. G.H. Geiger, D.R. Poirier, Transport Phenomena in Metallurgy, Addison-Wesley Publishing, Reading, 1980, p. 451.

39. I.I. Olsen, R. Koksbang, E. Skou, L. Klein, *Electrochim. Acta*, 40 (11), 1995, pp. 1701-1706.

40. J. Evans, C.A. Vincent, P.G. Bruce, *Polymer*, 28, 1987, pp. 2324-2328.

41. P.G. Bruce and C.A. Vincent, *J. Electroanal. Chem.*, 225, 1987, p. 1.

42. P.G. Bruce, J. Evans, C.A. Vincent, *Solid State Ionics*, 28/30, 1988, p. 918.

43. Y.C. Yeh, T.Y. Tseng, D.A. Chang, *J. Am. Ceram. Soc.*, 73(7), 1990, pp. 1992-1998.

44. S. Colson, S.P. Szu, L.C. Klein, J.M. Tarascon, *Solid State Ionics*, 46 (3-4), 1991, pp. 283-289.

45. M. Watanabe, M. Togo, K. Sanui, N. Ogata, T. Kobayshi, Z. Ohtaki, *Macromolecules*, 17, 1984, pp. 2908-2912.

46. F.E. Terman, Radio Engineer's Handbook, McGraw-Hill, New York, 1943, p. 111.

47. P.G. Shewmon, Diffusion in Solids, J. Williams Book Company, Jenks, OK, 1983, p. 2.

48. O.A. Esin, A.I. Sotonikov, Y.P. Nickitin, *Dokl. Akad. Nauk. SSSR*, 158, 1964, p. 1149.

49. G.V. Samsonov, ed., The Oxide Handbook, IFI-Plenum Press, New York, Second Edition, 1982, p. 153.

50. G. Burns, Solid State Physics, Academic Press, New York, 1985, p. 335.

51. E.R. Van Artsdalen, I.S. Yaffe, *J. Phys. Chem.*, 59, 1955, pp. 118-127.

52. M.W. Chase, Jr., C.A. Davies, J.R. Downey, Jr., D.J. Frurip. R.A. McDonald, A.N. Syverud, *J. Physical and Chemical Reference Data*, Supplement 14(1), 1985, p. 905.

53. W.H. Press, B.P. Flannery, S.A, Teukolsky, W.T. Vetterling, Numerical Recipes: the Art of Scientific Computing, Cambridge University Press, Cambridge, 1986. p. 503.

54. G.H. Geiger, D.R. Poirier, Transport Phenomena in Metallurgy, Addison-Wesley Publishing, Reading, 1980, p. 451.

55. G.J. Janz, A.T. Ward, R.D. Reeves, Molten Salt Data: Electrical Conductance, Density, and Viscosity, Technical Bulletin Series, Rensselaer Polytechnic Institute, Troy, NY, 1964.

56. L.L. Hench, J.K. West, Principles of Electronic Ceramics, Wiley and Sons, New York, 1990, p. 139.

57. P.S. Tarsikka, B. Singh, *J. Non-Crystalline Solids*, 124 (1990) p. 224.

58. S. Petrucci, ed. Ionic Interactions From Dilute Solutions to Fused Salts, Academic Press, New York, 1971, p. 283.

59. J.J. Hauser, *Phys. Rev. B.*, 31(4) 1985, pp, 2133-2139.

60. J.W. Mayer, S.S. Lau, Electronic Materials Science: For Integrated Circuits in Si and GaAs, Macillan Press, New York, 1990. p. flyleaf.

61. J.D. Mackenzie, Modern Aspects of the Vitreous State, Butterworth, Washington, 1964, p.134.

62. M. Cutler, Liquid Semiconductors, Academic Press, 1977, p. 131.

63. I.G. Austin, N.F. Mott, *Adv. Physics*, 18, 1969, pp. 41-102.

64. G.N. Greaves, *J. Non-Crystalline Solids*, 11, 1973, pp. 427-446.

65. T. Kudo, H. Obayashi, *J. Electrochem. Soc.*, 123(3), pp. 415-419.

66. G. Handfield, G.G. Charette, *Can. Met. Qua.*, 10(3), 1971, pp. 235-243.

67. D.C. Harris, Quantitative Analysis, W. H. Freeman and Company, New York, 1982, pp. 32-38.

68. R.L. Powell, W.J.Hall, C.H. Hyink, J.L. Sparks, G.W. Burns, M.C. Scroger, H.H. Plumb Thermocouple Reference Table Based on IPTs-68, U.S. Dept. of Commerce, National Bureau of Standards, 1974, p. 31.